Pluripotent stem-cell-based screening uncovers sildenafil as a mitochondrial disease therapy

Annika Zink, Dao-Fu Dai, Annika Wittich, Marie-Thérèse Henke, Giulia Pedrotti, Sonja Heiduschka, Guillem Santamaria, Tancredi Massimo Pentimalli, Christian Brueser, Sofia Notopoulou, Abdul Rahim Umar, Aleksandra Zhaivoron, Laura Petersilie, Caleb Jerred, Jesper Bergmans, Louis Anton Neu, Fabian Schumacher, Jan Keller-Findeisen, Agnieszka Rybak-Wolf, Daniel Stach, Jeanette Reinshagen, Undine Haferkamp, Kim Krieg, Andrea Zaliani, Liliya Euro, Alessia Di Donfrancesco, Chiara Santanatoglia, Enrica Cappellozza, Marta Suarez Cubero, Mario Pavez-Giani, Oleh Bakumenko, David Meierhofer,

Article - Version of Record

Suggested Citation:
Zink, A., Dai, D.-F., Wittich, A., Henke, M.-T., Pedrotti, G., Heiduschka, S.,Santamaria, G., Pentimalli, T. M., Brueser, C., Notopoulou, S., Umar, A. R.,Zhaivoron, A., Petersilie, L., Jerred, C., Bergmans, J., Neu, L. A., Schumacher,F., Keller-Findeisen, J., Rybak-Wolf, A., … Prigione, A. (2026). Pluripotentstem-cell-based screening uncovers sildenafil as a mitochondrial diseasetherapy. Cell, 189(6), 1656-1679.e42. https://doi.org/10.1016/j.cell.2026.02.008[https://doi.org/10.1016/j.cell.2026.02.008]

Cell

Article

Pluripotent stem-cell-based screening uncovers sildenafil as a mitochondrial disease therapy

Graphical abstract

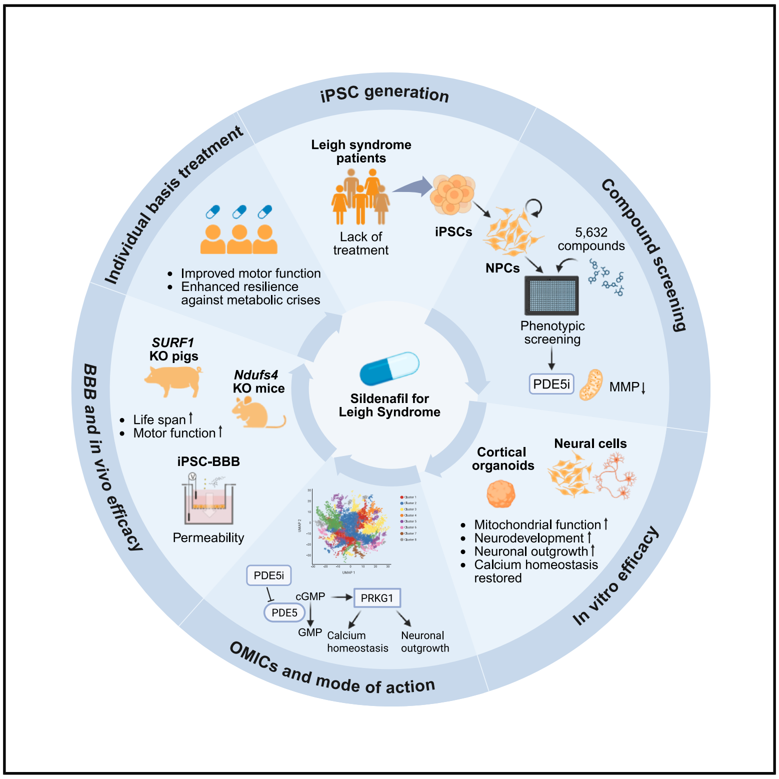

Highlights

- Repurposable drug screen in Leigh syndrome neural cells identifies PDE5 inhibitors
- PDE5 inhibitor sildenafil rescues the neurodevelopmental disease signature *in vitro*
- PDE5 inhibitor sildenafil extends the lifespan of Leigh syndrome animal models *in vivo*
- Sildenafil treatment on an individual basis clinically improves symptoms in six LS patients

Authors

Annika Zink, Dao-Fu Dai,
Annika Wittich, ..., Ole Pless,
Markus Schuelke, Alessandro Prigione

Correspondence

ddai4@jh.edu (D.-F.D.),
dario.brunetti@unimi.it (D.B.),
antonio.delsol@uni.lu (A.d.S.),
emanuela.bottani@univr.it (E.B.),
ole.pless@itmp.fraunhofer.de (O.P.),
markus.schuelke@charite.de (M.S.),
alessandro.prigione@hhu.de (A.P.)

In brief

Leigh syndrome is a severe and untreatable mitochondrial disease. Using patient-derived models in 2D and 3D, Zink and colleagues identify the PDE5 inhibitor sildenafil as a repurposable drug candidate, leading to lifespan extension in mammalian models and clinical improvement in six individuals with Leigh syndrome.

Zink et al., 2026, Cell *189*, 1656–1679

https://doi.org/10.1016/j.cell.2026.02.008

CellPress

CellPress
OPEN ACCESS

Cell

Article

Pluripotent stem-cell-based screening uncovers sildenafil as a mitochondrial disease therapy

Annika Zink,[1,51] Dao-Fu Dai,[2,51,52,*] Annika Wittich,[3,51] Marie-Thérèse Henke,[4,5,51] Giulia Pedrotti,[6,51] Sonja Heiduschka,[1,7,51] Guillem Santamaria,[8] Tancredi Massimo Pentimalli,[9,10] Christian Brueser,[11] Sofia Notopoulou,[12] Abdul Rahim Umar,[13] Aleksandra Zhaivoron,[14] Laura Petersilie,[15] Caleb Jerred,[1,7] Jesper Bergmans,[16,17] Louis Anton Neu,[15] Fabian Schumacher,[18] Jan Keller-Findeisen,[11] Agnieszka Rybak-Wolf,[9] Daniel Stach,[3] Jeanette Reinshagen,[3] Undine Haferkamp,[3] Kim Krieg,[3] Andrea Zaliani,[3] Liliya Euro,[14] Alessia Di Donfrancesco,[19] Chiara Santanatoglia,[6] Enrica Cappellozza,[6] Marta Suarez Cubero,[20] Mario Pavez-Giani,[21,22] Oleh Bakumenko,[11] David Meierhofer,[23]

(Author list continued on next page)

[1]Department of General Pediatrics, Neonatology and Pediatric Cardiology, Medical Faculty, University Hospital Düsseldorf, Heinrich-Heine-Düsseldorf, 40225 Düsseldorf, Germany
[2]Department of Pathology, Johns Hopkins University School of Medicine, Baltimore, MD 21218, USA
[3]Fraunhofer Institute for Translational Medicine and Pharmacology ITMP, Discovery Research ScreeningPort, 22525 Hamburg, Germany
[4]Charité - Universitätsmedizin Berlin, corporate member of Freie Universität Berlin and Humboldt-Universität zu Berlin, Department of Neuropediatrics, 10117 Berlin, Germany
[5]Charité - Universitätsmedizin Berlin, corporate member of Freie Universität Berlin and Humboldt-Universität zu Berlin, NeuroCure Clinical Research Center, 10117 Berlin, Germany
[6]Department of Diagnostics and Public Health, University of Verona, 37134 Verona, Italy
[7]Faculty of Mathematics and Natural Sciences, Heinrich Heine University, 40225 Düsseldorf, Germany
[8]Computational Biology Group, Luxembourg Centre for Systems Biomedicine, University of Luxembourg, 4366 Esch-sur-Alzette, Luxembourg
[9]Berlin Institute for Medical Systems Biology (BIMSB), Max Delbrück Center for Molecular Medicine in the Helmholtz Association (MDC), 10115 Berlin, Germany
[10]Charité – Universitätsmedizin Berlin, 10117 Berlin, Germany
[11]Fraunhofer Institute for Translational Medicine and Pharmacology ITMP, Translational Neuroinflammation and Automated Microscopy, 37037 Göttingen, Germany
[12]Institute of Applied Biosciences (INAB), Centre For Research and Technology Hellas (CERTH), 57001 Thessaloniki, Greece
[13]Department of Physics, University of South Florida, Tampa, FL 33620, USA
[14]Stem Cells and Metabolism Program, Faculty of Medicine, University of Helsinki, 00014 Helsinki, Finland
[15]Institute of Neurobiology, Heinrich Heine University, 40225 Düsseldorf, Germany
[16]Radboud Center for Mitochondrial Medicine, Radboud University Medical Center, 6500 HB Nijmegen, the Netherlands

(Affiliations continued on next page)

SUMMARY

Mitochondrial disease encompasses inherited disorders affecting mitochondrial function. A severe and untreatable form of mitochondrial disease is Leigh syndrome (LS), causing psychomotor regression and metabolic crises. To accelerate drug discovery for LS, we screen a library of 5,632 repurposable compounds in neural cells from LS-patient-derived induced pluripotent stem cells (iPSCs). We identify phosphodiesterase type 5 (PDE5) inhibitors as leads and prioritize sildenafil for its clinical safety. Sildenafil corrects mitochondrial membrane potential defects, restores neurodevelopmental pathways, and normalizes calcium responses in LS brain organoids. In small and large mammalian models of LS, sildenafil extends lifespan and ameliorates disease phenotypes. Off-label treatment on an individual basis with sildenafil in six LS patients improves their motor function and resistance to metabolic crises. Collectively, the findings highlight the potential of iPSC-driven drug discovery and position sildenafil as a promising drug candidate for mitochondrial disease.

INTRODUCTION

Mitochondrial disease encompasses rare genetic conditions caused by dysfunction in the cell's energy-producing organelles.[1] A severe form of mitochondrial disease is Leigh syndrome (LS, OMIM #256000), which is characterized by neurodevelopmental regression and muscle weakness, with early death following metabolic crises.[2,3] LS can result from pathogenic variants in more than 100 genes in nuclear DNA or mitochondrial DNA (mtDNA) involved in oxidative phosphorylation (OXPHOS),[4]

Alan Foley,[8] Susanne Morales-Gonzalez,[4] Isabella Tolle,[1] Diran Herebian,[1] Daniele Bonesso,[24] Giulia Cecchetto,[1] Sakurako Nagumo Wong,[9] Monica Moresco,[25] Alessandra Maresca,[25] Ilaria Decimo,[6] Francesco De Sanctis,[26] Annalisa Adamo,[26] Merel J.W. Adjobo-Hermans,[16,27] Roberto Duchi,[28] Maria Barandalla,[28] Marco Scaglia,[28] Andrea Perota,[28] Cesare Galli,[28] Burkhard Kleuser,[18] Lukas Cyganek,[11,21,37] Chris Mühlhausen,[29] Lars Schlotawa,[11,29,30] Valeria Tiranti,[19] Ertan Mayatepek,[1] Ildiko Szabo,[24] Chiara La Morgia,[25,31] Thomas Klopstock,[32,33,34] Valerio Carelli,[25,31] Felix Distelmaier,[1] Andrea Rossi,[35] Nikolaus Rajewsky,[9,36,37,38,39] Ghanim Ullah,[13] Stefan Jakobs,[11,30,40,41] Christine R. Rose,[15] Spyros Petrakis,[12] Frank Edenhofer,[20] Werner J.H. Koopman,[16,17,42] Pawel Lisowski,[9,43,44] Anu Suomalainen,[14,45,46] Dario Brunetti,[19,47,52,*] Antonio del Sol,[8,48,49,52,*] Emanuela Bottani,[6,52,*] Ole Pless,[3,52,*] Markus Schuelke,[4,5,50,52,*] and Alessandro Prigione[1,52,53,*]

[17] Department of Pediatrics, Amalia Children's Hospital, Radboud University Medical Center, 6525 GA Nijmegen, the Netherlands
[18] Institute of Pharmacy, Freie Universität Berlin, 14195 Berlin, Germany
[19] Fondazione IRCCS Istituto Neurologico Carlo Besta, 20126 Milan, Italy
[20] Department of Molecular Biology & CMBI, Genomics, Stem Cell & Regenerative Medicine Group, University of Innsbruck, 6020 Innsbruck, Austria
[21] Stem Cell Unit, Clinic for Cardiology and Pneumology, University Medical Center Göttingen, 37075 Göttingen, Germany
[22] Experimental Cardiology Institute, Medical Clinic I/Cardiology and Angiology, Justus Liebig University of Giessen, 35392 Giessen, Germany
[23] Max Planck Institute for Molecular Genetics, 14195 Berlin, Germany
[24] Department of Biology, University of Padova, 35121 Padova, Italy
[25] IRCCS Istituto delle Scienze Neurologiche di Bologna, Programma di Neurogenetica, 40139 Bologna, Italy
[26] Department of Medicine, Section of Immunology, University of Verona Hospital Trust, 37134 Verona, Italy
[27] Department of Medical BioSciences, Radboud Center for Mitochondrial Medicine, Radboud University Medical Center, 6525 GA Nijmegen, the Netherlands
[28] Avantea, 26100 Cremona, Italy
[29] Department of Pediatrics and Adolescent Medicine, University Medical Center, Georg-August-University, 37075 Göttingen, Germany
[30] German Center for Child and Adolescent Health (DZKJ), Section CNS Development and Neurological Disease, partner site Göttingen, Robert-Koch-Str. 40, 37075 Göttingen, Germany
[31] Department of Biomedical and Neuromotor Sciences (DIBINEM), University of Bologna, 40127 Bologna, Italy
[32] Friedrich-Baur-Institute, Department of Neurology, LMU University Hospital, Ludwig-Maximilians-Universität München, 80336 Munich, Germany
[33] Munich Cluster for Systems Neurology (SyNergy), 81377 Munich, Germany
[34] German Center for Neurodegenerative Diseases (DZNE), 81377 Munich, Germany
[35] Genome Engineering and Model Development lab (GEMD), IUF-Leibniz Research Institute for Environmental Medicine, 40223 Düsseldorf, Germany
[36] NeuroCure Cluster of Excellence, 10117 Berlin, Germany
[37] German Center for Cardiovascular Research (DZHK), partner site Lower Saxony and Berlin, 10785 Berlin, Germany
[38] National Center for Tumor Diseases (NCT), German Cancer Consortium (DKTK), 13125 Berlin, Germany
[39] German Center for Neurodegenerative Diseases (DZNE), 10117 Berlin, Germany
[40] Department of NanoBiophotonics, Max Planck Institute for Multidisciplinary Sciences, 37077 Göttingen, Germany
[41] Department of Neurology, University Medical Center Göttingen, 37075 Göttingen, Germany
[42] Human and Animal Physiology, Wageningen University, 6708 WD Wageningen, the Netherlands
[43] Neuropsychiatry and Laboratory of Molecular Psychiatry, Department of Psychiatry and Neurosciences, Charité - Universitätsmedizin Berlin, 10117 Berlin, Germany
[44] Department of Molecular Biology, Institute of Genetics and Animal Biotechnology, Polish Academy of Sciences, 05-552 Jastrzebiec n/Warsaw, Poland
[45] HiLife, University of Helsinki, 0004 Helsinki, Finland
[46] HUS Diagnostics, Helsinki University Hospital, 00290 Helsinki, Finland
[47] Department of Clinical Sciences and Community Health, Dipartimento di Eccellenza 2023-2027, University of Milan, 20122 Milan, Italy
[48] IKERBASQUE, Basque Foundation for Science, 48009 Bilbao, Spain
[49] CIC bioGUNE-BRTA (Basque Research and Technology Alliance), Bizkaia Technology Park, 48160 Derio, Spain
[50] German Center for Child and Adolescent Health (DZKJ), Section CNS Development and Neurological Disease, partner site Berlin, 13353 Berlin, Germany
[51] These authors contributed equally
[52] Senior author
[53] Lead contact
*Correspondence: ddai4@jh.edu (D.-F.D.), dario.brunetti@unimi.it (D.B.), antonio.delsol@uni.lu (A.d.S.), emanuela.bottani@univr.it (E.B.), ole.pless@itmp.fraunhofer.de (O.P.), markus.schuelke@charite.de (M.S.), alessandro.prigione@hhu.de (A.P.)

https://doi.org/10.1016/j.cell.2026.02.008

including complex V (CV) gene *MT-ATP6* (mitochondrially encoded ATP synthase subunit 6),[5] complex IV (CIV) assembly factor gene *SURF1* (SURFEIT1),[6] and complex I gene *NDUFS4* (nicotinamide adenine dinucleotide [NAD] + hydrogen [NADH] dehydrogenase [ubiquinone] iron-sulfur protein 4).[7]

Currently, there are no treatments for LS.[8] One obstacle to therapy discovery is the paucity of model systems.[9] The difficulties in mtDNA editing have hindered the establishment of models for mtDNA defects.[10] A pig model of LS due to *SURF1* knockout (KO) showed neurodevelopmental defects

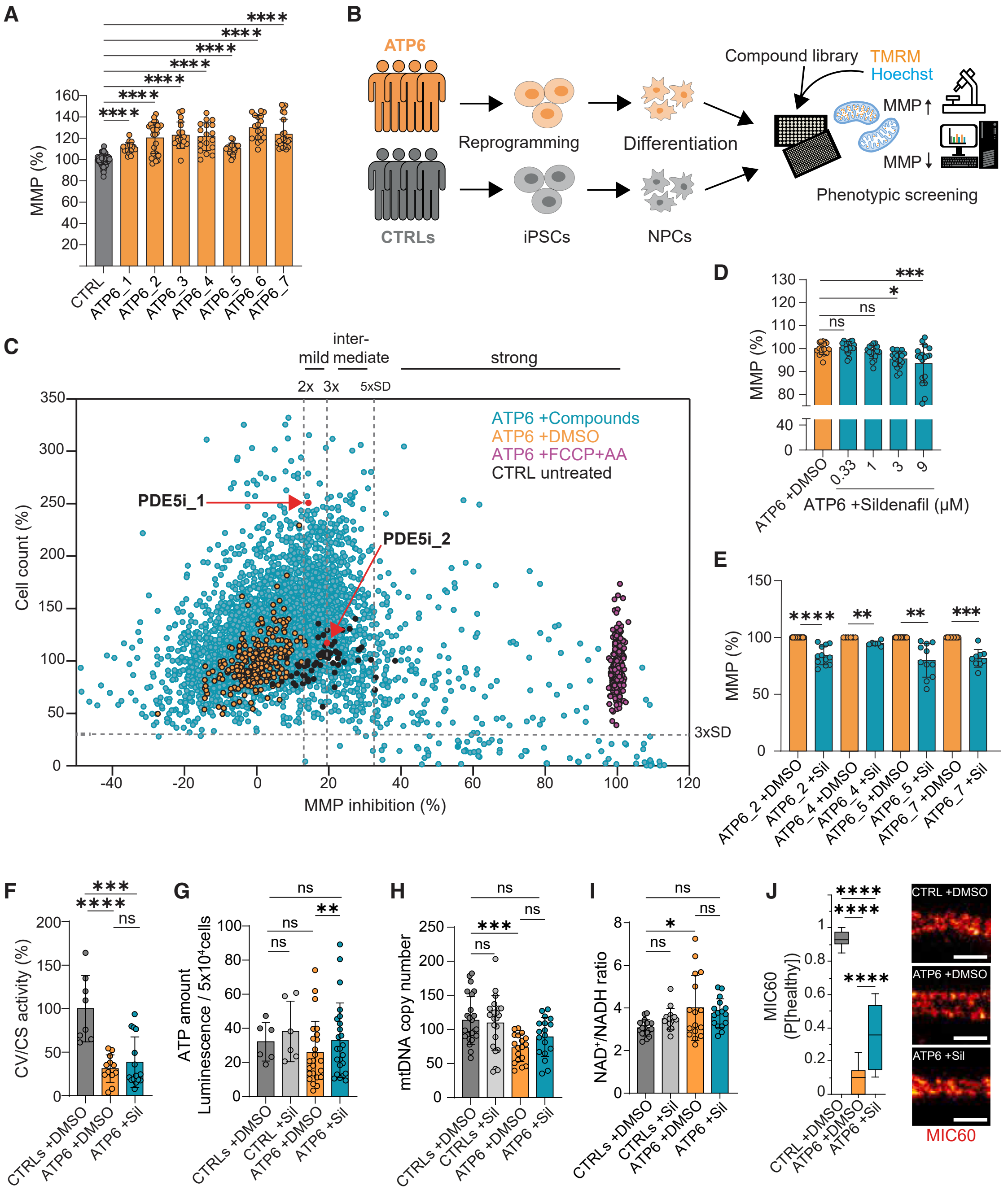

Figure 1. Compound screen in LS NPCs leads to identifying the PDE5i sildenafil

(A) HCA MMP quantification in LS NPCs (ATP6_1, ATP6_2, ATP6_3, ATP6_4, ATP6_5, ATP6_6, and ATP6_7) and control NPCs (CTRL_1). Dots: mean value/well, *n* = 3–5 independent experiments. *****p* < 0.0001; ordinary one-way ANOVA with Dunnett's multiple comparisons.

(B) Screening approach.

(C) Compound screen in LS NPCs (ATP6_2) based on MMP depolarization (TMRM) vs. cell count (Hoechst). Control NPCs: CTRL_1; PDE5i_1: T-0156, PDE5i_2: vardenafil hydrochloride.

(D) HCA MMP quantification in LS NPCs (ATP6_2) treated with sildenafil compared with DMSO. Dots: mean value/well, *n* = 4 independent experiments; **p* < 0.05, ****p* < 0.001, ns, not significant; ordinary one-way ANOVA with Dunnett's multiple comparisons.

(E) Cytofluorimetry MMP quantification in LS NPCs treated with sildenafil (Sil) compared with DMSO. Dots: individual values, *n* = 3 independent experiments. ***p* < 0.01, ****p* < 0.001, *****p* < 0.0001; two-tailed paired *t* test.

(F) CV activity normalized to citrate synthase (CS) activity in LS NPCs (ATP6_2, ATP6_4, ATP6_5, and ATP6_7) compared with control NPCs (CTRL_1 and CTRL_3). Dots: pool of 10–15 million cells, *n* = 3 independent experiments. ****p* < 0.001, *****p* < 0.0001; one-way ANOVA with Tukey's multiple comparisons.

(legend continued on next page)

and early lethality,[11] but *Surf1* KO mice failed to replicate LS phenotypes.[12,13] The most widely used model of LS is the homozygous *Ndufs4* KO mouse, characterized by progressive encephalopathy, growth retardation, and premature death.[14,15] This model has been used to propose therapeutic interventions, including antioxidants,[16–18] rapamycin,[19] interferon-gamma-targeting therapies,[20] cannabidiol,[21] or hypoxia.[22,23] Only a few of these strategies have been tested in LS individuals, and no successful results have been obtained.

New approach methodologies (NAMs) with LS patient-derived induced pluripotent stem cells (iPSCs)[24] have been instrumental in uncovering pathological mechanisms. These include neuronal outgrowth defects,[25] altered calcium homeostasis,[26,27] and glutamate toxicity in neuronal cultures,[28] as well as impaired cortical development and neuromorphogenesis in brain organoids.[25,29,30] Despite these advances, large-scale drug screens in iPSC models of mitochondrial disease have yet to be performed.

We previously demonstrated that iPSC-derived neural precursor cells (NPCs) are an effective drug discovery platform for mtDNA diseases.[27] LS NPCs carrying a *MT-ATP6* variant exhibited abnormal mitochondrial membrane potential (MMP), a feature that can be exploited for high-throughput screens.[31] Here, we leveraged this MMP phenotype to screen a library of 5,632 repurposable drug candidates in LS NPCs. We identified phosphodiesterase type 5 (PDE5) inhibitors as lead compounds and prioritized sildenafil for its safety profile.[32] Sildenafil rescued the neurodevelopmental disease signature, promoted neuronal outgrowth, and normalized calcium homeostasis in human LS models. *In vivo*, sildenafil extended the lifespan of *Ndufs4* KO mice and *SURF1* KO pigs. Mechanistically, sildenafil's action appeared to be mediated through cyclic GMP (cGMP)-dependent protein kinase 1 (PRKG1). Off-label treatment on an individual basis with sildenafil in six patients with LS carrying *MT-ATP6* variants improved muscle strength and resistance to metabolic crises. The data implicate sildenafil as a repurposable drug for mitochondrial disorders.

RESULTS

Repurposable drug screen in LS NPCs identifies PDE5i

To determine whether MMP hyperpolarization observed in LS NPCs carrying the m.9185T>C variant in the *MT-ATP6* gene[27] represented a robust phenotype, we generated NPCs from 7 LS patients carrying different *MT-ATP6* variants (3 m.9185T>C, 1 m.8993T>C, 2 m.8993T>G, and one m.9176T>G) (Figure S1A).[27,33–36] For controls, we used NPCs from 8 healthy individuals, including 2 patients' mothers carrying *MT-ATP6* variants at low heteroplasmy (<2%) (Figure S10H). LS NPCs expressed NPC markers similarly to control NPCs (Figures S1E and S1F) and retained mtDNA heteroplasmy of parental iPSCs (Figure S10H). LS NPCs showed defective bioenergetics (Figure S1C), disrupted MT-ATP6 protein expression (Figure S1B) and CV assembly structure (Figures S4A and S4B), and MMP hyperpolarization (Figure 1A).

We applied a well-curated library of 5,632 repurposable molecules[37] to modulate the MMP of LS NPCs. We used live-cell high-content analysis (HCA) based on tetramethylrhodamine methyl ester (TMRM) intensity[31] (Figures 1B, S2A, and S2B). Compounds were applied with 0.05% maximal concentration of DMSO, which was not toxic in LS NPCs (Figure S2C). We included MMP values from one control NPC line for baseline MMP after having confirmed that various control NPC lines displayed comparable MMP (Figure S2D). We established the Z′ factor[38] to be ∼0.68–0.85 across plates (Figures S2E–S2G) and identified 5 μM as the optimal screening concentration achieving an ∼5% hit rate with low toxicity (Figure S2H) and high reproducibility (Figure S2I).

We classified compounds based on their depolarizing effect in LS NPCs (MMP inhibition) relative to the standard deviation (SD) of DMSO-treated LS NPCs (SD = 6.51%). We identified 767 mild uncouplers (13.0%–19.5% inhibition, >2 SD), 520 intermediate uncouplers (19.5%–32.5% inhibition, >3 SD), and 187 strong uncouplers (>5 SD) (Figure 1C). We excluded toxic compounds based on cell count (cut-off: 29.86%). We focused on mild uncouplers that depolarized the MMP of LS NPCs to values similar to control NPCs (Figure 1C). Among those, we identified two PDE5 inhibitors (PDE5i), T-0156 and vardenafil hydrochloride, which showed dose-dependent MMP depolarization in LS NPCs without loss of viability (Figures S3A–S3D).

As our previous proof-of-concept screen in LS NPCs highlighted the PDE5i avanafil,[27] we prioritized PDE5i employed in pediatric settings. Sildenafil emerged as a strong candidate, given its safety profile in children treated for pulmonary arterial hypertension (PAH) or lymphatic malformations.[39–42] Sildenafil led to dose-dependent MMP depolarization in LS NPCs (Figure 1D) without toxicity (Figures S3E–S3G) and with a half-maximal inhibitory concentration (IC_{50}) of ∼3 μM at 16 h (Figure S3H). MMP normalization occurred similarly in LS NPCs carrying different *MT-ATP6* variants with overall MMP depolarization of ∼16% (Figure 1E). Sildenafil did not modify the MMP in control NPCs (Figures S3I and S3J).

Bioenergetically, sildenafil did not lead to a measurable improvement in CV activity (Figure 1F) or in CV assembly structure[43,44] (Figure S4C). The protein levels of known mitochondrial modulators were also not significantly impacted (Figures S4D and S4E). Nonetheless, sildenafil increased intracellular ATP in

(G) ATP content in control NPCs (CTRL_1 and CTRL_3) and LS NPCs (ATP6_2, ATP6_4, ATP6_5, and ATP6_7). Dots: biological replicates, *n* = 3 independent experiments. $^{**}p < 0.01$; mixed-effects model (equivalent to repeated-measures ANOVA) with multiple comparisons.

(H) mtDNA copy number in control NPCs (CTRL_1, *n* = 5–6; CTRL_2, *n* = 6; CTRL_3, *n* = 6; CTRL_4, *n* = 6) and LS NPCs (ATP6_2, *n* = 6; ATP6_4, *n* = 6; ATP6_7 *n* = 6). Dots: biological replicates, *n* = 3 independent experiments. $^{***}p < 0.001$; one-way ANOVA with Tukey's multiple comparisons.

(I) NAD^+/NADH ratio in control NPCs (CTRL_1, CTRL_2, CTRL_3, and CTRL_4) and LS NPCs (ATP6_2, ATP6_4, ATP6_5, and ATP6_7). Dots: individual values, *n* = 3 independent experiments. $^{*}p < 0.05$; unpaired two-tailed *t* test.

(J) Left, probability of MIC60 staining pattern of LS NPCs (ATP6_2) to be similar to that of control NPCs (CTRL_1). *n* = 3 independent experiments, comprising a total of 4,000 images. $^{****}p < 0.0001$; Kruskal-Wallis with Dunn's multiple comparisons. Right, representative STED images. Scale bar: 500 nm.
See also Figures S1–S4.

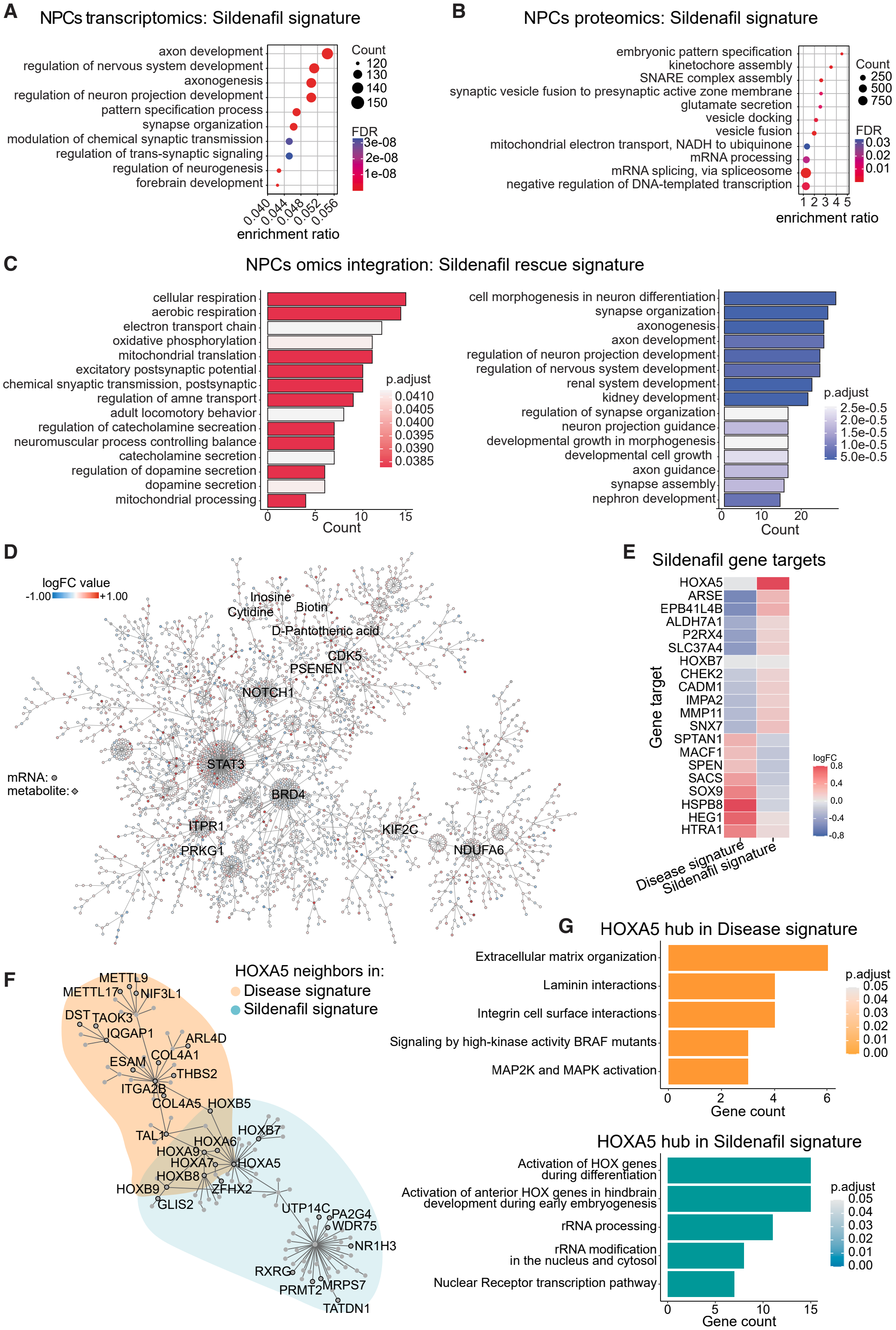

(legend on next page)

LS NPCs (Figure 1G) and restored mtDNA copy number (Figure 1H). The NAD$^+$/NADH ratio was also normalized (Figures 1I and S1D). Because *MT-ATP6* defects may disrupt mitochondrial cristae,[45] we analyzed the cristae junction regulator MIC60 with stimulated emission depletion (STED) microscopy.[46] We inspected the MIC60 labeling pattern of 4,000 STED images with a machine-learning approach by training a neural network classifier to distinguish control NPCs (P[healthy]-score = 1) from LS NPCs (P[healthy]-score = 0). Using images not used for training, we detected altered MIC60 localization in LS NPCs that were partially reversed by sildenafil (Figures 1J and S3K). Manual quantification of approximately 300 STED images yielded similar results (Figure S3L) and highlighted a peripheral MIC60 distribution pattern in LS NPCs that was restored by sildenafil (Figures S3M and S3N). Hence, sildenafil improved mitochondrial phenotypes in LS neural cells.

The PDE5i sildenafil ameliorates the LS disease signature by modulating neuronal development pathways

To investigate the mechanism of action of sildenafil, we performed multi-omics in 4 LS NPC lines (1 for each *MT-ATP6* variant: m.9185T>C, m.8993T>C, m.8993T>G, and m.9176T>G) and 4 healthy control NPC lines. The omics design identified (1) the disease signature by comparing DMSO-treated LS NPCs to DMSO-treated control NPCs and (2) the sildenafil signature by comparing sildenafil-treated LS NPCs to DMSO-treated LS NPCs (Figure S1G).

The disease signature included biological processes (BPs) related to nervous system and axon development and cellular components (CCs) implicated in the mitochondrial inner membrane and neuronal cell body in transcriptomics (Figures S5A and S5B), and mitochondrial translation and mitochondrial membrane in proteomics (Figures S5F, S5G, and S5I). The sildenafil signature affected similar pathways, including axon and nervous system development (Figure 2A) and mitochondrial inner membrane and neuronal cell body in transcriptomics (Figure S5C) and electron transport chain (ETC) in proteomics (Figures 2B and S5H). Genes restored by sildenafil (Figures S5D and S5E) included neuron-specific calcium sensor *CABP1*[47] (Table S1) and neurodevelopment-associated genes *HOXA5*[48,49] and *DBX1*[50] (Figure S5E; Table S1). Restored proteins included BAG4, protecting against ATP depletion-induced cell death,[51] downregulated in LS NPCs (Table S1) and upregulated after treatment (Figure S5J). No significant transcriptional changes were observed in sildenafil-treated control NPCs (Figure S5K).

Metabolomics identified metabolites important for brain energy metabolism, including creatine[52,53] and cysteine,[54] that were altered by the disease (Figure S4F) and normalized by sildenafil (Figure S4G; Table S1). Creatinine, a non-enzymatic breakdown product of creatine, was not normalized, possibly reflecting an increased use of creatine. The disease and sildenafil signatures also impacted the glutathione metabolism pathway (Figures S6A and S6B).

Multi-omics integration[55] revealed 796 molecules shared between the integrated signatures for disease and sildenafil, with 724 exhibiting opposite regulation. Hence, sildenafil reversed 33.5% of dysregulated molecules (724 over 2,160). The integrated signatures impacted signaling pathways (e.g., Notch and WNT) and axon guidance (Figures S6C and S6D). Reversed BPs included one group related to mitochondrial respiration and one related to morphogenesis and axon development (Figure 2C). The multi-omics map of the sildenafil rescue signature (including only transcriptomics and metabolomics, as proteomics did not show sufficiently significant changes) highlighted a network comprising metabolites (e.g., biotin and pantothenic acid) and genes related to ETC (e.g., *NDUFA6*) and development (e.g., *NOTCH1*, *BRD4*, and *STAT3*) (Figure 2D).

We identified 20 putative sildenafil targets whose gene expression was altered in LS NPCs compared with control NPCs and restored in LS NPCs treated with sildenafil (Figure 2E). The top responsive gene was *HOXA5* (logFC_diseased = −0.02, logFC_treated = +5.2). The *HOXA5* hub was involved in extracellular matrix organization in LS NPCs but became associated with differentiation and neurodevelopment upon treatment (Figures 2F and 2G). The *HOXA5* network may thus be dysregulated in LS, and its modulation by sildenafil might contribute to healthy neurodevelopment. Another key responder was *PRKG1*, a master regulator and downstream target of PDE5,[56] which was highlighted by the multi-omics map of the sildenafil rescue signature (Figure 2D). To monitor the expression of putative sildenafil-responsive genes, we treated LS NPCs grown in physiologically low glucose with 1 or 10 μM sildenafil for 6 and 24 h (Figures S6E and S6F). The treatments modulated the expression of sildenafil targets over time, including proliferation-related genes *BRD4*, *STAT3*, and *NOTCH1*[57,58]; synapsis-associated *NRG1*[59]; neuroinflammation-associated *P2RX4*[60]; and glucose metabolism-related *SLC37A4*.[61]

LS brain organoids show neurodevelopmental defects and highlight the impact of sildenafil on progenitor populations

We used cortical brain organoids to explore the impact of sildenafil on human neurodevelopment. In agreement with previous studies in LS brain organoids,[25,29,30] *MT-ATP6* variants impaired neurogenic zone formation (Figure 3A) and altered the ratio of early neurons to neural progenitors (Figure 3B). Two different protocols for generating cortical brain organoids showed

Figure 2. Neurodevelopmental impact of sildenafil revealed by multi-omics
(A) Top ten biological processes (BPs) in sildenafil-treated LS NPCs based on transcriptomics (FDR, false discovery rate).
(B) Top ten BPs in sildenafil-treated LS NPCs based on proteomics.
(C) BPs of 724 molecules reversed by sildenafil with logarithmic fold change (logFC) > 0 based on multi-omics integration.
(D) Multi-omics network of sildenafil signature in LS NPCs. Dot size: centrality in the network; dot color: logFC value.
(E) Putative sildenafil-responsive genes based on transcriptomics.
(F and G) Network analysis for *HOXA5* hub and associated pathways.
See also Figures S4–S6 and Table S1.

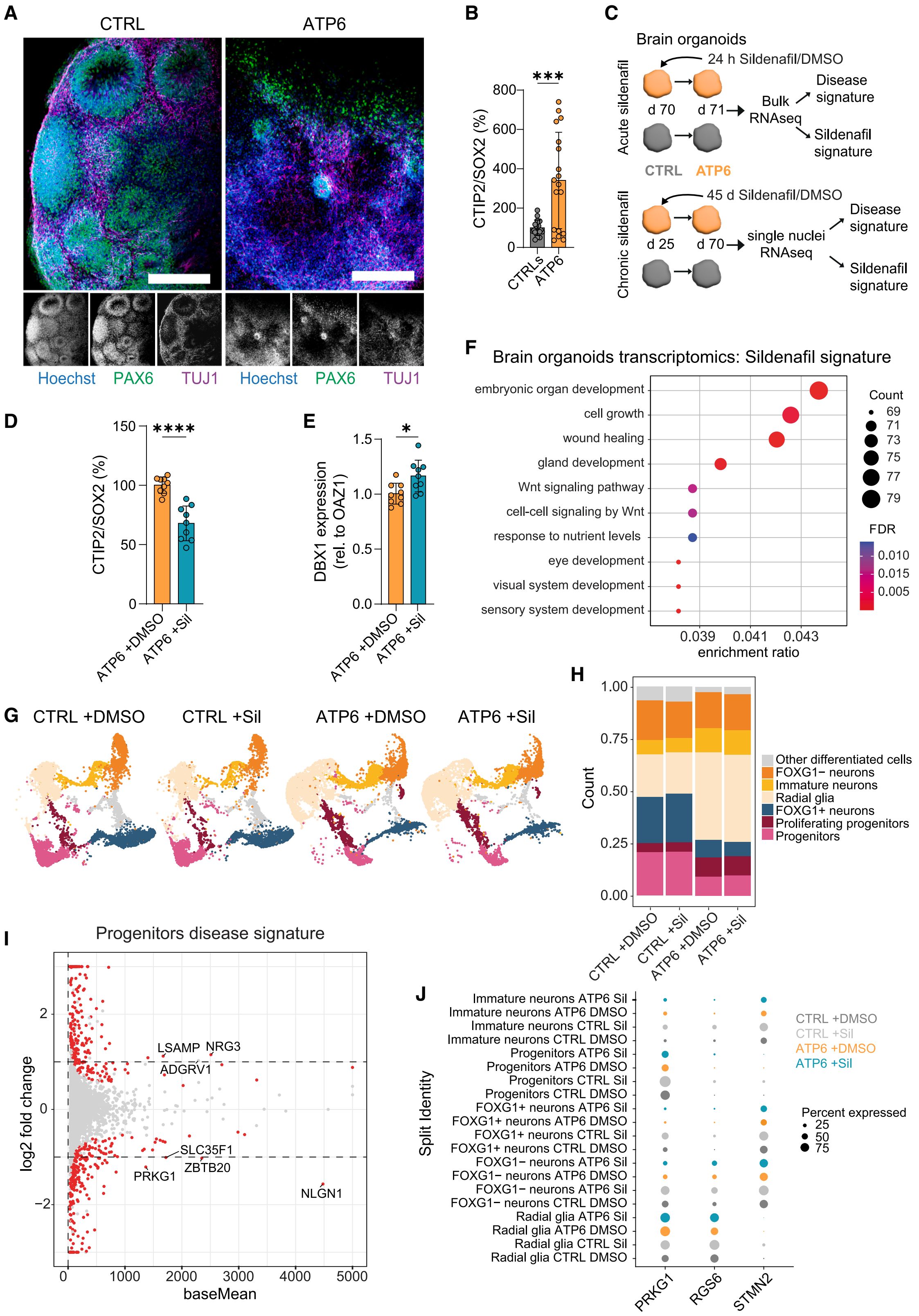

(legend on next page)

defective growth rates (Figure S7A). One protocol[62] showed size defects in LS organoids after 50 days in culture (Figure S7B); another protocol,[63] allowing initial homogeneous organoid shape, resulted in earlier growth defects in LS organoids that became less pronounced over time (Figure S7B). The results suggest that *MT-ATP6* variants might affect neural progenitor development.

We treated LS brain organoids with sildenafil for either 24 h (acute paradigm) or 45 days (chronic paradigm) (Figure 3C). *MT-ATP6* variants disrupted BPs related to synapses and neuronal projections (Figure S7E) and CCs related to neuronal cell bodies and synapses (Figure S7F). The acute sildenafil signature modulated pathways related to embryonic development and Wingless-related integration site (WNT) signaling (Figure 3F) and corrected gene defects (Figures S7C and S7D), including *WDR45B*, which was downregulated in LS brain organoids (Table S1) and upregulated by sildenafil (Figure S7D), and whose variants are associated with neurodevelopmental disorders.[64] Sildenafil also rescued the ratio of early neurons to neural progenitors (Figure 3D) and upregulated *DBX1* (Figure 3E).

To dissect the cell populations affected by *MT-ATP6* variants and chronic sildenafil, we performed single-nucleus RNA sequencing (snRNA-seq) (Figure 3C). Unsupervised clustering highlighted 9 clusters (Figure S8A): clusters 0 and 3 for radial glia, clusters 4 and 8 for progenitors, cluster 6 for proliferating progenitors, cluster 5 for immature neurons, cluster 2 for FOXG1-positive neurons, cluster 1 for FOXG1-negative neurons, and cluster 7 for other cell types (Figure S8B). This annotation revealed that *MT-ATP6* variants impaired neuronal commitment, with alterations in radial glia, progenitors, and FOXG1-positive neurons (Figures 3G and 3H). The disease signature involved the downregulation in the progenitor population of *PRKG1* and *NLGN1*, a regulator for synapse development[65] (Figure 3I), and the downregulation in the neuronal population of genes impacting neurite outgrowth, such as *STMN2*[66] (Figure S8D; Table S1). The sildenafil signature upregulated neuronal outgrowth-associated genes, such as *RGS6*[67] (Figures S8C and S8D; Table S1). The effect of sildenafil was mostly evident in radial glia and progenitors (Figure S8C; Table S1). Whereas *STMN2* was mainly present in FOXG1-positive neurons and immature neurons, *RGS6* was found mainly in radial glia, and *PRKG1* in radial glia and progenitors (Figures 3J and S8D). The glycolytic signature, suggested to be an indicator of brain organoid stress,[68] was not altered, indicating that neither *MT-ATP6* variants nor sildenafil posed additional stress (Figure S8E). Altogether, LS disrupted brain organoid development by impairing early neuronal organization of radial glia and progenitor populations, and sildenafil specifically affected those populations.

Sildenafil improves calcium homeostasis and neurite outgrowth in LS neural models

We examined the functional consequences of sildenafil in LS neural cells. Given the reported calcium dysregulation[26,27] and the known deterioration of LS patients upon metabolic decompensation,[3] we induced acute metabolic stress in LS brain organoids to monitor their intracellular calcium response. We dissected brain organoids on days 70–74 to prepare cortical brain organoid slices (cBOSs),[69] which we grew until day 129 and then treated with sildenafil for 24 h before applying acute metabolic stress (2 min of glucose deprivation and inhibition of glycolysis [GLY] and OXPHOS) (Figure 4A). The calcium response to metabolic stress was more pronounced and premature in LS cBOS compared with control cBOS, suggesting increased susceptibility to metabolic imbalance (Figures 4B and 4C). Pre-treatment with sildenafil in LS cBOS reduced their calcium load after metabolic stress and also their peak calcium amplitude (Figures 4B and 4C). Hence, sildenafil might prevent excessive decompensation in LS neuronal cells under acute metabolic stress.

To investigate the interplay between calcium and bioenergetics in treated LS neural cells, we applied a mathematical model[70] that coupled cytosolic calcium dynamics with mitochondrial function, incorporating F_1F_0 ATPase activity (F1F0), GLY, the adenine nucleotide translocator (ANT), NADH production via the aspartate-glutamate carrier (AGC), and NADH oxidation in ETC (o). Based on our previous calcium modeling,[71–73] we integrated additional fluxes through the plasma membrane calcium ATPase (PMCA), the sarco-plasmic/endoplasmic reticulum calcium ATPase (SERCA), and IP_3 receptors (IP3Rs) (Table S2). Following global sensitivity analysis[70] (Figure S9A), the model recapitulated the pattern of calcium traces measured in LS cBOS (Figure S9B). Combining a high rate of F1F0 with a low rate of IP3R (Figure S9C) reproduced the reduction of calcium peak in sildenafil-treated LS cBOS under stress (Figures 4B and 4C) and key features observed in sildenafil-treated LS NPCs, including MMP reduction (Figures 1D and 1E), slight NADH reduction (Figure S1D), and ATP increase (Figure 1G). Other combinations failed to recapitulate sildenafil effects (Figures S9D and S9E). The modeling thus suggested that

Figure 3. Sildenafil affects progenitor populations in LS brain organoids

(A) Representative images of day 35 brain organoids from controls (CTRL_2) and LS (ATP6_7). Scale bar: 200 μm.

(B) Differentiation ratio in day 70 brain organoids from controls (CTRL_1 and CTRL_2) and LS (ATP6_4 and ATP6_7). Five organoids per line per independent experiment ($n = 3$). ***$p < 0.001$; unpaired two-tailed *t* test.

(C) Brain organoid experiments to assess acute (10 μM for 24 h) and chronic (10 μM for 45 days) sildenafil treatment signatures.

(D) Differentiation ratio in day 70 brain organoids from LS (ATP6_4). Ten organoids per line per independent experiment ($n = 3$). ****$p < 0.0001$; unpaired two-tailed *t* test.

(E) qPCR analysis of *DBX1* in day 70 LS brain organoids (ATP6_4). Ten organoids per line per independent experiment ($n = 3$). *$p < 0.05$; unpaired two-tailed *t* test.

(F) Top-ten BPs of acute sildenafil signature based on transcriptomics.

(G and H) Population distribution and related quantification in chronic sildenafil-treated brain organoids.

(I) Disease signature in the progenitor population of brain organoids.

(J) Expression patterns of *PRKG1*, *RGS6*, and *STMN2* across distinct populations of brain organoids.

See also Figures S7 and S8 and Table S1.

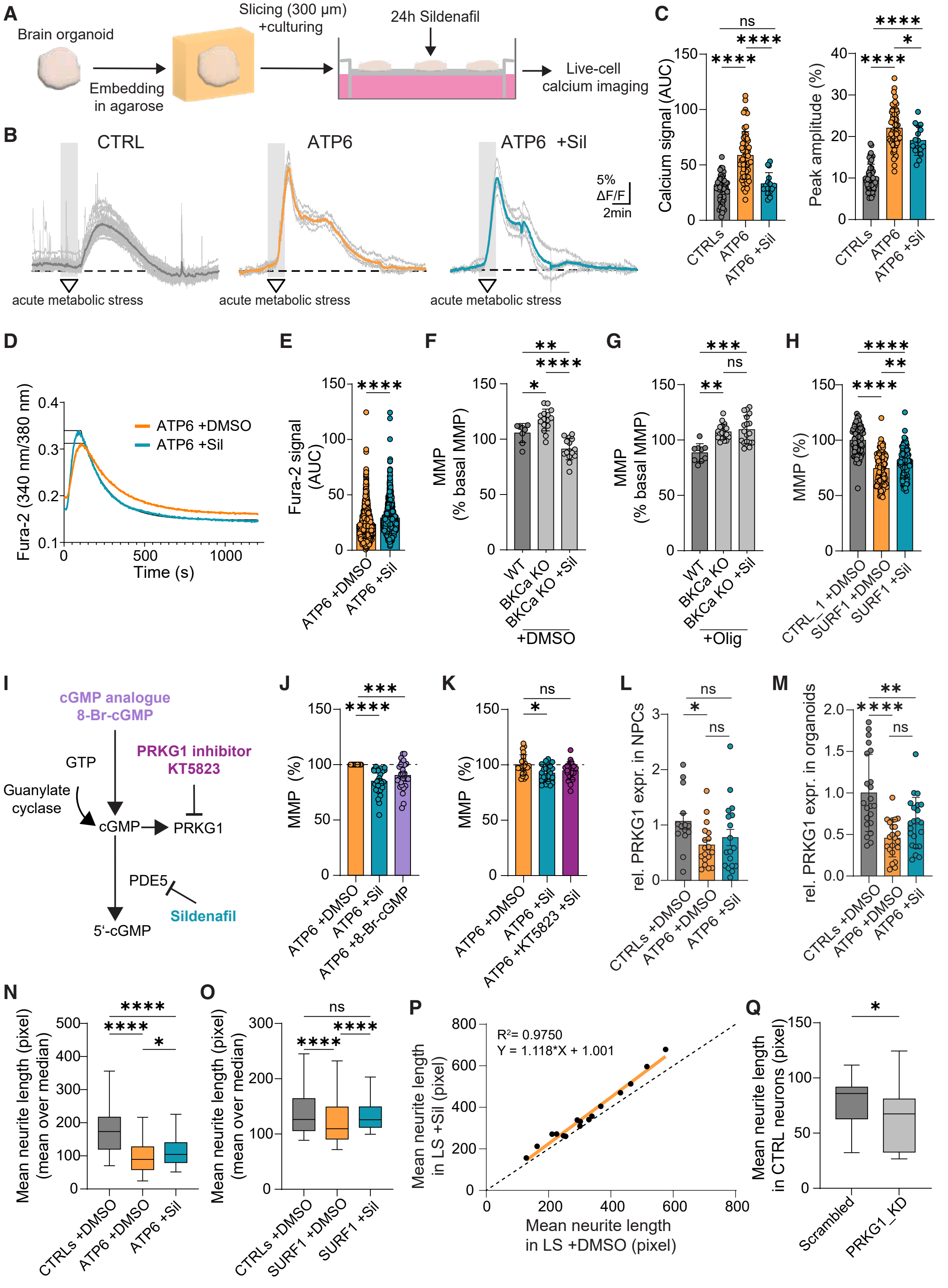

Figure 4. Sildenafil ameliorates calcium homeostasis and neurite outgrowth

(A) cBOS generation for live-cell calcium imaging.

(B) Representative calcium traces of cBOS from control (CTRL_2) and LS (ATP6_7). Gray lines: individual cells; colored lines: average traces.

(legend continued on next page)

sildenafil's action may be mimicked by increasing CV activity together with decreasing calcium release from the endoplasmic reticulum (ER), in turn improving cellular bioenergetics.

We analyzed ER calcium with the SERCA inhibitor thapsigargin. In the absence of extracellular calcium, pre-treatment with sildenafil in LS NPCs increased the thapsigargin-induced cytoplasmic calcium signal (Figures 4D and 4E), possibly indicating higher ER calcium storage or modulation of mitochondrial calcium homeostasis.[74,75] A faster decline of calcium in sildenafil-treated cells (Figure 4D) could imply reduced calcium release from the ER through IP3R, as suggested by the model, or enhanced cytosolic calcium efflux to the extracellular space through the sodium-calcium exchanger (NCX) or the PMCA because of increased cytosolic ATP levels by sildenafil or augmented uptake into mitochondria. To indirectly address mitochondrial calcium, we investigated big-conductance calcium-activated potassium (BKCa) channels, which are localized in the plasma and mitochondrial membrane[76] and have been implicated in sildenafil's action.[77,78] As previously shown,[79] human BKCa KO cells[80] displayed increased MMP compared with wild type (WT) (Figures 4F and 4G). Sildenafil normalized MMP when BKCa KO cells were incubated in DMSO (Figure 4F) but not when they were acutely exposed to the CV inhibitor oligomycin (Figure 4G). The results suggest that BKCa channels may contribute to the action of sildenafil on MMP when cells lack a functional CV and that residual CV activity is necessary for the restorative effect of sildenafil, as indicated by the model.

These findings raised the possibility that MMP normalization by sildenafil may not be due to direct mitochondrial uncoupling. To test this, we employed NPCs carrying a variant in the nuclear gene *SURF1*[25] (Figure S10H). The MMP of *SURF1* mutant NPCs was depolarized compared with that of isogenic control NPCs (Figure 4H). Nonetheless, sildenafil still restored MMP (Figure 4H). Hence, sildenafil might also be beneficial in other forms of LS where MMP is depolarized.

We applied chemical manipulation of the PDE5 pathway to prove its involvement in the MMP rescue of LS NPCs (Figure 4I). The cGMP analog 8-Br-cGMP recapitulated the MMP amelioration seen with sildenafil (Figure 4J). Inhibition of the downstream target PRKG1 with KT5823 blunted the effect of sildenafil on MMP normalization (Figure 4K). Indeed, PRKG1 levels were reduced in *MT-ATP6* mutant NPCs (Figures 4L and S10A), *MT-ATP6* mutant brain organoids (Figure 4M), and *SURF1* mutant neurons and brain organoids (Figure S10B).

We quantified the effect of sildenafil on neuronal outgrowth[81] of dopaminergic neurons (Figure S10C). In agreement with previous findings,[25,30] *MT-ATP6* mutant neurons and *SURF1* mutant neurons exhibited reduced neurite length (Figures 4N, 4O, and S10D). Sildenafil promoted neurite outgrowth in LS neurons (Figures 4N, 4O, and S10D). This improvement was specific to LS neurons (carrying *MT-ATP6*, *SURF1*, or *NDUFS4* variants) (Figure 4P) and was not observed in control neurons (Figure S10E). PRKG1 signal was reduced in LS neurons (Figure S10F), and PRKG1 knockdown in control neurons recapitulated the neurite growth defects seen in LS neurons (Figure 4Q). Because PRKG1 is involved in both calcium homeostasis and neurite outgrowth,[82–86] its dysregulation in LS might underscore its role as a therapeutic target that could contribute to the sildenafil response (Figure S10G).

Sildenafil extends the lifespan of LS animals and crosses the human BBB

To address the therapeutic potential of sildenafil *in vivo*, we employed the germline *Ndufs4* KO mouse.[14,15] Sildenafil was added to the drinking water of the animals starting on day 25. The treatment extended the lifespan of *Ndufs4* KO mice (Figure 5A) and alleviated muscle weakness and ataxia by partially correcting defective energy expenditure (Figure 5B). Upon placing LS mice in metabolic chambers (Figure S11A), we observed improved oxygen consumption and carbon dioxide production with sildenafil (Figure 5C), possibly indicating enhanced

---

(C) Area under the curve (AUC) and peak intracellular calcium in cBOS from controls (CTRL_1, $n = 10$; CTRL_2, $n = 40$) and LS (ATP6_7, $n = 58$; ATP6_7 +Sil, $n = 16$). Dots: individual cells. *$p < 0.05$, ****$p < 0.0001$; two-tailed Mann-Whitney U test.

(D and E) Mean calcium trace and AUC quantification of intracellular calcium in LS NPCs (ATP6_2, ATP6_4, ATP6_5, and ATP6_7). Dots: individual cells, n = at least 3 independent experiments per line. ****$p < 0.001$; unpaired two-tailed t test.

(F and G) HCA MMP quantification in WT and BKCa KO cells after DMSO (F) or oligomycin (G). $n = 3$ independent replicates. *$p < 0.05$, **$p < 0.01$, ****$p < 0.001$, ****$p < 0.0001$; one-way ANOVA with Tukey's multiple comparisons test (F) and Kruskal-Wallis with Dunn's multiple comparisons (G).

(H) HCA MMP quantification in *SURF1* mutant NPCs (SURF1_1) and isogenic control NPCs (CTRL_1). Dots: mean value/image, $n = 3$ independent experiments. **$p < 0.01$, ****$p < 0.0001$; ordinary one-way ANOVA with Holm-Šídák's multiple comparisons.

(I) PDE5-PRKG1 pathway and modulations.

(J) Cytofluorimetry MMP quantification in LS NPCs (ATP6_2, ATP6_4, ATP6_5, and ATP6_7). Dots: individual values, $n = 7$ independent experiments. ***$p < 0.001$, ****$p < 0.0001$; one-way ANOVA with Tukey's multiple comparisons.

(K) HCA MMP quantification in LS NPCs (ATP6_2). Dots: mean value/image, $n = 3$ independent experiments. *$p < 0.05$; one-way ANOVA with Dunnett's T3 multiple comparisons.

(L) PRKG1 protein expression in control NPCs (CTRL_1, CTRL_2, CTRL_3, CTRL_4, and CTRL_5) and LS NPCs (ATP6_2, ATP6_4, ATP6_5, and ATP6_7) from immunoblots (Figure S10A), $n = 5$ independent experiments. *$p < 0.05$; unpaired two-tailed t test.

(M) qPCR analysis of *PRKG1* in day 70 brain organoids from controls (CTRL_1 and CTRL_2) and LS (ATP6_4 and ATP6_7). Five organoids per line per independent experiment ($n = 3$). **$p < 0.01$****, $p < 0.0001$; two-tailed Mann-Whitney U test.

(N and O) Neurite outgrowth in neurons from *MT-ATP6* variants (ATP6_2, $n = 2$; ATP6_4, $n = 1$) and controls (CTRL_1, $n = 2$; CTRL_2, $n = 2$; and CTRL_3, $n = 1$), and from *SURF1* variant (SURF1_1, $n = 3$) and isogenic control (CTRL_1, $n = 3$). *$p < 0.05$, ****$p < 0.0001$; Kruskal-Wallis with Dunn's multiple comparisons.

(P) Linear regression (sildenafil over DMSO) of mean neurite length in LS neurons (ATP6_2, $n = 3$; ATP6_4, $n = 1$; ATP6_7, $n = 3$; SURF1_1 $n = 3$; NDUFS4_1, $n = 3$; NDUFS4_2, $n = 3$). Dots: individual experiments. Black dotted line: hypothetical linear regression with no effect ($y = x$ or slope = 1).

(Q) Neurite outgrowth in control neurons (CTRL_1), $n = 3$ independent experiments. *$p < 0.05$; unpaired two-tailed t test.

See also Figures S9 and S10 and Table S2.

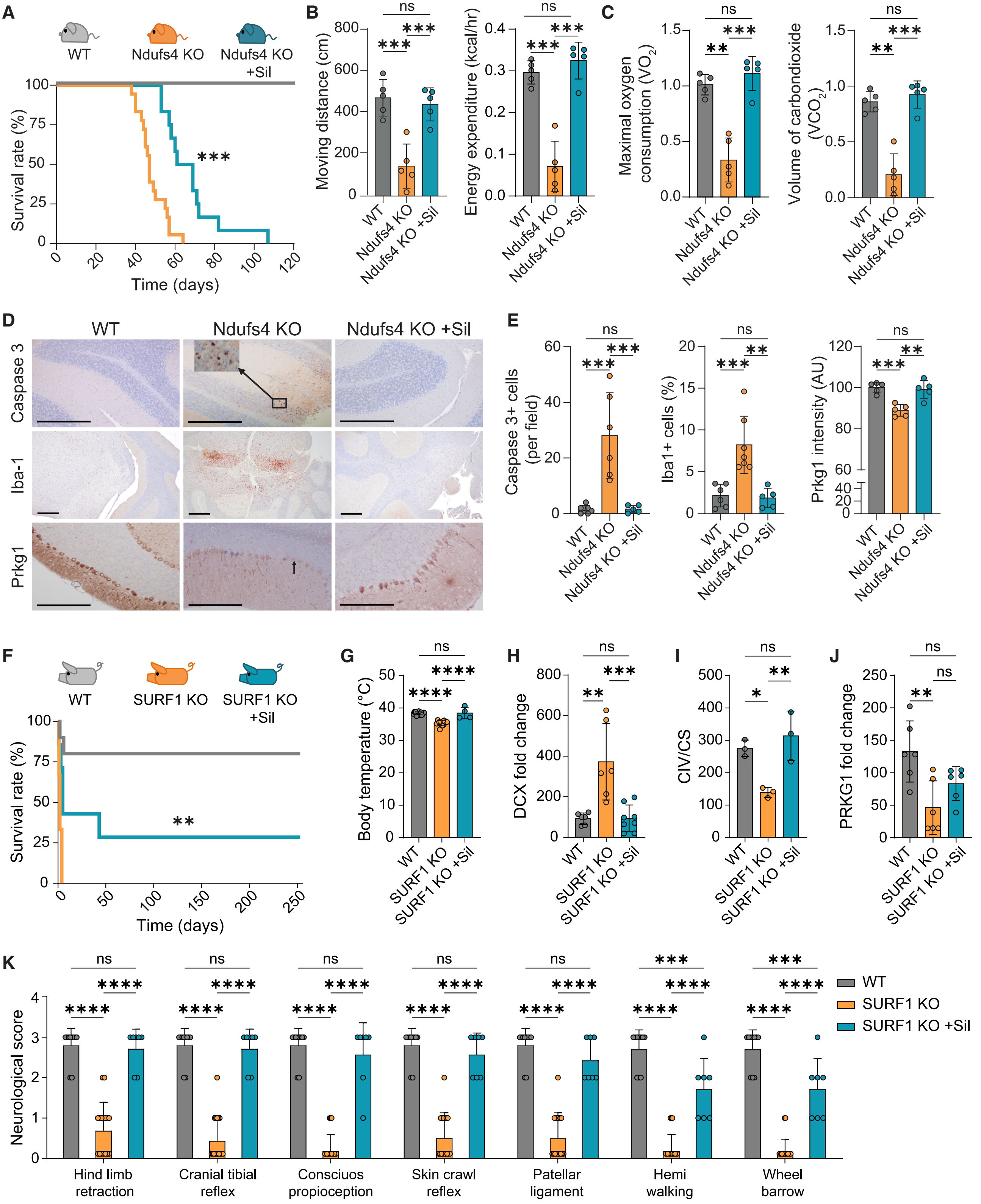

(legend on next page)

metabolic fitness. Cardiac bradyarrhythmia and dysfunction were also ameliorated (Figure S11B).

Consistent with previous observations,[14,87,88] LS mice showed cleaved caspase-3 staining in the cerebellum and brain stem regions associated with increased Iba1 staining,[89] suggestive of cell death and microglial activation (Figures 5D and 5E). The number of cells positive for caspase-3 or Iba1 decreased in sildenafil-treated LS mice (Figures 5D and 5E). The loss of Purkinje cells of the cerebellum was also ameliorated (Figures S11C and S11D). The expression of Prkg1, which is particularly evident in normal cerebellar Purkinje neurons,[15] was reduced in LS mice and rescued by sildenafil (Figures 5D and 5E).

Next, we employed *SURF1* KO pigs, which exhibit severe neurodevelopmental impairment.[11] *SURF1* KO piglets were treated immediately at birth ($n = 3$ animals with 2.1 mg/kg/day, $n = 4$ animals with 0.5 mg/kg/day). Sildenafil improved animal responsiveness, mobility, and suckling behavior, leading to lifespan extension once the unstable perinatal phase was overcome (Figure 5F). Some LS pigs survived beyond day 261 despite reduced body weight (98 kg vs. 140–170 kg in age-matched controls). Sildenafil increased the body temperature of LS pigs, suggesting an effect on systemic metabolism (Figures 5G and S11F). The expression of NPC-associated doublecortin (DCX) was normalized by sildenafil (Figures 5H and S11G), indicating neurodevelopmental amelioration. CIV activity was also restored (Figure 5I). Reduced PRKG1 levels in the basal ganglia of LS pigs increased with treatment in most animals (Figures 5J and S11G). By adapting the Newcastle Pediatric Mitochondrial Disease Scale (NPMDS), we observed improvement in multiple domains of neuromotor integrity (Figures 5K and S11E). Collectively, the *in vivo* data highlighted the potential clinical effectiveness of sildenafil and underscored PRKG1 as one of its mechanistic targets.

In some LS pigs treated with high sildenafil doses, we noticed microhemorrhages (Figure S11H). We further assessed toxicity using LS iPSC-derived cardiomyocytes (Figure S12A). Only high concentrations of sildenafil (>50 μM) appeared to be cardiotoxic (Figures S12B–S12D), as 10 μM sildenafil did not affect cell viability in LS cardiomyocytes (Figures S12B–S12D) and did not alter their glycolytic rate (Figure S12E). The findings are in agreement with the higher mortality rate seen in children with PAH treated with high sildenafil doses.[40]

We then probed the blood-brain barrier (BBB) permeability of sildenafil using an iPSC-based model[90] (Figure 6A). Similar to control brain capillary endothelial cells (BCECs), LS BCECs showed correct morphology and marker expression (Figure 6B) as well as monolayer integrity and transendothelial electrical resistance (TEER) (Figures S12F and S12G). The permeability of sildenafil and sildenafil citrate (the active pharmacological substance applied orally in clinical applications) in LS BCECs was similar to that of control BCECs (Figure 6C). The results are consistent with permeability values of sildenafil reported in other settings[91] and imply that sildenafil can effectively cross the BBB in LS.

Sildenafil treatment on an individual basis improved clinical outcome in six LS patients

Because sildenafil can be used safely in pediatric conditions,[39–42] we initiated off-label treatment on an individual basis with sildenafil in six LS patients carrying *MT-ATP6* variants (Tables 1 and S3). All patients showed cranial magnetic resonance imaging (cMRI) signs consistent with LS lesions (Figures 6E and S12H). From patient 1, we also obtained iPSCs (line ATP6_7), which were used to generate NPCs and brain organoids (Figure S10H). When selecting the sildenafil dosage, we referred to the trial STARTS-1 (Sildenafil in Treatment-Naive Children, Aged 1 to 17 Years, With Pulmonary Arterial Hypertension)[41] and the trial STARTS-2[40] in children with PAH. Given the potential toxic effects of high dosages, we only considered low (0.66–1.49 mg/kg/day) or medium dosages (1.50–3.00 mg/kg/day). Two patients/guardians opted for low dosages and four for medium dosages. Mass spectrometry quantification of total sildenafil concentration in the plasma[91] showed a plasma concentration of $\sim$1 μM (Figure 6D), which is close to the IC_{50} value of 3 μM that was found effective for normalizing MMP in LS NPCs (Figure S3H).

To monitor the occurrence of adverse reactions, we asked patients/guardians to respond to a questionnaire on side effects after 6 months of sildenafil use (Table S4). In patient 3, sildenafil had to be discontinued due to a rash, even though the frequent episodes of sudden muscle weakness were resolved during sildenafil medication and returned once the drug was discontinued (Tables 1 and S4). In all the other cases, sildenafil was well

Figure 5. Sildenafil extends the lifespan of small and large mammalian models of LS

(A) Kaplan-Meier survival curve of treated ($n = 18$) and sildenafil-treated *Ndufs4* KO mice ($n = 12$). $***p < 0.001$; log-rank (Mantel-Cox) test.

(B and C) Functional parameters in a metabolic chamber with 42- to 45-day-old *Ndufs4* KO mice ($n = 15$, 5 independent experiments). $**p < 0.01$, $***p < 0.001$; ANOVA post hoc analysis.

(D and E) Representative immunohistochemistry and quantification in 50-day-old *Ndufs4* KO mice. $**p < 0.01$, $***p < 0.001$; ANOVA post hoc analysis. Scale bar: 500 μm.

(F) Kaplan-Meier survival curve of WT pigs ($n = 10$), untreated *SURF1* KO pigs ($n = 16$), and sildenafil-treated *SURF1* KO pigs ($n = 3$ with 2.1 mg/kg/day, $n = 4$ with 0.5 mg/kg/day). $**p < 0.01$; log-rank (Mantel-Cox) test.

(G) Body temperature in *SURF1* KO pigs. $****p < 0.0001$; one-way ANOVA with Tukey's multiple comparisons.

(H) DCX protein expression in basal ganglia of *SURF1* KO pigs from immunoblots (Figure S11G). $n = 3$ replicates per sample. $***p < 0.001$, $**p < 0.01$; one-way ANOVA with Tukey's multiple comparisons.

(I) CIV activity normalized to citrate synthase (CS) activity in basal ganglia of *SURF1* KO pigs. $n = 3$ replicates per sample. $**p < 0.01$, $*p < 0.05$; one-way ANOVA with Tukey's multiple comparisons.

(J) PRKG1 protein expression in basal ganglia of *SURF1* KO pigs from immunoblots (Figure S11G). $n = 3$ replicates per sample. $**p < 0.01$; one-way ANOVA with Tukey's multiple comparisons.

(K) Neurological score in *SURF1* KO pigs. $****p < 0.0001$, $***p < 0.001$; two-way ANOVA with Tukey's multiple comparisons.

See also Figure S11.

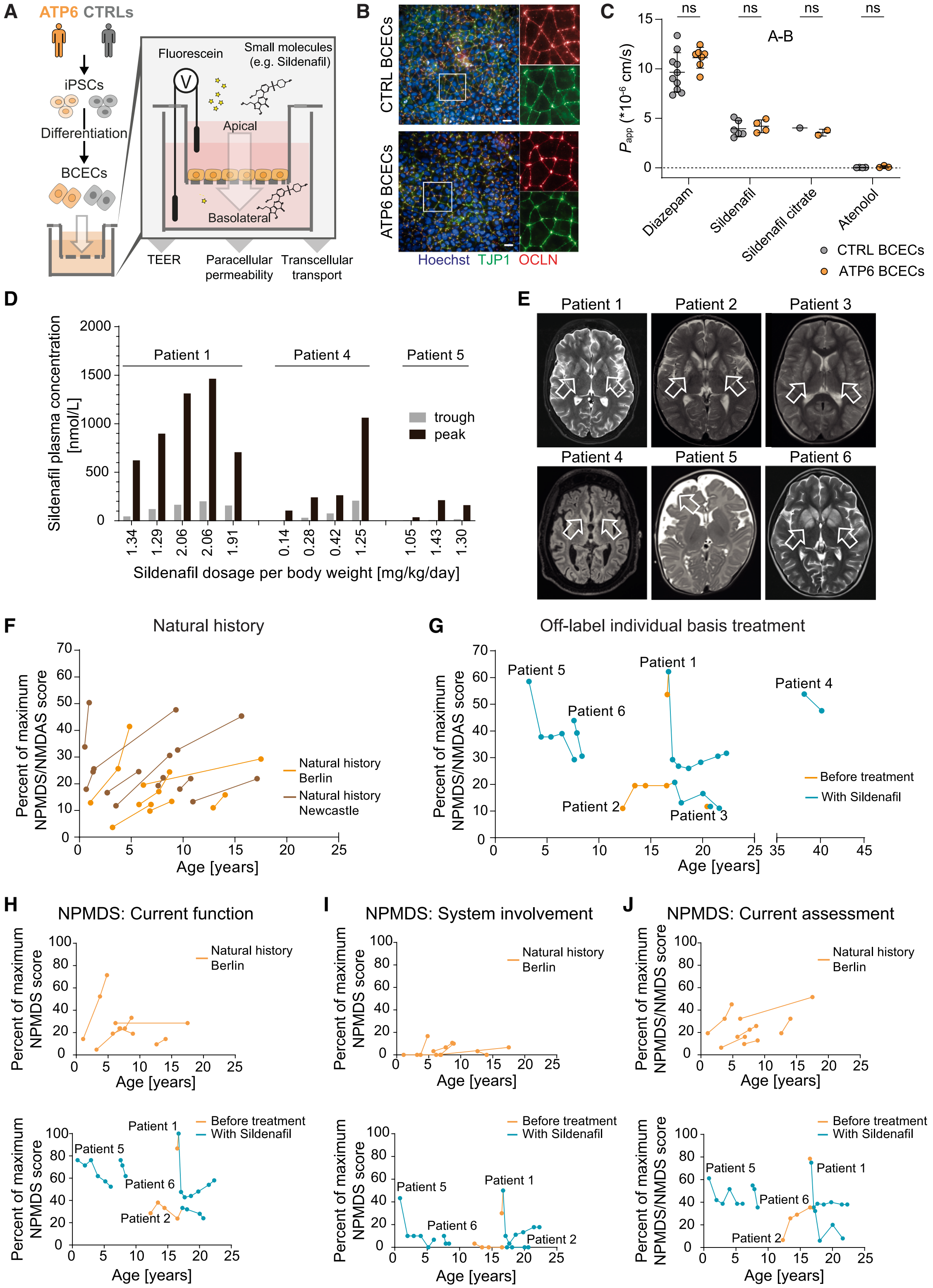

Figure 6. Sildenafil crosses the BBB and improves clinical features in six LS patients with *MT-ATP6* variants

(A) iPSC-derived BBB model.

(B) Representative immunostaining of BCECs from controls (CTRL_8) and LS (ATP6_2). Scale bar: 20 μm.

(legend continued on next page)

tolerated (Table S4), leading to improvement in motor function and development (Tables 1 and S3). Patient 5 showed protection from metabolic crises that had occurred nearly monthly before sildenafil treatment, while mild improvements in cognitive abilities were reported for patients 4 and 6 (Tables 1 and S3).

We assessed disease progression using the NPMDS[92] or the Newcastle Mitochondrial Disease Adult Scale (NMDAS).[93] These rating scales cover multiple aspects of mitochondrial disease, including clinical assessments and quality of life. The total score describes the overall severity of disease burden and typically increases over time.[92,93] The rise of NPMDS/NMDAS was evident in LS patients with *MT-ATP6* variants previously described in a cohort in Newcastle[94] (Δ8.8 percent points per year [SD = 11.4]) (Figure 6F) and in our cohort in Berlin[95] (Δ3.4 percent points per year [SD = 2.2]) (Figure 6F). Remarkably, NPMDS/NMDAS scores of the six sildenafil-treated patients decreased or showed reduced rates of increase over time (Figure 6G). The effect was evident across all dimensions of NPMDS (Figures 6H–6J). In patients 1, 5, and 6, sildenafil was started during a metabolic crisis, which resolved rapidly and led to a rapid drop in NMDAS/NPMDS. The subsequent NPMDS/NMDAS increase seen in patient 1 may be due to natural progression of the disease or reduced compliance. Overall, chronic treatment on an individual basis with sildenafil showed clinical improvements in LS patients carrying *MT-ATP6* variants.

DISCUSSION

Sildenafil is a well-studied molecule in clinical applications.[32] In addition to its use in adult men with erectile dysfunction,[96] sildenafil can treat PAH and rare lymphatic malformations in children.[39–42] Recent studies suggest that it might be a repurposable candidate for nervous system disorders.[97] Sildenafil use was associated with reduced risk of developing Alzheimer's disease (AD) and promoted neuronal outgrowth in AD iPSC-derived neurons.[98,99] Sildenafil lowered cognitive decline in mouse models of Huntington's disease (HD)[100,101] and increased motor and cognitive performance in HD individuals.[102] It also alleviated neuropathological signs in animal models of multiple sclerosis[103] and ischemic stroke.[104] In this study, we found that sildenafil might slow down the neurological decline of the severe mitochondrial brain disease LS. Sildenafil increased the lifespan of two mammalian models of LS. One treated pig remained clinically stable for over 6 months, an unprecedented health span and lifespan extension in this model. In treated LS individuals, the reduction of the upward sloping trend in the NPMDS/NMDAS score over time possibly implies that sildenafil modified the disease trajectory.

Sildenafil releases cGMP, which has a wide range of functions, likely resulting in a poly-pharmacological mode of action.[32] Sildenafil showed enhanced neurogenesis in mice,[105,106] as cGMP and PRKG1 modulated neurotransmitter release, neuronal survival, and neurite formation.[82–85] Mice deficient for Prkg1 exhibit impaired axon guidance and connectivity.[86] Consistently, we found that the signature of sildenafil primarily involved the regulation of neurodevelopment, and it acted specifically on progenitors and radial glia populations. LS neural cells showed reduced PRKG1 levels, and knockdown of PRKG1 in healthy neurons recapitulated the branching defects seen in patient cells. In mouse brain, *Prkg1* is known to be highly expressed in Purkinje cells, where its selective depletion results in motor learning defects.[107] Here, we found that treatment with sildenafil increased Prkg1 levels in LS mice and some LS pigs, potentially promoting neuronal morphogenesis and connectivity.

In addition to its neurological impact, sildenafil might induce mitochondrial biogenesis and oxygen consumption,[108,109] as PRKG1 may represent a regulator of energy homeostasis.[110] This is supported by our findings showing that PRKG1 inhibition blunted MMP normalization by sildenafil. Sildenafil also reversed changes in mitochondrial cristae junction distributions that may reflect cristae morphology defects caused by *MT-ATP6* variants.[45] We postulate that the bioenergetic improvement and MMP normalization by sildenafil may be related to its action on calcium homeostasis. Modulation of BKCa channels has been implicated in the sildenafil effect in other disease contexts[77,78] and neuronal calcium signaling can be mediated by PRKG1.[111,112] However, because PRKG1 protein levels were not fully normalized in all LS models, it is possible that sildenafil might enhance PRKG1 enzymatic activity rather than its protein abundance.[56] In fact, continuous application of the cGMP analog 8-Br-cGMP can reduce PRKG1 expression.[113] Further dissection of this pathway is required.

Whether the restorative effects of sildenafil seen in LS are linked to its vasodilatory mechanisms[32] remains to be studied. The increase in blood flow and oxygen delivery to muscle and brain tissue may potentially contribute to beneficial metabolic effects. Sildenafil led to vascular and metabolic improvements in individuals with AD[114] and in subjects with vascular cognitive impairment.[115] The effect of sildenafil on the vasculature[32] and the beneficial consequences of hypoxia seen in animal models of LS[22,23] might indicate that modulation of brain vascularization and associated oxygenation[116] could represent important therapeutic targets in LS.

Our findings underscore the power of conducting drug discovery studies driven by iPSC models. Similar strategies could

---

(C) Permeability coefficient (*p*app) in the apical-basolateral (AB) media of control BCECs (CTRL_8) and LS BCECs (ATP6_2), *n* = 1–5 independent experiments; two-way ANOVA.

(D) Quantification of sildenafil in the plasma of three LS patients treated with sildenafil.

(E) Exemplary cMRI taken during the diagnosis of the six LS patients who were subsequently treated with sildenafil. In patients 1–4 and 6, the arrows point towards T_2-hyperintense pathological basal ganglia lesions in the *Putamen* and *Globus pallidus* and in the *Nucleus caudatus* (patient 4); in patient 5, the arrow points towards frontal brain atrophy with an enlargement of the external cerebrospinal fluid spaces.

(F and G) NMDAS/NPMDS plotted as percentage of the maximum reachable score for the respective age group. Left: cohort in Newcastle (brown lines) and in Berlin (orange lines). Right: six LS patients treated with sildenafil.

(H–J) Different dimensions of NPMDS in untreated and sildenafil-treated LS patients.

See also Figure S12.

Table 1. Clinical characteristics and response to sildenafil treatment on an individual basis in six LS patients carrying *MT-ATP6* variants

Patient [sex assigned at birth]	Variant [mtDNA haplogroup] (heteroplasmy)	mtDNA variant on the protein level	Phenotype [manifestation age]	[HPO number] symptoms	cMRI features [at age in years]	Initiation of sildenafil treatment [years] (dosage)	Effect of sildenafil treatment
1 [male]	m.9176T>G [K1b2a3] (99.4%)	MT-ATP6 p.L217R	LEIGH [2 years]	[HPO:1250] epilepsy, [HPO:1260] dysarthria, [HPO:1270] motor developmental delay, [HPO:1639] cardiomyopathy, [HPO:2093] respiratory insufficiency, [HPO:3477] demyelinating neuropathy, [HPO:6789] encephlopathy, [HPO:7240] ataxia	increased T_2-signal intensities at the *Putamen*, *Nucleus caudatus* on both sides and at the perisylvian gray matter [16.5 years]	December 2018 ongoing [16 years] (2.0 mg/kg/day)	Improvements: independent breathing (tracheostoma could be closed), motor abilities (can sit, walk with support, maneuver wheel-chair), seizures stopped, independent eating and swallowing, cardiomyopathy improved; No change: neuropathy, dysarthria
2 [male]	m.8993T>G [U5a1b3] (87.7%)	MT-ATP6 p.L156R	LEIGH [2.5 years]	[HPO:1270] motor developmental delay, [HPO:2381] transient aphasia, [HPO:4911] metabolic crises, [HPO:7021] pain insensitivity, [HPO:7240] ataxia	increased T_2- and FLAIR-signal intensities at the *Putamen* and *Nucleus caudatus* on both sides [2.2 years]	October 2019 ongoing [15 years] (1.2 mg/kg/day)	Improvements: no metabolic crises during febrile illness, improvement of exercise tolerance (free walking distance improved from 500 to >5,000 m), no daytime sleepiness, ataxia improved, SARA score improved from 15.5 to 11 points; No change: mild intellectual disability
3 [female]	m.9185T>C [T2b] (100.0%)	MT-ATP6 p.L220P	LEIGH [5 years]	[HPO:0544] horizontal ophthalmoplegia, [HPO:1256] mild intellectual disability, [HPO:1270] motor developmental delay, [HPO:2355] loss of ambulation, [HPO:3477] axonal neuropathy, [HPO:3752] episodic muscle weakness	increased T_2-signal intensities at the *Putamen* on both sides [5 years], which had spontaneously disappeared by the age of 14 years	May 2019 until November 2021 [21 years] (2.9 mg/kg/day)	Improvements: reduction of episodes of muscle weakness, improvement of exercise intolerance**;** No change: neuropathy; Comments: after stopping sildenafil due to a delayed drug reaction (skin rash), the disease symptoms reappeared

(*Continued on next page*)

Table 1. ***Continued***

Patient [sex assigned at birth]	Variant [mtDNA haplogroup] (heteroplasmy)	mtDNA variant on the protein level	Phenotype [manifestation age]	[HPO number] symptoms	cMRI features [at age in years]	Initiation of sildenafil treatment [years] (dosage)	Effect of sildenafil treatment
4 [male]	m.8993T>G [R0a1a] (96.7%)	MT-ATP6 p.L156R	LEIGH [2–3 years]	[HPO:0365] deafness, [HPO:1249] intellectual developmental delay, [HPO:1270] motor developmental delay, [HPO:2123] myoclonic seizures, [HPO:2421] loss of head control, [HPO:3546] exercise intolerance, [HPO:7240] ataxia	increased FLAIR-signal intensities at the *Nuclei caudati* on both sides and enlargement of the internal and external CSF spaces due to diffuse brain atrophy [35 years]	May 2022 ongoing [38 years] (1.5 mg/kg/day)	Improvements: increased muscle strength (keeping his head position, ability to sit and walk), dysphagia, hyposthenia, slight improvement of in cognitive abilities; No change: deafness, ataxia; Comments: while the patient had to discontinue sildenafil for the time of an operation, the symptoms reoccurred after a short time and disappeared again after reinitiation of sildenafil
5 [male]	m.8570T>C[H4] (98.5%)	MT-ATP6 p.L15P, MT-ATP8 p.X68Q+26AS*	NARP [2 months]	[HPO:1639] hypertrophic cardiomyopathy, [HPO:1903] anemia, [HPO:2015] dysphagia, [HPO:4911] multiple metabolic crises, [HPO:8947] floppy infant	delayed myelination, frontal brain atrophy; increased T_2-signal intensities in the brain stem affecting the *Fasciculus longitudinalis* and the *Substantia nigra* on both sides [2.2 years]	September 2019 ongoing [9 months] (1.5 mg/kg/day)	Improvements: dysphagia, did not have a metabolic crisis after initiation of sildenafil therapy (before nearly one crisis every month with ICU admission), cardiomyopathy stable**;** No change: intellectual disability, delayed motor and cognitive development

(*Continued on next page*)

Table 1. *Continued*

Patient [sex assigned at birth]	Variant [mtDNA haplogroup] (heteroplasmy)	mtDNA variant on the protein level	Phenotype [manifestation age]	[HPO number] symptoms	cMRI features [at age in years]	Initiation of sildenafil treatment [years] (dosage)	Effect of sildenafil treatment
6 [female]	m.8993T>C [T2a1a] (100.0%)	MT-ATP6 p.L156R	LEIGH [7 years]	[HPO:1258] spastic paraplegia, [HPO:1268] intellectual decline, [HPO:1290] muscular hypotonia, [HPO:1332] dystonia, [HPO:2015] dysphagia, [HPO:2371] loss of speech, [HPO:2421] loss of head control, [HPO:4911] metabolic crisis, [HPO:6789] encephalopathy	increased T_2-signal intensities at the *Putamen*, *Pallidum*, and *Nucleus caudatus* on both sides and within the cortical gray matter [7.5 years]	June 2024 ongoing [7 years] (1.8 mg/kg/day)	Improvements: sitting with support and standing with assistance, consciousness normalized, normal language perception, slow improvement of muscle tone and movement disorder; No change: still wheelchair-dependent due to profound dystonia

NARP, neuropathy, ataxia, and retinitis pigmentosa; HPO, Human Phenotype Ontology; cMRI, cranial magnetic resonance imaging; FLAIR, fluid-attenuated inversion recovery; CSF, cerebrospinal fluid; SARA, scale for the assessment and rating of ataxia.See also Tables S3 and S4.

be applied to other neurological diseases for which effective model systems are lacking. Considering that mitochondria play a crucial role in cellular health and brain function and homeostasis,[117–119] understanding the potential effects of PDE5i in mitochondrial diseases may also have important implications in the context of common aging-related neurological disorders.

Limitations of the study

We reported clinical effects observed in a small cohort of mitochondrial disease patients. It is imperative that the safety and efficacy of sildenafil in patients with LS be assessed in a larger, double-blind, randomized, placebo-controlled trial. High sildenafil dosages were associated with toxicity in LS cardiomyocytes and microhemorrhages in newborn LS pigs. Although the doses that we used in LS patients have been found safe for neonatal encephalopathy,[120,121] particular precautions should be taken in infants due to the low sildenafil clearance in postnatal age that leads to longer half-lives in neonates compared with adults.[122] Sildenafil dosage should therefore be carefully monitored in treated children. Other more potent PDE5i, such as vardenafil (IC_{50} = 0.091 ± 0.031 nM) and tadalafil (IC_{50} = 1.8 ± 0.4 nM),[123] could be considered as alternatives to sildenafil in patients with mitochondrial disorders.[124]

The predictions of the mathematical model and the role of mitochondrial calcium fluxes, including the mitochondrial calcium uniporter and other ion channels that could be directly modified by cGMP or PRKG1, warrant further investigation to elucidate the effects of sildenafil in neural cells. We identified here putative sildenafil-responsive genes, but additional work is needed to dissect their biological role in LS. Besides experiments in pigs, which were carried out only in male animals, both sexes were investigated in all other experiments in mice and iPSCs, as well as in treatments on an individual basis. Nonetheless, we did not assess the influence of sex or gender on disease phenotypes and treatment outcomes. Future studies are required to address these aspects in the context of sildenafil treatment in mitochondrial diseases.

RESOURCE AVAILABILITY

Lead contact

Further information and requests for resources and reagents should be directed to and will be fulfilled by the lead contact, Alessandro Prigione (alessandro.prigione@hhu.de).

Information requests regarding Leigh syndrome patients and their treatment should be directed to the lead clinical scientist, Markus Schuelke (markus.schuelke@charite.de).

Materials availability

There are restrictions on the availability of patient-derived iPSCs used in this study due to our ethical approval, which does not support sharing with third parties without a specific amendment and does not allow performing genomic studies, in order to respect the European privacy protection law.

Data and code availability

- Raw and processed RNA-seq data are deposited in the NCBI Gene Expression Omnibus (GEO) or Sequence Read Archive (SRA): bulk RNA-seq NPC dataset at GEO: GSE292178; bulk RNA-seq brain organoids dataset at SRA BioProject: https://www.ncbi.nlm.nih.gov/bioproject/?term=PRJNA1248577; and snRNA-seq brain organoids dataset at GEO: GSE293573.

- The proteomics NPC dataset is deposited in the ProteomeXchange Consortium via the PRIDE partner repository[125] at PRIDE: PXD059519.
- The metabolomics NPC dataset is deposited in the MassIVE repository at MassIVE: https://www.omicsdi.org/dataset/massive/MSV000097182.
- Codes to reproduce our snRNA-seq results are available at: https://github.com/tpentim/Leigh_Sildenafil_Organoids.
- All original code is available in this paper's STAR Methods.
- Any additional information required to reanalyze the data reported in this paper is available from the lead contact upon request.

ACKNOWLEDGMENTS

We are grateful for technical support from Dr. Francesca Griggio, Samantha Solito, and Dr. Giulia Finotti (University of Verona); Leonardo Caporali (Carelli lab); Noemi Cannizzaro (Bottani lab); and Dr. Alessia Adelizzi, Dr. Chiara Guarona, and Dr. Martina Greco (Brunetti lab). We acknowledge financial support from the European Joint Programme for Rare Diseases (EJPRD) (CureMILS to A. Prigione, O.P., W.J.H.K., A.D.-S., P.L., E.B., A.S., and F.E.); the Bundesministerium für Forschung, Technologie und Raumfahrt (BMFTR) (01GM2002A to A. Prigione, 01GM2002B to O.P., mitoNET 01GM1906A and GENOMIT 01GM1920A to T.K., and the German Center for Child and Adolescent Health to M. Schuelke); the European Commission's Horizon Europe Programme (SIMPATHIC 101080249 to A. Prigione, M. Schuelke, and W.J.H.K.); the Deutsche Forschungsgemeinschaft (DFG) (PR1527/13-1, PR1527/14-1, and PR1527/15-1 to A. Prigione; RO5380/1-1 to A.R.; and FOR 2795 "Synapses under Stress" Ro2327/13-2 to C.R.R. and PR1527/6-1 to A. Prigione); AFM-Téléthon (SildeMITO 28545 to A. Prigione, M. Schuelke, V.C., V.T., and A.R.; 25179 to A.R.; and 29044 to A. Prigione); the German Excellence Strategy (EXC-2049-390688087) through the NeuroCure Consortium at Charité-Universitätsmedizin Berlin (to M. Schuelke); the SPARK program at the Berlin Institute of Health (BIH) (to A. Prigione and M. Schuelke); Telethon Italy (GMR23T2021 to I.S.); the Austrian Science Fund (FWF) (10.55776/I5184 and 10.55776/F78 to F.E.); the United Mitochondrial Disease Foundation (UMDF) and the Leigh Syndrome International Consortium (LSIC) (to A. Prigione and D.-F.D.); the foundations People Against Leigh Syndrome (PALS), Mito Foundation, Foundation Maladies Rares and Association (AMMi), Cure Mito and Cure ATP6, and Mitocon Italy (to A. Prigione); MitoHelp and the Eva Luise Köhler Foundation (to A. Prigione and M. Schuelke); KIAT 2410008128 and NIH DK133118 (to D.-F.D.); North Rhine-Westphalia and the European Union (IN-SU-3-001 to A.R.); the European Union (FETPROACT-2018-2020 HERMES 824164 to I.D.); the National Recovery and Resilience Plan (NRRP) (Mission 4, Component 2, Investment 1.1, Call for Tender No. 104 on February 2, 2022, by the Italian Ministry of University and Research, funded by the European Union – NextGeneration EU, project CUP B53D23018710001, Grant Assignment Decree no. 1110, adopted on July 20, 2023, by MUR) (to E.B.); Fondazione Telethon (GSA23F002 to E.B.; GMR23T2152 to D. Brunetti); the Italian Foundation A.M.Me.C. (to E.B.); Fondazione Regionale per la Ricerca Biomedica (Regione Lombardia-FRRB) (1740526 to D. Brunetti); the Italian Ministry of Health (RRC to D. Brunetti); RO5380/1-1, RO5380/10-1, and RO5380/13-1 (to A.R.); Leibniz Competition (SAW) Cooperative Excellence Project (K642/2024 to A.R.); and VHL Betroffene Familien e.V. (to A.R.). S.H. was supported by the Jürgen Manchot Stiftung. V.T., C.L.M., V.C., and M. Schuelke are members of the European Reference Network for Rare Neuromuscular Diseases (ERN EURO-NMD). Part of the work was performed at the Center for the Study of Mitochondrial Pediatric Diseases, funded by the Mariani Foundation, Italy, at Fondazione IRCCS Istituto Neurologico "Carlo Besta." During this study, A.S. was funded by the Research Council of Finland, the Jane and Aatos Erkko Foundation, the PolG Foundation, and the Sigrid Jusélius Foundation. We acknowledge the Center for Advanced Imaging (CAi) at HHU for providing access to the Revvity Operetta CLS. The graphical abstract was created with BioRender: https://BioRender.com/hi5ov9y.

AUTHOR CONTRIBUTIONS

Conceptualization, A. Prigione, M. Schuelke, O.P., D.-F.D., E.B., W.J.H.K., A.d.S., A.S., P.L., and F.E.; methodology, A. Zink, A.W., M.-T.H., G.P., S.H., C.J., L.P., M.S.C., J.B., C.B., L.E., A.D.D., F.S., D.M., A.R.-W., U.H., K.K., I.T., D. Brunetti, D. Bonesso, D.H., G.C., S.N.W., D.-F.D., C.M., L.S., T.K., M. Scaglia, J.K.-F., D.S., J.R., C.S., E.C., M.P.-G., S.M.-G., C.L.-M., F.D., I.D., F.D.S., A.A., R.D., M.B., M. Scaglia, C.G., L.A.N., and A. Perota; formal analysis, G.S., T.M.P., S.N., A.F., A.R.U., M. Schuelke, A. Zhaivoron, A. Zaliani, O.B., D.M., M.M., and A.M.; resources, E.M., V.C., V.T., A.R., N.R., P.L., B.K., I.D., and S.J.; writing – original draft, A. Prigione; writing – review & editing, A. Prigione, O.P., M. Schuelke, D.-F.D., E.B., and C.R.R.; supervision, A. Prigione, O.P., C.R.R., I.S., M.J.W.A.-H., E.M., S.J., G.U., S.P., W.J.H.K., A.S., F.E., E.B., M. Schuelke, L.C., V.C., S.J., A.d.S., and D. Brunetti; visualization, A. Zink, A.W., O.P., A. Prigione, M.-T.H., G.P., S.H., and M. Schuelke; funding acquisition, A. Prigione, D. Brunetti, A.d.S., O.P., W.J.H.K., P.L., A.S., F.E., E.B., M. Schuelke, and C.R.R.

DECLARATION OF INTERESTS

A. Prigione and M. Schuelke filed patent applications for sildenafil in the treatment of CIV and CV defects and obtained Orphan Drug Designation (ODD) for sildenafil in Leigh syndrome from the Committee for Orphan Medicinal Products (COMP) of the European Medicines Agency (EMA) (EU/3/23/2831). A.S. and L.E. are co-founders of NADMED Ltd.

STAR★METHODS

Detailed methods are provided in the online version of this paper and include the following:

- KEY RESOURCES TABLE
- EXPERIMENTAL MODEL AND STUDY PARTICIPANT DETAILS
  - Induced pluripotent stem cells (iPSCs)
  - Animals
  - Cell lines
  - Human participants
- METHOD DETAILS
  - Neural precursor cells (NPCs) and differentiated neurons
  - Cortical brain organoids
  - Assessment of mitochondrial membrane potential (MMP)
  - Compound screening
  - Bioenergetic assessment
  - Quantification of NAD metabolites
  - Quantification of mtDNA copy number
  - Analysis of mitochondrial nanostructure
  - Bulk RNA sequencing
  - Single-nucleus RNA sequencing
  - Proteomics analysis
  - Targeted metabolomics profiling
  - Multi-omics integration
  - Calcium imaging in cortical brain organoid slices (cBOS)
  - Calcium imaging in NPCs
  - Neurite outgrowth quantification
  - Experiments with *Ndufs4* KO mice
  - Experiments with *SURF1* KO pigs
  - Quantification of sildenafil concentration in patient plasma
  - Genotyping and heteroplasmy quantification
  - Cranial magnetic resonance imaging (cMRI)
  - Toxicity assays
  - Immunostaining
  - Immunoblot analysis
  - Mitochondrial complex assembly
  - Quantitative polymerase chain reaction (qPCR)
  - Human blood-brain barrier (BBB) model
  - iPSC-derived cardiomyocyte (iPSC-CMs)
  - Computational modeling of calcium and bioenergetics
- QUANTIFICATION AND STATISTICAL ANALYSIS

SUPPLEMENTAL INFORMATION

Supplemental information can be found online at https://doi.org/10.1016/j.cell.2026.02.008.

Received: April 14, 2025
Revised: August 19, 2025
Accepted: February 6, 2026
Published: March 11, 2026

REFERENCES

1. Gorman, G.S., Chinnery, P.F., DiMauro, S., Hirano, M., Koga, Y., McFarland, R., Suomalainen, A., Thorburn, D.R., Zeviani, M., and Turnbull, D.M. (2016). Mitochondrial diseases. Nat. Rev. Dis. Primers *2*, 16080. https://doi.org/10.1038/nrdp.2016.80.
2. Leigh, D. (1951). Subacute necrotizing encephalomyelopathy in an infant. J. Neurol. Neurosurg. Psychiatry *14*, 216–221. https://doi.org/10.1136/jnnp.14.3.216.
3. Baertling, F., Rodenburg, R.J., Schaper, J., Smeitink, J.A., Koopman, W.J.H., Mayatepek, E., Morava, E., and Distelmaier, F. (2014). A guide to diagnosis and treatment of Leigh syndrome. J. Neurol. Neurosurg. Psychiatry *85*, 257–265. https://doi.org/10.1136/jnnp-2012-304426.
4. McCormick, E.M., Keller, K., Taylor, J.P., Coffey, A.J., Shen, L., Krotoski, D., Harding, B., NICHD ClinGen U24 Mitochondrial Disease Gene Curation Expert Panel, Gai, X., Falk, M.J., et al. (2023). Expert Panel Curation of 113 Primary Mitochondrial Disease Genes for the Leigh Syndrome Spectrum. Ann. Neurol. *94*, 696–712. https://doi.org/10.1002/ana.26716.
5. Thorburn, D.R., Rahman, J., and Rahman, S. (1993). Mitochondrial DNA-Associated Leigh Syndrome and NARP. In GeneReviews®, M.P. Adam, D.B. Everman, G.M. Mirzaa, R.A. Pagon, S.E. Wallace, L.J.H. Bean, K.W. Gripp, and A. Amemiya, eds. (University of Washington).
6. Tiranti, V., Hoertnagel, K., Carrozzo, R., Galimberti, C., Munaro, M., Granatiero, M., Zelante, L., Gasparini, P., Marzella, R., Rocchi, M., et al. (1998). Mutations of SURF-1 in Leigh disease associated with cytochrome c oxidase deficiency. Am. J. Hum. Genet. *63*, 1609–1621. https://doi.org/10.1086/302150.
7. Petruzzella, V., Vergari, R., Puzziferri, I., Boffoli, D., Lamantea, E., Zeviani, M., and Papa, S. (2001). A nonsense mutation in the NDUFS4 gene encoding the 18 kDa (AQDQ) subunit of complex I abolishes assembly and activity of the complex in a patient with Leigh-like syndrome. Hum. Mol. Genet. *10*, 529–535. https://doi.org/10.1093/hmg/10.5.529.
8. Weissig, V. (2020). Drug Development for the Therapy of Mitochondrial Diseases. Trends Mol. Med. *26*, 40–57. https://doi.org/10.1016/j.molmed.2019.09.002.
9. Henke, M.T., Prigione, A., and Schuelke, M. (2024). Disease models of Leigh syndrome: From yeast to organoids. J. Inherit. Metab. Dis. *47*, 1292–1321. https://doi.org/10.1002/jimd.12804.
10. Gammage, P.A., Moraes, C.T., and Minczuk, M. (2018). Mitochondrial Genome Engineering: The Revolution May Not Be CRISPR-Ized. Trends Genet. *34*, 101–110. https://doi.org/10.1016/j.tig.2017.11.001.
11. Quadalti, C., Brunetti, D., Lagutina, I., Duchi, R., Perota, A., Lazzari, G., Cerutti, R., Di Meo, I., Johnson, M., Bottani, E., et al. (2018). SURF1 knockout cloned pigs: Early onset of a severe lethal phenotype. Biochim. Biophys. Acta Mol. Basis Dis. *1864*, 2131–2142. https://doi.org/10.1016/j.bbadis.2018.03.021.
12. Dell'agnello, C., Leo, S., Agostino, A., Szabadkai, G., Tiveron, C., Zulian, A., Prelle, A., Roubertoux, P., Rizzuto, R., and Zeviani, M. (2007). Increased longevity and refractoriness to Ca(2+)-dependent neurodegeneration in Surf1 knockout mice. Hum. Mol. Genet. *16*, 431–444. https://doi.org/10.1093/hmg/ddl477.
13. Kovářová, N., Pecina, P., Nůsková, H., Vrbacký, M., Zeviani, M., Mráček, T., Viscomi, C., and Houštěk, J. (2016). Tissue- and species-specific differences in cytochrome c oxidase assembly induced by SURF1 defects. Biochim. Biophys. Acta *1862*, 705–715. https://doi.org/10.1016/j.bbadis.2016.01.007.
14. Quintana, A., Kruse, S.E., Kapur, R.P., Sanz, E., and Palmiter, R.D. (2010). Complex I deficiency due to loss of Ndufs4 in the brain results in progressive encephalopathy resembling Leigh syndrome. Proc. Natl. Acad. Sci. USA *107*, 10996–11001. https://doi.org/10.1073/pnas.1006214107.
15. van de Wal, M.A.E., Adjobo-Hermans, M.J.W., Keijer, J., Schirris, T.J.J., Homberg, J.R., Wieckowski, M.R., Grefte, S., van Schothorst, E.M., van Karnebeek, C., Quintana, A., et al. (2022). Ndufs4 knockout mouse models of Leigh syndrome: pathophysiology and intervention. Brain *145*, 45–63. https://doi.org/10.1093/brain/awab426.
16. Martinelli, D., Catteruccia, M., Piemonte, F., Pastore, A., Tozzi, G., Dionisi-Vici, C., Pontrelli, G., Corsetti, T., Livadiotti, S., Kheifets, V., et al. (2012). EPI-743 reverses the progression of the pediatric mitochondrial disease–genetically defined Leigh Syndrome. Mol. Genet. Metab. *107*, 383–388. https://doi.org/10.1016/j.ymgme.2012.09.007.
17. Kayser, E.B., Mulholland, M., Olkhova, E.A., Chen, Y., Coulson, H., Cairns, O., Truong, V., James, K., Johnson, B.M., Hanaford, A., et al. (2025). Evaluating the efficacy of vatiquinone in preclinical models of Leigh syndrome and GPX4 deficiency. Orphanet J. Rare Dis. *20*, 65. https://doi.org/10.1186/s13023-025-03582-x.
18. de Haas, R., Das, D., Garanto, A., Renkema, H.G., Greupink, R., van den Broek, P., Pertijs, J., Collin, R.W.J., Willems, P., Beyrath, J., et al. (2017). Therapeutic effects of the mitochondrial ROS-redox modulator KH176 in a mammalian model of Leigh Disease. Sci. Rep. *7*, 11733. https://doi.org/10.1038/s41598-017-09417-5.
19. Johnson, S.C., Yanos, M.E., Kayser, E.B., Quintana, A., Sangesland, M., Castanza, A., Uhde, L., Hui, J., Wall, V.Z., Gagnidze, A., et al. (2013). mTOR inhibition alleviates mitochondrial disease in a mouse model of Leigh syndrome. Science *342*, 1524–1528. https://doi.org/10.1126/science.1244360.
20. Hanaford, A.R., Khanna, A., James, K., Truong, V., Liao, R., Chen, Y., Mulholland, M., Kayser, E.B., Watanabe, K., Hsieh, E.S., et al. (2024). Interferon-gamma contributes to disease progression in the Ndufs4(-/-) model of Leigh syndrome. Neuropathol. Appl. Neurobiol. *50*, e12977. https://doi.org/10.1111/nan.12977.
21. Puighermanal, E., Luna-Sánchez, M., Gella, A., van der Walt, G., Urpi, A., Royo, M., Tena-Morraja, P., Appiah, I., de Donato, M.H., Menardy, F., et al. (2024). Cannabidiol ameliorates mitochondrial disease via PPARgamma activation in preclinical models. Nat. Commun. *15*, 7730. https://doi.org/10.1038/s41467-024-51884-8.
22. Jain, I.H., Zazzeron, L., Goli, R., Alexa, K., Schatzman-Bone, S., Dhillon, H., Goldberger, O., Peng, J., Shalem, O., Sanjana, N.E., et al. (2016). Hypoxia as a therapy for mitochondrial disease. Science *352*, 54–61. https://doi.org/10.1126/science.aad9642.
23. Blume, S.Y., Garg, A., Martí-Mateos, Y., Midha, A.D., Chew, B.T.L., Lin, B., Yu, C., Dick, R., Lee, P.S., Situ, E., et al. (2025). HypoxyStat, a small-molecule form of hypoxia therapy that increases oxygen-hemoglobin affinity. Cell *188*, 1580–1588.e11. https://doi.org/10.1016/j.cell.2025.01.029.
24. Tolle, I., Tiranti, V., and Prigione, A. (2023). Modeling mitochondrial DNA diseases: from base editing to pluripotent stem-cell-derived organoids. EMBO Rep. *24*, e55678. https://doi.org/10.15252/embr.202255678.
25. Inak, G., Rybak-Wolf, A., Lisowski, P., Pentimalli, T.M., Jüttner, R., Glažar, P., Uppal, K., Bottani, E., Brunetti, D., Secker, C., et al. (2021). Defective metabolic programming impairs early neuronal morphogenesis in neural cultures and an organoid model of Leigh syndrome. Nat. Commun. *12*, 1929. https://doi.org/10.1038/s41467-021-22117-z.
26. Galera-Monge, T., Zurita-Díaz, F., Canals, I., Hansen, M.G., Rufián-Vázquez, L., Ehinger, J.K., Elmér, E., Martin, M.A., Garesse, R., Ahlenius, H., et al. (2020). Mitochondrial Dysfunction and Calcium Dysregulation in Leigh Syndrome Induced Pluripotent Stem Cell Derived Neurons. Int. J. Mol. Sci. *21*, 3191. https://doi.org/10.3390/ijms21093191.
27. Lorenz, C., Lesimple, P., Bukowiecki, R., Zink, A., Inak, G., Mlody, B., Singh, M., Semtner, M., Mah, N., Auré, K., et al. (2017). Human iPSC-Derived Neural Progenitors Are an Effective Drug Discovery Model for Neurological mtDNA Disorders. Cell Stem Cell *20*, 659–674.e9. https://doi.org/10.1016/j.stem.2016.12.013.

28. Zheng, X., Boyer, L., Jin, M., Kim, Y., Fan, W., Bardy, C., Berggren, T., Evans, R.M., Gage, F.H., and Hunter, T. (2016). Alleviation of neuronal energy deficiency by mTOR inhibition as a treatment for mitochondria-related neurodegeneration. eLife *5*, e13378. https://doi.org/10.7554/eLife.13378.

29. Romero-Morales, A.I., Robertson, G.L., Rastogi, A., Rasmussen, M.L., Temuri, H., McElroy, G.S., Chakrabarty, R.P., Hsu, L., Almonacid, P.M., Millis, B.A., et al. (2022). Human iPSC-derived cerebral organoids model features of Leigh syndrome and reveal abnormal corticogenesis. Development *149*, dev199914. https://doi.org/10.1242/dev.199914.

30. Menacho, C., Okawa, S., Álvarez-Merz, I., Wittich, A., Muñoz-Oreja, M., Lisowski, P., Pentimalli, T.M., Rybak-Wolf, A., Inak, G., Zakin, S., et al. (2024). Deep learning-driven neuromorphogenesis screenings identify repurposable drugs for mitochondrial disease. Preprint at bioRxiv. https://doi.org/10.1101/2024.07.08.602501.

31. Zink, A., Haferkamp, U., Wittich, A., Beller, M., Pless, O., and Prigione, A. (2022). High-content screening of mitochondrial polarization in neural cells derived from human pluripotent stem cells. Star Protoc. *3*, 101602. https://doi.org/10.1016/j.xpro.2022.101602.

32. Ghofrani, H.A., Osterloh, I.H., and Grimminger, F. (2006). Sildenafil: from angina to erectile dysfunction to pulmonary hypertension and beyond. Nat. Rev. Drug Discov. *5*, 689–702. https://doi.org/10.1038/nrd2030.

33. Henke, M.T., Zink, A., Diecke, S., Prigione, A., and Schuelke, M. (2023). Generation of two mother-child pairs of iPSCs from maternally inherited Leigh syndrome patients with m.8993 T > G and m.9176 T > G MT-ATP6 mutations. Stem Cell Res. *67*, 103030. https://doi.org/10.1016/j.scr.2023.103030.

34. Lorenz, C., Zink, A., Henke, M.T., Staege, S., Mlody, B., Bünning, M., Wanker, E., Diecke, S., Schuelke, M., and Prigione, A. (2022). Generation of four iPSC lines from four patients with Leigh syndrome carrying homoplasmic mutations m.8993T > G or m.8993T > C in the mitochondrial gene MT-ATP6. Stem Cell Res. *61*, 102742. https://doi.org/10.1016/j.scr.2022.102742.

35. Steiner, T., Zink, A., Henke, M.T., Cecchetto, G., Buenning, M., Rossi, A., Schuelke, M., and Prigione, A. (2022). RNA-based generation of iPSCs from a boy carrying the mutation m.9185 T>C in the mitochondrial gene MT-ATP6 and from his healthy mother. Stem Cell Res. *64*, 102920. https://doi.org/10.1016/j.scr.2022.102920.

36. Haschke, A.M., Diecke, S., and Schuelke, M. (2024). Characterization of two iPSC lines from patients with maternally inherited leigh (MILS) and neuropathy, ataxia, and retinitis pigmentosa (NARP) syndrome carrying the MT-ATP6 m.8993 T>G mutation at different degrees of heteroplasmy. Stem Cell Res. *81*, 103547. https://doi.org/10.1016/j.scr.2024.103547.

37. Corsello, S.M., Bittker, J.A., Liu, Z., Gould, J., McCarren, P., Hirschman, J.E., Johnston, S.E., Vrcic, A., Wong, B., Khan, M., et al. (2017). The Drug Repurposing Hub: a next-generation drug library and information resource. Nat. Med. *23*, 405–408. https://doi.org/10.1038/nm.4306.

38. Zhang, J.H., Chung, T.D., and Oldenburg, K.R. (1999). A Simple Statistical Parameter for Use in Evaluation and Validation of High Throughput Screening Assays. J. Biomol. Screen. *4*, 67–73. https://doi.org/10.1177/108705719900400206.

39. Sun, L., Wang, C., Zhou, Y., Sun, W., and Wang, C. (2021). Clinical Efficacy and Safety of Different Doses of Sildenafil in the Treatment of Persistent Pulmonary Hypertension of the Newborn: A Network Meta-analysis. Front. Pharmacol. *12*, 697287. https://doi.org/10.3389/fphar.2021.697287.

40. Barst, R.J., Beghetti, M., Pulido, T., Layton, G., Konourina, I., Zhang, M., and Ivy, D.D.; STARTS-2 Investigators (2014). STARTS-2: long-term survival with oral sildenafil monotherapy in treatment-naive pediatric pulmonary arterial hypertension. Circulation *129*, 1914–1923. https://doi.org/10.1161/CIRCULATIONAHA.113.005698.

41. Barst, R.J., Ivy, D.D., Gaitan, G., Szatmari, A., Rudzinski, A., Garcia, A.E., Sastry, B.K., Pulido, T., Layton, G.R., Serdarevic-Pehar, M., et al. (2012). A randomized, double-blind, placebo-controlled, dose-ranging study of oral sildenafil citrate in treatment-naive children with pulmonary arterial hypertension. Circulation *125*, 324–334. https://doi.org/10.1161/CIRCULATIONAHA.110.016667.

42. Danial, C., Tichy, A.L., Tariq, U., Swetman, G.L., Khuu, P., Leung, T.H., Benjamin, L., Teng, J., Vasanawala, S.S., and Lane, A.T. (2014). An open-label study to evaluate sildenafil for the treatment of lymphatic malformations. J. Am. Acad. Dermatol. *70*, 1050–1057. https://doi.org/10.1016/j.jaad.2014.02.005.

43. Bugiardini, E., Bottani, E., Marchet, S., Poole, O.V., Beninca, C., Horga, A., Woodward, C., Lam, A., Hargreaves, I., Chalasani, A., et al. (2020). Expanding the molecular and phenotypic spectrum of truncating MT-ATP6 mutations. Neurol. Genet. *6*, e381. https://doi.org/10.1212/NXG.0000000000000381.

44. Carrozzo, R., Wittig, I., Santorelli, F.M., Bertini, E., Hofmann, S., Brandt, U., and Schägger, H. (2006). Subcomplexes of human ATP synthase mark mitochondrial biosynthesis disorders. Ann. Neurol. *59*, 265–275. https://doi.org/10.1002/ana.20729.

45. Kenvin, S., Torregrosa-Muñumer, R., Reidelbach, M., Pennonen, J., Turkia, J.J., Rannila, E., Kvist, J., Sainio, M.T., Huber, N., Herukka, S.K., et al. (2022). Threshold of heteroplasmic truncating MT-ATP6 mutation in reprogramming, Notch hyperactivation and motor neuron metabolism. Hum. Mol. Genet. *31*, 958–974. https://doi.org/10.1093/hmg/ddab299.

46. Stephan, T., Brüser, C., Deckers, M., Steyer, A.M., Balzarotti, F., Barbot, M., Behr, T.S., Heim, G., Hübner, W., Ilgen, P., et al. (2020). MICOS assembly controls mitochondrial inner membrane remodeling and crista junction redistribution to mediate cristae formation. EMBO J. *39*, e104105. https://doi.org/10.15252/embj.2019104105.

47. Li, C., Enomoto, M., Rossi, A.M., Seo, M.D., Rahman, T., Stathopulos, P.B., Taylor, C.W., Ikura, M., and Ames, J.B. (2013). CaBP1, a neuronal Ca2+ sensor protein, inhibits inositol trisphosphate receptors by clamping intersubunit interactions. Proc. Natl. Acad. Sci. USA *110*, 8507–8512. https://doi.org/10.1073/pnas.1220847110.

48. Jeannotte, L., Gotti, F., and Landry-Truchon, K. (2016). Hoxa5: A Key Player in Development and Disease. J. Dev. Biol. *4*, 13. https://doi.org/10.3390/jdb4020013.

49. Philippidou, P., Walsh, C.M., Aubin, J., Jeannotte, L., and Dasen, J.S. (2012). Sustained Hox5 gene activity is required for respiratory motor neuron development. Nat. Neurosci. *15*, 1636–1644. https://doi.org/10.1038/nn.3242.

50. Inamata, Y., and Shirasaki, R. (2014). Dbx1 triggers crucial molecular programs required for midline crossing by midbrain commissural axons. Development *141*, 1260–1271. https://doi.org/10.1242/dev.102327.

51. Eichholtz-Wirth, H., Fritz, E., and Wolz, L. (2003). Overexpression of the ‘silencer of death domain’, SODD/BAG-4, modulates both TNFR1- and CD95-dependent cell death pathways. Cancer Lett. *194*, 81–89. https://doi.org/10.1016/s0304-3835(03)00009-0.

52. Kreider, R.B., and Stout, J.R. (2021). Creatine in Health and Disease. Nutrients *13*, 447. https://doi.org/10.3390/nu13020447.

53. Wyss, M., and Kaddurah-Daouk, R. (2000). Creatine and creatinine metabolism. Physiol. Rev. *80*, 1107–1213. https://doi.org/10.1152/physrev.2000.80.3.1107.

54. Paul, B.D., Sbodio, J.I., and Snyder, S.H. (2018). Cysteine Metabolism in Neuronal Redox Homeostasis. Trends Pharmacol. Sci. *39*, 513–524. https://doi.org/10.1016/j.tips.2018.02.007.

55. Lisowski, P., Lickfett, S., Rybak-Wolf, A., Menacho, C., Le, S., Pentimalli, T.M., Notopoulou, S., Dykstra, W., Oehler, D., López-Calcerrada, S., et al. (2024). Mutant huntingtin impairs neurodevelopment in human brain organoids through CHCHD2-mediated neurometabolic failure. Nat. Commun. *15*, 7027. https://doi.org/10.1038/s41467-024-51216-w.

56. Francis, S.H., Busch, J.L., Corbin, J.D., and Sibley, D. (2010). cGMP-dependent protein kinases and cGMP phosphodiesterases in nitric oxide and cGMP action. Pharmacol. Rev. *62*, 525–563. https://doi.org/10.1124/pr.110.002907.

57. Andrieu, G., Tran, A.H., Strissel, K.J., and Denis, G.V. (2016). BRD4 Regulates Breast Cancer Dissemination through Jagged1/Notch1 Signaling. Cancer Res. *76*, 6555–6567. https://doi.org/10.1158/0008-5472.CAN-16-0559.

58. Xu, F., Lu, S., Jia, X., and Zhou, Y. (2023). Bromodomain protein 4 mediates the roles of TGFβ1-induced Stat3 signaling in mouse liver fibrogenesis. Toxicol. Lett. *385*, 42–50. https://doi.org/10.1016/j.toxlet.2023.08.009.

59. Shi, L., and Bergson, C.M. (2020). Neuregulin 1: an intriguing therapeutic target for neurodevelopmental disorders. Transl. Psychiatry *10*, 190. https://doi.org/10.1038/s41398-020-00868-5.

60. Sophocleous, R.A., Ooi, L., and Sluyter, R. (2022). The P2X4 Receptor: Cellular and Molecular Characteristics of a Promising Neuroinflammatory Target. Int. J. Mol. Sci. *23*, 5739. https://doi.org/10.3390/ijms23105739.

61. Chou, J.Y., and Mansfield, B.C. (2014). The SLC37 family of sugar-phosphate/phosphate exchangers. Curr. Top. Membr. *73*, 357–382. https://doi.org/10.1016/B978-0-12-800223-0.00010-4.

62. Le, S., Petersilie, L., Inak, G., Menacho-Pando, C., Kafitz, K.W., Rybak-Wolf, A., Rajewsky, N., Rose, C.R., and Prigione, A. (2021). Generation of Human Brain Organoids for Mitochondrial Disease Modeling. J. Vis. Exp. *172*, e62756. https://doi.org/10.3791/62756.

63. Miura, Y., Li, M.Y., Birey, F., Ikeda, K., Revah, O., Thete, M.V., Park, J.Y., Puno, A., Lee, S.H., Porteus, M.H., et al. (2020). Generation of human striatal organoids and cortico-striatal assembloids from human pluripotent stem cells. Nat. Biotechnol. *38*, 1421–1430. https://doi.org/10.1038/s41587-020-00763-w.

64. Cong, Y., So, V., Tijssen, M.A.J., Verbeek, D.S., Reggiori, F., and Mauthe, M. (2021). WDR45, one gene associated with multiple neurodevelopmental disorders. Autophagy *17*, 3908–3923. https://doi.org/10.1080/15548627.2021.1899669.

65. Craig, A.M., and Kang, Y. (2007). Neurexin-neuroligin signaling in synapse development. Curr. Opin. Neurobiol. *17*, 43–52. https://doi.org/10.1016/j.conb.2007.01.011.

66. Klim, J.R., Williams, L.A., Limone, F., Guerra San Juan, I., Davis-Dusenbery, B.N., Mordes, D.A., Burberry, A., Steinbaugh, M.J., Gamage, K.K., Kirchner, R., et al. (2019). ALS-implicated protein TDP-43 sustains levels of STMN2, a mediator of motor neuron growth and repair. Nat. Neurosci. *22*, 167–179. https://doi.org/10.1038/s41593-018-0300-4.

67. Liu, Z., Chatterjee, T.K., and Fisher, R.A. (2002). RGS6 interacts with SCG10 and promotes neuronal differentiation. Role of the G gamma subunit-like (GGL) domain of RGS6. J. Biol. Chem. *277*, 37832–37839. https://doi.org/10.1074/jbc.M205908200.

68. He, Z., Dony, L., Fleck, J.S., Szałata, A., Li, K.X., Slišković, I., Lin, H.C., Santel, M., Atamian, A., Quadrato, G., et al. (2024). An integrated transcriptomic cell atlas of human neural organoids. Nature *635*, 690–698. https://doi.org/10.1038/s41586-024-08172-8.

69. Petersilie, L., Heiduschka, S., Nelson, J.S.E., Neu, L.A., Le, S., Anand, R., Kafitz, K.W., Prigione, A., and Rose, C.R. (2024). Cortical brain organoid slices (cBOS) for the study of human neural cells in minimal networks. iScience *27*, 109415. https://doi.org/10.1016/j.isci.2024.109415.

70. Wacquier, B., Combettes, L., Van Nhieu, G.T., and Dupont, G. (2016). Interplay Between Intracellular Ca(2+) Oscillations and Ca(2+)-stimulated Mitochondrial Metabolism. Sci. Rep. *6*, 19316. https://doi.org/10.1038/srep19316.

71. Toglia, P., Cheung, K.H., Mak, D.O.D., and Ullah, G. (2016). Impaired mitochondrial function due to familial Alzheimer's disease-causing presenilins mutants via Ca(2+) disruptions. Cell Calcium *59*, 240–250. https://doi.org/10.1016/j.ceca.2016.02.013.

72. Toglia, P., and Ullah, G. (2016). The gain-of-function enhancement of IP3-receptor channel gating by familial Alzheimer's disease-linked presenilin mutants increases the open probability of mitochondrial permeability transition pore. Cell Calcium *60*, 13–24. https://doi.org/10.1016/j.ceca.2016.05.002.

73. Pensalfini, A., Umar, A.R., Glabe, C., Parker, I., Ullah, G., and Demuro, A. (2022). Intracellular Injection of Brain Extracts from Alzheimer's Disease Patients Triggers Unregulated Ca^{2+} Release from Intracellular Stores That Hinders Cellular Bioenergetics. Cells *11*, 3630. https://doi.org/10.3390/cells11223630.

74. D'Angelo, D., Sánchez-Vázquez, V.H., Cartes-Saavedra, B., Vecellio Reane, D., Cupo, R.R., Delgado de la Herran, H., Ghirardo, G., Shorter, J., Wevers, R.A., Wortmann, S.B., et al. (2025). Dependence of mitochondrial calcium signalling and dynamics on the disaggregase, CLPB. Nat. Commun. *16*, 2810. https://doi.org/10.1038/s41467-025-57641-9.

75. Waldeck-Weiermair, M., Deak, A.T., Groschner, L.N., Alam, M.R., Jean-Quartier, C., Malli, R., and Graier, W.F. (2013). Molecularly distinct routes of mitochondrial Ca2+ uptake are activated depending on the activity of the sarco/endoplasmic reticulum Ca2+ ATPase (SERCA). J. Biol. Chem. *288*, 15367–15379. https://doi.org/10.1074/jbc.M113.462259.

76. Szabo, I., and Szewczyk, A. (2023). Mitochondrial Ion Channels. Annu. Rev. Biophys. *52*, 229–254. https://doi.org/10.1146/annurev-biophys-092622-094853.

77. Behmenburg, F., Dorsch, M., Huhn, R., Mally, D., Heinen, A., Hollmann, M.W., and Berger, M.M. (2015). Impact of Mitochondrial Ca2+-Sensitive Potassium (mBKCa) Channels in Sildenafil-Induced Cardioprotection in Rats. PLoS One *10*, e0144737. https://doi.org/10.1371/journal.pone.0144737.

78. Prieto, D., Rivera, L., Benedito, S., Recio, P., Villalba, N., Hernández, M., and García-Sacristán, A. (2006). Ca2+-activated K+ (KCa) channels are involved in the relaxations elicited by sildenafil in penile resistance arteries. Eur. J. Pharmacol. *531*, 232–237. https://doi.org/10.1016/j.ejphar.2005.12.033.

79. Checchetto, V., Leanza, L., De Stefani, D., Rizzuto, R., Gulbins, E., and Szabo, I. (2021). Mitochondrial K^+ channels and their implications for disease mechanisms. Pharmacol. Ther. *227*, 107874. https://doi.org/10.1016/j.pharmthera.2021.107874.

80. Kulawiak, B., Żochowska, M., Bednarczyk, P., Galuba, A., Stroud, D.A., and Szewczyk, A. (2023). Loss of the large conductance calcium-activated potassium channel causes an increase in mitochondrial reactive oxygen species in glioblastoma cells. Pflugers Arch. *475*, 1045–1060. https://doi.org/10.1007/s00424-023-02833-9.

81. Lickfett, S., Menacho, C., Zink, A., Telugu, N.S., Beller, M., Diecke, S., Cambridge, S., and Prigione, A. (2022). High-content analysis of neuronal morphology in human iPSC-derived neurons. Star Protoc. *3*, 101567. https://doi.org/10.1016/j.xpro.2022.101567.

82. Shelly, M., Lim, B.K., Cancedda, L., Heilshorn, S.C., Gao, H., and Poo, M.M. (2010). Local and long-range reciprocal regulation of cAMP and cGMP in axon/dendrite formation. Science *327*, 547–552. https://doi.org/10.1126/science.1179735.

83. Zhao, Z., Wang, Z., Gu, Y., Feil, R., Hofmann, F., and Ma, L. (2009). Regulate axon branching by the cyclic GMP pathway via inhibition of glycogen synthase kinase 3 in dorsal root ganglion sensory neurons. J. Neurosci. *29*, 1350–1360. https://doi.org/10.1523/JNEUROSCI.3770-08.2009.

84. Fiscus, R.R. (2002). Involvement of cyclic GMP and protein kinase G in the regulation of apoptosis and survival in neural cells. Neurosignals. *11*, 175–190. https://doi.org/10.1159/000065431.

85. Barnstable, C.J., Wei, J.Y., and Han, M.H. (2004). Modulation of synaptic function by cGMP and cGMP-gated cation channels. Neurochem. Int. *45*, 875–884. https://doi.org/10.1016/j.neuint.2004.03.018.

86. Schmidt, H., Werner, M., Heppenstall, P.A., Henning, M., Moré, M.I., Kühbandner, S., Lewin, G.R., Hofmann, F., Feil, R., and Rathjen, F.G. (2002). cGMP-mediated signaling via cGKIalpha is required for the guidance and connectivity of sensory axons. J. Cell Biol. *159*, 489–498. https://doi.org/10.1083/jcb.200207058.

87. Yoon, J.Y., Daneshgar, N., Chu, Y., Chen, B., Hefti, M., Vikram, A., Irani, K., Song, L.S., Brenner, C., Abel, E.D., et al. (2022). Metabolic rescue ameliorates mitochondrial encephalo-cardiomyopathy in murine and

human iPSC models of Leigh syndrome. Clin. Transl. Med. *12*, e954. https://doi.org/10.1002/ctm2.954.

88. Aguilar, K., Comes, G., Canal, C., Quintana, A., Sanz, E., and Hidalgo, J. (2022). Microglial response promotes neurodegeneration in the Ndufs4 KO mouse model of Leigh syndrome. Glia *70*, 2032–2044. https://doi.org/10.1002/glia.24234.
89. Daneshgar, N., Leidinger, M.R., Le, S., Hefti, M., Prigione, A., and Dai, D.F. (2022). Activated microglia and neuroinflammation as a pathogenic mechanism in Leigh syndrome. Front. Neurosci. *16*, 1068498. https://doi.org/10.3389/fnins.2022.1068498.
90. Appelt-Menzel, A., Oerter, S., Mathew, S., Haferkamp, U., Hartmann, C., Jung, M., Neuhaus, W., and Pless, O. (2020). Human iPSC-Derived Blood-Brain Barrier Models: Valuable Tools for Preclinical Drug Discovery and Development? Curr. Protoc. Stem Cell Biol. *55*, e122. https://doi.org/10.1002/cpsc.122.
91. Gómez-Vallejo, V., Ugarte, A., García-Barroso, C., Cuadrado-Tejedor, M., Szczupak, B., Dopeso-Reyes, I.G., Lanciego, J.L., García-Osta, A., Llop, J., Oyarzabal, J., et al. (2016). Pharmacokinetic investigation of sildenafil using positron emission tomography and determination of its effect on cerebrospinal fluid cGMP levels. J. Neurochem. *136*, 403–415. https://doi.org/10.1111/jnc.13454.
92. Phoenix, C., Schaefer, A.M., Elson, J.L., Morava, E., Bugiani, M., Uziel, G., Smeitink, J.A., Turnbull, D.M., and McFarland, R. (2006). A scale to monitor progression and treatment of mitochondrial disease in children. Neuromuscul. Disord. *16*, 814–820. https://doi.org/10.1016/j.nmd.2006.08.006.
93. Schaefer, A.M., Phoenix, C., Elson, J.L., McFarland, R., Chinnery, P.F., and Turnbull, D.M. (2006). Mitochondrial disease in adults: a scale to monitor progression and treatment. Neurology *66*, 1932–1934. https://doi.org/10.1212/01.wnl.0000219759.72195.41.
94. Lim, A.Z., Ng, Y.S., Blain, A., Jiminez-Moreno, C., Alston, C.L., Nesbitt, V., Simmons, L., Santra, S., Wassmer, E., Blakely, E.L., et al. (2022). Natural History of Leigh Syndrome: A Study of Disease Burden and Progression. Ann. Neurol. *91*, 117–130. https://doi.org/10.1002/ana.26260.
95. Carli, S., Levarlet, A., Diodato, D., Bertini, E.S., Martinelli, D., Malandrini, A., Lopergolo, D., Gallus, G.N., Ganetzky, R.D., La Morgia, C., et al. (2025). Natural History of Patients With Mitochondrial ATPase Deficiency Due to Pathogenic Variants of MT-ATP6 and MT-ATP8. Neurology *104*, e213462. https://doi.org/10.1212/WNL.0000000000213462.
96. Giuliano, F., Jackson, G., Montorsi, F., Martin-Morales, A., and Raillard, P. (2010). Safety of sildenafil citrate: review of 67 double-blind placebo-controlled trials and the postmarketing safety database. Int. J. Clin. Pract. *64*, 240–255. https://doi.org/10.1111/j.1742-1241.2009.02254.x.
97. Xiong, Y., and Wintermark, P. (2022). The Role of Sildenafil in Treating Brain Injuries in Adults and Neonates. Front. Cell. Neurosci. *16*, 879649. https://doi.org/10.3389/fncel.2022.879649.
98. Fang, J., Zhang, P., Zhou, Y., Chiang, C.W., Tan, J., Hou, Y., Stauffer, S., Li, L., Pieper, A.A., Cummings, J., et al. (2021). Endophenotype-based in silico network medicine discovery combined with insurance record data mining identifies sildenafil as a candidate drug for Alzheimer's disease. Nat Aging *1*, 1175–1188. https://doi.org/10.1038/s43587-021-00138-z.
99. Sanders, O., and Rajagopal, L. (2020). Phosphodiesterase Inhibitors for Alzheimer's Disease: A Systematic Review of Clinical Trials and Epidemiology with a Mechanistic Rationale. J. Alzheimers. Dis. Rep. *4*, 185–215. https://doi.org/10.3233/ADR-200191.
100. Saavedra, A., Giralt, A., Arumí, H., Alberch, J., and Pérez-Navarro, E. (2013). Regulation of hippocampal cGMP levels as a candidate to treat cognitive deficits in Huntington's disease. PLoS One *8*, e73664. https://doi.org/10.1371/journal.pone.0073664.
101. Puerta, E., Hervias, I., Barros-Miñones, L., Jordan, J., Ricobaraza, A., Cuadrado-Tejedor, M., García-Osta, A., and Aguirre, N. (2010). Sildenafil protects against 3-nitropropionic acid neurotoxicity through the modulation of calpain, CREB, and BDNF. Neurobiol. Dis. *38*, 237–245. https://doi.org/10.1016/j.nbd.2010.01.013.
102. Achenbach, J., Faissner, S., and Saft, C. (2022). Resurrection of sildenafil: potential for Huntington's Disease, too? J. Neurol. *269*, 5144–5150. https://doi.org/10.1007/s00415-022-11196-7.
103. Duarte-Silva, E., Meiry da Rocha Araújo, S., Oliveira, W.H., Lós, D.B., Bonfanti, A.P., Peron, G., de Lima Thomaz, L., Verinaud, L., and Peixoto, C.A. (2021). Sildenafil Alleviates Murine Experimental Autoimmune Encephalomyelitis by Triggering Autophagy in the Spinal Cord. Front. Immunol. *12*, 671511. https://doi.org/10.3389/fimmu.2021.671511.
104. Ölmestig, J.N.E., Marlet, I.R., Hainsworth, A.H., and Kruuse, C. (2017). Phosphodiesterase 5 inhibition as a therapeutic target for ischemic stroke: A systematic review of preclinical studies. Cell. Signal. *38*, 39–48. https://doi.org/10.1016/j.cellsig.2017.06.015.
105. Zhang, R.L., Chopp, M., Roberts, C., Wei, M., Wang, X., Liu, X., Lu, M., and Zhang, Z.G. (2012). Sildenafil enhances neurogenesis and oligodendrogenesis in ischemic brain of middle-aged mouse. PLoS One *7*, e48141. https://doi.org/10.1371/journal.pone.0048141.
106. Feil, R., Hofmann, F., and Kleppisch, T. (2005). Function of cGMP-dependent protein kinases in the nervous system. Rev. Neurosci. *16*, 23–41. https://doi.org/10.1515/revneuro.2005.16.1.23.
107. Feil, R., Hartmann, J., Luo, C., Wolfsgruber, W., Schilling, K., Feil, S., Barski, J.J., Meyer, M., Konnerth, A., De Zeeuw, C.I., et al. (2003). Impairment of LTD and cerebellar learning by Purkinje cell-specific ablation of cGMP-dependent protein kinase I. J. Cell Biol. *163*, 295–302. https://doi.org/10.1083/jcb.200306148.
108. Corum, D.G., Jenkins, D.P., Heslop, J.A., Tallent, L.M., Beeson, G.C., Barth, J.L., Schnellmann, R.G., and Muise-Helmericks, R.C. (2020). PDE5 inhibition rescues mitochondrial dysfunction and angiogenic responses induced by Akt3 inhibition by promotion of PRC expression. J. Biol. Chem. *295*, 18091–18104. https://doi.org/10.1074/jbc.RA120.013716.
109. Zhu, G., Ueda, K., Hashimoto, M., Zhang, M., Sasaki, M., Kariya, T., Sasaki, H., Kaludercic, N., Lee, D.I., Bedja, D., et al. (2022). The mitochondrial regulator PGC1alpha is induced by cGMP-PKG signaling and mediates the protective effects of phosphodiesterase 5 inhibition in heart failure. FEBS Lett. *596*, 17–28. https://doi.org/10.1002/1873-3468.14228.
110. Kaun, K.R., and Sokolowski, M.B. (2009). cGMP-dependent protein kinase: linking foraging to energy homeostasis. Genome *52*, 1–7. https://doi.org/10.1139/G08-090.
111. Paupardin-Tritsch, D., Hammond, C., Gerschenfeld, H.M., Nairn, A.C., and Greengard, P. (1986). cGMP-dependent protein kinase enhances Ca2+ current and potentiates the serotonin-induced Ca2+ current increase in snail neurones. Nature *323*, 812–814. https://doi.org/10.1038/323812a0.
112. Dason, J.S., Allen, A.M., Vasquez, O.E., and Sokolowski, M.B. (2019). Distinct functions of a cGMP-dependent protein kinase in nerve terminal growth and synaptic vesicle cycling. J. Cell Sci. *132*, jcs227165. https://doi.org/10.1242/jcs.227165.
113. Soff, G.A., Cornwell, T.L., Cundiff, D.L., Gately, S., and Lincoln, T.M. (1997). Smooth muscle cell expression of type I cyclic GMP-dependent protein kinase is suppressed by continuous exposure to nitrovasodilators, theophylline, cyclic GMP, and cyclic AMP. J. Clin. Investig. *100*, 2580–2587. https://doi.org/10.1172/JCI119801.
114. Sheng, M., Lu, H., Liu, P., Li, Y., Ravi, H., Peng, S.L., Diaz-Arrastia, R., Devous, M.D., and Womack, K.B. (2017). Sildenafil Improves Vascular and Metabolic Function in Patients with Alzheimer's Disease. J. Alzheimers Dis. *60*, 1351–1364. https://doi.org/10.3233/JAD-161006.
115. Webb, A.J.S., Birks, J.S., Feakins, K.A., Lawson, A., Dawson, J., Rothman, A.M.K., Werring, D.J., Llwyd, O., Stewart, C.R., and Thomas, J. (2024). Cerebrovascular Effects of Sildenafil in Small Vessel Disease: The OxHARP Trial. Circ. Res. *135*, 320–331. https://doi.org/10.1161/CIRCRESAHA.124.324327.

116. Baik, A.H., and Jain, I.H. (2020). Turning the Oxygen Dial: Balancing the Highs and Lows. Trends Cell Biol. *30*, 516–536. https://doi.org/10.1016/j.tcb.2020.04.005.

117. Cunnane, S.C., Trushina, E., Morland, C., Prigione, A., Casadesus, G., Andrews, Z.B., Beal, M.F., Bergersen, L.H., Brinton, R.D., de la Monte, S., et al. (2020). Brain energy rescue: an emerging therapeutic concept for neurodegenerative disorders of ageing. Nat. Rev. Drug Discov. *19*, 609–633. https://doi.org/10.1038/s41573-020-0072-x.

118. Suomalainen, A., and Nunnari, J. (2024). Mitochondria at the crossroads of health and disease. Cell *187*, 2601–2627. https://doi.org/10.1016/j.cell.2024.04.037.

119. Iwata, R., Casimir, P., Erkol, E., Boubakar, L., Planque, M., Gallego López, I.M., Ditkowska, M., Gaspariunaite, V., Beckers, S., Remans, D., et al. (2023). Mitochondria metabolism sets the species-specific tempo of neuronal development. Science *379*, eabn4705. https://doi.org/10.1126/science.abn4705.

120. Wintermark, P., Lapointe, A., Steinhorn, R., Rampakakis, E., Burhenne, J., Meid, A.D., Bajraktari-Sylejmani, G., Khairy, M., Altit, G., Adamo, M.T., et al. (2024). Feasibility and Safety of Sildenafil to Repair Brain Injury Secondary to Birth Asphyxia (SANE-01): A Randomized, Double-blind, Placebo-controlled Phase Ib Clinical Trial. J. Pediatr. *266*, 113879. https://doi.org/10.1016/j.jpeds.2023.113879.

121. Wintermark, P., Lapointe, A., Altit, G., Steinhorn, R., Rampakakis, E., Meid, A.D., Burhenne, J., Bajraktari-Sylejmani, G., Khairy, M., Adamo, M.T., et al. (2025). Testing Higher Doses of Sildenafil to Repair Brain Injury Secondary to Birth Asphyxia: An Open-Label Dose-Finding Phase 1b Clinical Trial-Sildenafil Administration to Treat Neonatal Encephalopathy-Study 02. J. Pediatr. *285*, 114701. https://doi.org/10.1016/j.jpeds.2025.114701.

122. Mukherjee, A., Dombi, T., Wittke, B., and Lalonde, R. (2009). Population pharmacokinetics of sildenafil in term neonates: evidence of rapid maturation of metabolic clearance in the early postnatal period. Clin. Pharmacol. Ther. *85*, 56–63. https://doi.org/10.1038/clpt.2008.177.

123. Blount, M.A., Beasley, A., Zoraghi, R., Sekhar, K.R., Bessay, E.P., Francis, S.H., and Corbin, J.D. (2004). Binding of tritiated sildenafil, tadalafil, or vardenafil to the phosphodiesterase-5 catalytic site displays potency, specificity, heterogeneity, and cGMP stimulation. Mol. Pharmacol. *66*, 144–152. https://doi.org/10.1124/mol.66.1.144.

124. Preston, G., Jacob, N., Elsharkawi, I., Morava, E., and Kozicz, T. (2025). Phosphodiesterase type 5 inhibition as a therapeutic strategy in primary mitochondrial disease: Evidence from patient fibroblasts and clinical observations. Mol. Genet. Metab. *146*, 109197. https://doi.org/10.1016/j.ymgme.2025.109197.

125. Perez-Riverol, Y., Bai, J., Bandla, C., García-Seisdedos, D., Hewapathirana, S., Kamatchinathan, S., Kundu, D.J., Prakash, A., Frericks-Zipper, A., Eisenacher, M., et al. (2022). The PRIDE database resources in 2022: a hub for mass spectrometry-based proteomics evidences. Nucleic Acids Res. *50*, D543–D552. https://doi.org/10.1093/nar/gkab1038.

126. Pantazis, C.B., Yang, A., Lara, E., McDonough, J.A., Blauwendraat, C., Peng, L., Oguro, H., Kanaujiya, J., Zou, J., Sebesta, D., et al. (2022). A reference human induced pluripotent stem cell line for large-scale collaborative studies. Cell Stem Cell *29*, 1685–1702.e22. https://doi.org/10.1016/j.stem.2022.11.004.

127. Lee, J.H., Park, I.H., Gao, Y., Li, J.B., Li, Z., Daley, G.Q., Zhang, K., and Church, G.M. (2009). A robust approach to identifying tissue-specific gene expression regulatory variants using personalized human induced pluripotent stem cells. PLoS Genet. *5*, e1000718. https://doi.org/10.1371/journal.pgen.1000718.

128. Wang, X., Sterr, M., Burtscher, I., Chen, S., Hieronimus, A., Machicao, F., Staiger, H., Häring, H.U., Lederer, G., Meitinger, T., et al. (2018). Genome-wide analysis of PDX1 target genes in human pancreatic progenitors. Mol. Metab. *9*, 57–68. https://doi.org/10.1016/j.molmet.2018.01.011.

129. Rössler, U., Hennig, A.F., Stelzer, N., Bose, S., Kopp, J., Søe, K., Cyganek, L., Zifarelli, G., Ali, S., von der Hagen, M., et al. (2021). Efficient generation of osteoclasts from human induced pluripotent stem cells and functional investigations of lethal CLCN7-related osteopetrosis. J. Bone Miner. Res. *36*, 1621–1635. https://doi.org/10.1002/jbmr.4322.

130. Binder, S., Ramachandran, H., Hildebrandt, B., Dobner, J., and Rossi, A. (2024). Prime-Editing of human ACTB in induced pluripotent stem cells to model human ACTB Loss-of-Function diseases and compensatory mechanisms. Stem Cell Res. *75*, 103304. https://doi.org/10.1016/j.scr.2024.103304.

131. Yu, J., Vodyanik, M.A., Smuga-Otto, K., Antosiewicz-Bourget, J., Frane, J.L., Tian, S., Nie, J., Jonsdottir, G.A., Ruotti, V., Stewart, R., et al. (2007). Induced pluripotent stem cell lines derived from human somatic cells. Science *318*, 1917–1920. https://doi.org/10.1126/science.1151526.

132. Kruse, S.E., Watt, W.C., Marcinek, D.J., Kapur, R.P., Schenkman, K.A., and Palmiter, R.D. (2008). Mice with mitochondrial complex I deficiency develop a fatal encephalomyopathy. Cell Metab. *7*, 312–320. https://doi.org/10.1016/j.cmet.2008.02.004.

133. Reinhardt, P., Glatza, M., Hemmer, K., Tsytsyura, Y., Thiel, C.S., Höing, S., Moritz, S., Parga, J.A., Wagner, L., Bruder, J.M., et al. (2013). Derivation and expansion using only small molecules of human neural progenitors for neurodegenerative disease modeling. PLoS One *8*, e59252. https://doi.org/10.1371/journal.pone.0059252.

134. Velasco, S., Kedaigle, A.J., Simmons, S.K., Nash, A., Rocha, M., Quadrato, G., Paulsen, B., Nguyen, L., Adiconis, X., Regev, A., et al. (2019). Individual brain organoids reproducibly form cell diversity of the human cerebral cortex. Nature *570*, 523–527. https://doi.org/10.1038/s41586-019-1289-x.

135. Spinazzi, M., Casarin, A., Pertegato, V., Salviati, L., and Angelini, C. (2012). Assessment of mitochondrial respiratory chain enzymatic activities on tissues and cultured cells. Nat. Protoc. *7*, 1235–1246. https://doi.org/10.1038/nprot.2012.058.

136. Pfaffl, M.W. (2001). A new mathematical model for relative quantification in real-time RT-PCR. Nucleic Acids Res. *29*, e45. https://doi.org/10.1093/nar/29.9.e45.

137. Love, M.I., Huber, W., and Anders, S. (2014). Moderated estimation of fold change and dispersion for RNA-seq data with DESeq2. Genome Biol. *15*, 550. https://doi.org/10.1186/s13059-014-0550-8.

138. Yoon, S.J., Elahi, L.S., Pașca, A.M., Marton, R.M., Gordon, A., Revah, O., Miura, Y., Walczak, E.M., Holdgate, G.M., Fan, H.C., et al. (2019). Reliability of human cortical organoid generation. Nat. Methods *16*, 75–78. https://doi.org/10.1038/s41592-018-0255-0.

139. Hao, Y., Stuart, T., Kowalski, M.H., Choudhary, S., Hoffman, P., Hartman, A., Srivastava, A., Molla, G., Madad, S., Fernandez-Granda, C., et al. (2024). Dictionary learning for integrative, multimodal and scalable single-cell analysis. Nat. Biotechnol. *42*, 293–304. https://doi.org/10.1038/s41587-023-01767-y.

140. Hafemeister, C., and Satija, R. (2019). Normalization and variance stabilization of single-cell RNA-seq data using regularized negative binomial regression. Genome Biol. *20*, 296. https://doi.org/10.1186/s13059-019-1874-1.

141. Rybak-Wolf, A., Wyler, E., Pentimalli, T.M., Legnini, I., Oliveras Martinez, A., Glažar, P., Loewa, A., Kim, S.J., Kaufer, B.B., Woehler, A., et al. (2023). Modelling viral encephalitis caused by herpes simplex virus 1 infection in cerebral organoids. Nat. Microbiol. *8*, 1252–1266. https://doi.org/10.1038/s41564-023-01405-y.

142. Aibar, S., González-Blas, C.B., Moerman, T., Huynh-Thu, V.A., Imrichova, H., Hulselmans, G., Rambow, F., Marine, J.C., Geurts, P., Aerts, J., et al. (2017). SCENIC: single-cell regulatory network inference and clustering. Nat. Methods *14*, 1083–1086. https://doi.org/10.1038/nmeth.4463.

143. Liberzon, A., Birger, C., Thorvaldsdóttir, H., Ghandi, M., Mesirov, J.P., and Tamayo, P. (2015). The Molecular Signatures Database (MSigDB) hallmark gene set collection. Cell Syst. *1*, 417–425. https://doi.org/10.1016/j.cels.2015.12.004.

144. Petersilie, L., Kafitz, K.W., Neu, L.A., Heiduschka, S., Le, S., Prigione, A., and Rose, C.R. (2024). Protocol for the generation of cultured cortical brain organoid slices. Star Protoc. *5*, 103212. https://doi.org/10.1016/j.xpro.2024.103212.

145. Xia, W., Veeragandham, P., Cao, Y., Xu, Y., Rhyne, T.E., Qian, J., Hung, C.W., Zhao, P., Jones, Y., Gao, H., et al. (2024). Obesity causes mitochondrial fragmentation and dysfunction in white adipocytes due to RalA activation. Nat. Metab. *6*, 273–289. https://doi.org/10.1038/s42255-024-00978-0.

146. Picardi, E., and Pesole, G. (2012). Mitochondrial genomes gleaned from human whole-exome sequencing. Nat. Methods *9*, 523–524. https://doi.org/10.1038/nmeth.2029.

147. Rubino, F., Piredda, R., Calabrese, F.M., Simone, D., Lang, M., Calabrese, C., Petruzzella, V., Tommaseo-Ponzetta, M., Gasparre, G., and Attimonelli, M. (2012). HmtDB, a genomic resource for mitochondrion-based human variability studies. Nucleic Acids Res. *40*, D1150–D1159. https://doi.org/10.1093/nar/gkr1086.

148. Robinson, J.T., Thorvaldsdóttir, H., Winckler, W., Guttman, M., Lander, E.S., Getz, G., and Mesirov, J.P. (2011). Integrative genomics viewer. Nat. Biotechnol. *29*, 24–26. https://doi.org/10.1038/nbt.1754.

149. Krasemann, S., Haferkamp, U., Pfefferle, S., Woo, M.S., Heinrich, F., Schweizer, M., Appelt-Menzel, A., Cubukova, A., Barenberg, J., Leu, J., et al. (2022). The blood-brain barrier is dysregulated in COVID-19 and serves as a CNS entry route for SARS-CoV-2. Stem Cell Rep. *17*, 307–320. https://doi.org/10.1016/j.stemcr.2021.12.011.

150. Haferkamp, U., Hartmann, C., Abid, C.L., Brachner, A., Höchner, A., Gerhartl, A., Harwardt, B., Leckzik, S., Leu, J., Metzger, M., et al. (2023). Human isogenic cells of the neurovascular unit exert transcriptomic cell type-specific effects on a blood-brain barrier in vitro model of late-onset Alzheimer disease. Fluids Barriers CNS *20*, 78. https://doi.org/10.1186/s12987-023-00471-y.

151. Appelt-Menzel, A., Cubukova, A., Günther, K., Edenhofer, F., Piontek, J., Krause, G., Stüber, T., Walles, H., Neuhaus, W., and Metzger, M. (2017). Establishment of a Human Blood-Brain Barrier Co-culture Model Mimicking the Neurovascular Unit Using Induced Pluri- and Multipotent Stem Cells. Stem Cell Rep. *8*, 894–906. https://doi.org/10.1016/j.stemcr.2017.02.021.

152. Lippmann, E.S., Al-Ahmad, A., Azarin, S.M., Palecek, S.P., and Shusta, E.V. (2014). A retinoic acid-enhanced, multicellular human blood-brain barrier model derived from stem cell sources. Sci. Rep. *4*, 4160. https://doi.org/10.1038/srep04160.

153. Kleinsorge, M., and Cyganek, L. (2020). Subtype-Directed Differentiation of Human iPSCs into Atrial and Ventricular Cardiomyocytes. Star Protoc. *1*, 100026. https://doi.org/10.1016/j.xpro.2020.100026.

154. Cyganek, L., Tiburcy, M., Sekeres, K., Gerstenberg, K., Bohnenberger, H., Lenz, C., Henze, S., Stauske, M., Salinas, G., Zimmermann, W.H., et al. (2018). Deep phenotyping of human induced pluripotent stem cell-derived atrial and ventricular cardiomyocytes. JCI Insight *3*, e99941. https://doi.org/10.1172/jci.insight.99941.

155. Pavez-Giani, M.G., Sánchez-Aguilera, P.I., Bomer, N., Miyamoto, S., Booij, H.G., Giraldo, P., Oberdorf-Maass, S.U., Nijholt, K.T., Yurista, S.R., Milting, H., et al. (2021). ATPase Inhibitory Factor-1 Disrupts Mitochondrial Ca^{2+} Handling and Promotes Pathological Cardiac Hypertrophy through CaMKIIδ. Int. J. Mol. Sci. *22*, 4427. https://doi.org/10.3390/ijms22094427.

156. Bertram, R., Gram Pedersen, M., Luciani, D.S., and Sherman, A. (2006). A simplified model for mitochondrial ATP production. J. Theor. Biol. *243*, 575–586. https://doi.org/10.1016/j.jtbi.2006.07.019.

157. Magnus, G., and Keizer, J. (1998). Model of beta-cell mitochondrial calcium handling and electrical activity. II. Mitochondrial variables. Am. J. Physiol. *274*, C1174–C1184. https://doi.org/10.1152/ajpcell.1998.274.4.C1174.

158. Fall, C.P., and Keizer, J.E. (2001). Mitochondrial modulation of intracellular Ca(2+) signaling. J. Theor. Biol. *210*, 151–165. https://doi.org/10.1006/jtbi.2000.2292.

159. Cortassa, S., Aon, M.A., Marbán, E., Winslow, R.L., and O'Rourke, B. (2003). An integrated model of cardiac mitochondrial energy metabolism and calcium dynamics. Biophys. J. *84*, 2734–2755. https://doi.org/10.1016/S0006-3495(03)75079-6.

160. Tran Van Nhieu, G., Kai Liu, B., Zhang, J., Pierre, F., Prigent, S., Sansonetti, P., Erneux, C., Kuk Kim, J., Suh, P.G., Dupont, G., et al. (2013). Actin-based confinement of calcium responses during Shigella invasion. Nat. Commun. *4*, 1567. https://doi.org/10.1038/ncomms2561.

161. Contreras, L., Gomez-Puertas, P., Iijima, M., Kobayashi, K., Saheki, T., and Satrústegui, J. (2007). Ca2+ Activation kinetics of the two aspartate-glutamate mitochondrial carriers, aralar and citrin: role in the heart malate-aspartate NADH shuttle. J. Biol. Chem. *282*, 7098–7106. https://doi.org/10.1074/jbc.M610491200.

162. Lytton, J., Westlin, M., Burk, S.E., Shull, G.E., and MacLennan, D.H. (1992). Functional comparisons between isoforms of the sarcoplasmic or endoplasmic reticulum family of calcium pumps. J. Biol. Chem. *267*, 14483–14489. https://doi.org/10.1016/S0021-9258(19)49738-X.

163. Maravall, M., Mainen, Z.F., Sabatini, B.L., and Svoboda, K. (2000). Estimating intracellular calcium concentrations and buffering without wavelength ratioing. Biophys. J. *78*, 2655–2667. https://doi.org/10.1016/S0006-3495(00)76809-3.

164. Csordás, G., Golenár, T., Seifert, E.L., Kamer, K.J., Sancak, Y., Perocchi, F., Moffat, C., Weaver, D., Perez, S.F., Bogorad, R., et al. (2013). MICU1 controls both the threshold and cooperative activation of the mitochondrial Ca^{2+} uniporter. Cell Metab. *17*, 976–987. https://doi.org/10.1016/j.cmet.2013.04.020.

165. Jansen, M.J.W. (1999). Analysis of variance designs for model output. Comput. Phys. Commun. *117*, 35–43. https://doi.org/10.1016/S0010-4655(98)00154-4.

166. Saltelli, A., Annoni, P., Azzini, I., Campolongo, F., Ratto, M., and Tarantola, S. (2010). Variance based sensitivity analysis of model output. Design and estimator for the total sensitivity index. Comput. Phys. Commun. *181*, 259–270. https://doi.org/10.1016/j.cpc.2009.09.018.

167. Sobol', I.M. (2001). Global sensitivity indices for nonlinear mathematical models and their Monte Carlo estimates. Math. Comput. Simul. *55*, 271–280. https://doi.org/10.1016/S0378-4754(00)00270-6.

STAR★METHODS

KEY RESOURCES TABLE

REAGENT or RESOURCE	SOURCE	IDENTIFIER
Antibodies		
Purified anti-Pax-6 antibody, rabbit polyclonal IgG	BioLegend	Cat#901301; RRID: AB_2565003
Anti-β-Tubulin III antibody, mouse monoclonal, clone 2G10 (TUJ1)	Sigma-Aldrich	Cat#T8578; RRID: AB_1841228
PRKG1 polyclonal antibody, rabbit polyclonal IgG	Proteintech	Cat#21646-1-AP; RRID: AB_2878897
Anti-Nestin antibody, mouse monoclonal IgG1, clone 10C2	Merck/ Sigma-Aldrich	Cat#MAB5326; RRID: AB_2251134
Occludin Antibody, mouse monoclonal IgG1, cloneOC-3F10	Invitrogen	Cat#33-1500; RRID: AB_2533101
ZO-1 antibody, rabbit polyclonal IgG (TJP1)	Proteintech	Cat#21773-1-AP; RRID: AB_10733242
Cleaved Caspase-3 (Asp175) antibody, rabbit polyclonal	Cell Signaling Technology	Cat#9661; RRID: AB_2341188
Anti-Iba1 antibody, mouse monoclonal IgG1, cloneEPR16589	Abcam	Cat#Ab283319; RRID: AB_2924797
ATP6 antibody, rabbit polyclonal IgG	Immunological Science	Cat#AB-83828
Anti-GAPDH antibody, mouse monoclonal IgG1, clone6C5	Abcam	Cat#Ab8245; RRID: AB_2107448
Anti-β-actin antibody, mouse monoclonal IgG1	Abcam	Cat#ab8226; RRID: AB_30637
PRKG1 antibody, rabbit polyclonal IgG	Cell Signaling Technology	Cat#3248; RRID: AB_2067450
mTOR-Ser2448 antibody, rabbit polyclonal	Cell Signaling Technology	Cat#2971; RRID: AB_330970
Phospho-AMPKa-Thr174 antibody, rabbit monoclonal	Cell Signaling Technology	Cat#2535; RRID: AB_331250
Phospho-PGC1a-Ser571 antibody, rabbit polyclonal IgG	Biotechne	Cat#AF6650; RRID: AB_10890391
Phospho-4EBP-1 antibody, rabbit monoclonal IgG	Cell Signaling Technology	Cat#2855; RRID: AB_560835
PGC1a antibody, rabbit polyclonalIgG	Novus Bio	Cat#NBP1-04676; RRID: AB_1522118
AMPKa antibody, rabbit polyclonal IgG	Cell Signaling Technology	Cat#2532; RRID: AB_330331
4EBP-1 antibody, rabbit monoclonal	Cell Signaling Technology	Cat#9644; RRID: AB_2097841
Anti-GAPDH antibody, rabbit monoclonal IgG	Abcam	Cat#ab181602; RRID: AB_2630358
Donkey anti-Rabbit IgG (H+L) Highly Cross-Adsorbed Secondary Antibody, Alexa Fluor488	Invitrogen	Cat#A-21206; RRID: AB_2535792
Donkey anti-mouse IgG Antibody, Cy3 conjugate	Millipore	Cat#AP192C; RRID:AB_92642
Donkey anti-rabbit IgG (H+L) Highly Cross-Absorbed Secondary Antibody, Alexa Fluor647	Invitrogen	Cat# A32795; RRID:AB_2762835
Goat anti-Mouse IgG (H+L) Cross-Adsorbed Secondary Antibody, Alexa Fluor633	Invitrogen	Cat#A-21050
Goat Anti-Mouse IgG (H + L)-HRP Conjugate	BioRad	Cat#1706516; RRID: AB_2921252
Anti-Rabbit IgG (H+L), HRP Conjugate	Promega	Cat#W4018
Anti-Mitofilin antibody (MIC60), monoclonal IgG, clone EPR8749	Abcam	Cat#Ab137057; RRID: AB_3676556

(Continued on next page)

Continued

REAGENT or RESOURCE	SOURCE	IDENTIFIER
Anti-ACTN2 antibody (alpha-actinin), mouse monoclonal, clone EA-53	Sigma-Aldrich	Cat#A7811; RRID: AB_476766
Anti-ATP5B antibody, rabbit polyclonal	Sigma-Aldrich	Cat#HPA001528; RRID: AB_1078242
NDUFA9 antibody, mouse monoclonal IgG, clone 20C11B11B11	Invitrogen	Cat#459100; RRID: AB_10376187
Anti-SDHB, mouse monoclonal IgG2a, clone 21A11EA7	Abcam	Cat#ab14714; RRID: AB_301432
Anti-UQCRSF1/RISP antibody, mouse monoclonal IgG2b, clone 5A5	Abcam	Cat#ab14746; RRID: AB_301445
Doublecortin antibody (DCX), rabbit	Cell Signaling Technology	Cat#4604; RRID: AB_561007
Chemicals, peptides, and recombinant proteins		
StemMACSiPS-Brew XF, human	Miltenyi Biotec	Cat#130-104-368
mTeSRPlus	STEMCELL Technologies	Cat#100-0276
KnockOut-DMEM	Gibco	Cat#10829-018
KnockOutserum replacement (SR)	Gibco	Cat#10828-028
DMEM/F/12	Gibco	Cat#31330038
DMEM glucose-free	Gibco	Cat#11966025
Glasgow-MEM	Gibco	Cat#11710035
Neurobasal A-Medium glucose-free	Gibco	Cat#A2477501
Neurobasal	Gibco	Cat#21103-049
Non-essential amino acids (MEM-NEAA) 100X	Gibco	Cat#11140-050
Sodium pyruvate	Gibco	Cat#11360070
B-27 with Vitamin A (50×)	Gibco	Cat#17504044
B-27 without Vitamin A (50×)	Gibco	Cat#12587010
N2 Supplement (100×)	Gibco	Cat#17502-048
DPBS, no calcium, no magnesium	Gibco	Cat#14190144
Accutase	Thermo Fisher Scientific; Sigma-Aldrich	Cat#A1110501; Cat#A6964-100ML
UltraPure0.5 M EDTA	Invitrogen	Cat#11568896
ROCK inhibitor Y-27632	Enzo Life Sciences	Cat#ALX-270-333-M005
MycoZap Plus-CL	Lonza	Cat#VZA-2012
Penicillin/Streptomycin	Gibco	Cat#15140122
GlutaMAX	Gibco	Cat#35050061
L-glutamine	Gibco	Cat#25030081
FBS	Gibco	Cat#10270106
Matrigel, Growth Factor Reduced	Corning	Cat#356231
GeltrexReduced-Growth Factor Basement-Membrane Matrix, LDEV-free, stem-cell qualified	Gibco	Cat#A1413302
Chemically Defined Lipid Concentrate	Gibco	Cat#11905031
Anti-Adherence Rinsing Solution	STEMCELL Technologies	Cat#07010
Purmorphamin	Sigma-Aldrich; Miltenyi Biotec	Cat#540220; Cat#130-104-465
CHIR 99021	Sigma-Aldrich	Cat#SML1046
Dorsomorphin	Sigma-Aldrich	Cat#P5499
SB431542	Miltenyi Biotec	Cat#130-105-336
GDNF	R&D System	Cat#212-GD-010
BDNF	MACS Miltenyi	Cat#130-096-811
EGF	R&D System	Cat#236-EG-200
FGF2	R&D System	Cat#3718-FB-100

(*Continued on next page*)

Continued

REAGENT or RESOURCE	SOURCE	IDENTIFIER
Dibutyryl-cAMP	StemCell Technologies	Cat#73886
Recombinant Human NT-3	Peprotech / Biozol	Cat#450-03
FGF8-a	R&D systems	Cat#4745-F8-050
TGF-beta 3	STEMCELL Technologies	Cat#78156
(+)-sodium L-ascorbate (Vitamin C)	Sigma-Aldrich	Cat#A4034
cis-4,7,10,13,16,19-Docosahexaenoic acid methyl ester (DHA)	Sigma-Aldrich	Cat#D2534
WNT antagonist IWR1	EMD Millipore Corp	Cat#681669
Heparin	Merck	Cat#375095
ß-mercaptoethanol	Gibco	Cat#31350010
DMSO	Sigma-Aldrich	Cat#D2650-100ML
SuperSignal West Pico PLUS Chemiluminescent Substrate	Thermo Fisher Scientific	Cat#34580
16% Paraformaldehyde (PFA)	Thermo Fisher Scientific	Cat#28906
Hoechst 33342	Invitrogen	Cat#H3570
Donkey serum (DNS)	Merck Millipore	Cat#S30
Triton X-100	Sigma-Aldrich	Cat#93443; Cat#93426
Tween 20	Sigma-Aldrich	Cat#P1504
abberior STAR 635 (STAR RED)	Abberior	Cat#ST635-1002
DAPI	Sigma-Aldrich	Cat#D9542
MitoProbeTMRM Assay Kit for Flow Cytometry	Invitrogen	Cat#M20036
Tetramethylrhodamine methyl ester (TMRM)	Invitrogen	Cat#T668
Incucyte dye red	Sartorius	Cat#4717
Calcein AM Viability Dye	Invitrogen	Cat#C1430
MitoSpyOrange	BioLegend	Cat#424803
d_3-Sildenafil	CDN isotopes	Cat#D-6366
HpaII	NEB	Cat#R0171
StuI	NEB	Cat#R0187
XbaI	NEB	Cat#R0145
FCCP	Biozol	Cat#SEL-S8276
Antimycin A	Sigma-Aldrich	Cat#A8674
Oligomycin	Sigma-Aldrich	Cat#O4876-5MG
CCCP	Sigma-Aldrich	Cat#555602
Propidium iodide	Invitrogen	Cat#P1304MP
Sildenafil citrate	Sigma-Aldrich	Cat#SML3033
KT5823	Biomol	Cat#LKT-K7602.100
8-Br-cGMP	Sigma-Aldrich	Cat#203820
Sildenafil	Selleckchem	Cat#S468402 and S468403
Mowiol with 0.1% 1,4-Diazabicyclo[2.2.2]octan (DABCO)	Carl Roth	Cat#0713.1
LB Agar	Sigma-Aldrich	Cat#L2897
SuperFrost Plus glass slides	VWR	Cat#631-0447
Pro-Long Glass Antifade Mountant	Invitrogen	Cat#P36984
oligo d(T)18 primers	Thermo Fisher Scientific	Cat#SO132
dNTP mix	Thermo Fisher Scientific	Cat#10319879
Rnase OUT Recombinant Ribonuclease Inhibitor	Invitrogen	Cat#10777-019
M-MLV Reverse Transcriptase (200 U/µL)	Invitrogen	Cat#28025021

(*Continued on next page*)

Continued

REAGENT or RESOURCE	SOURCE	IDENTIFIER
Human Endothelial-SFM	Gibco	Cat#11111044
hFGF	Peprotech	Cat#100-18B
Retinoic acid	STEMCELL Technologies	Cat#72262
Collagen IV	Sigma-Aldrich	Cat#c5533-5MG
Fibronectin	Gibco/Thermo Fisher Scientific	Cat#33016015
Transwell membranes	Greiner	Cat#662641
Sodium fluorescein	Sigma-Aldrich	Cat#F6377-100G
Diazepam	Sigma-Aldrich	Cat#D0899-100MG
Atenolol	Sigma-Aldrich	Cat#A7655-1G
LysC	Roche	Cat#11420429001
Low melting temperature agarose	Gibco	Cat#5517UB
Hank’s Balanced Salt Solution (HBSS)	Sigma-Aldrich	Cat#H9394
Oregon Green 488 BAPTA-1 AM	Invitrogen	Cat#O6807
Deoxy-D-glucose	Apollo Scientific; Sigma-Aldrich	Cat#OR3900T; Cat#D8375-1g
RNase H	Epicentre/ LGC Biosearch Technologies	Cat#E0038-5D1
Acetonitrile	Biosolve, ULC/MS-CC/SFC	Cat#001204101BS
Fura-2 AM	Thermo Fisher Scientific	Cat#F1221
Thapsigargin	Thermo Fisher Scientific	Cat#T7459
Trypsin	Sigma-Aldrich/ Merck	Cat#T4799
$CaCl_2$	Sigma-Aldrich/ Merck	Cat#C7902
Altrenogest	MSD Animal Health	Regumate
PGF2-alpha ($PGF_{2\alpha}$)	Fatro S.P.A.	Prosolvin®
Critical commercial assays		
CellTiter-GloLuminescent Cell Viability assay	Promega	Cat#G7571
Rnase-Free Dnase Set (50) (250)	Qiagen	Cat#79254
RNeasy Mini Kit (50)	Qiagen	Cat#74104
Nucleo-Spin Tissue kit	Macherey-Nagel	Cat#740952.50
SYBR Green PCR Master Mix	Applied Biosystems	Cat#4364344
Bicinchoninic Acid (BCA) protein assay kit	Thermo Fisher Scientific	Cat#23252
NucleoSpin RNA Plus kit	Macherey-Nagel	Cat#740984.50
RNA Cleanup XP beads	Agencourt/Beckman coulter	Cat#A66514
TURBO DNase rigorous treatment	Invitrogen	Cat#AM1907
TruSeq Stranded Total LT Sample Prep Kit	Illumina	RS-122-2201, RS-122-2202
Chromium Single Cell 3′ (vNext) Reagent Kit	10X Genomics	Cat#PN-1000268 (16 rxns) or PN-1000269 (4 rxns)
ViaLight Plus Kit	Lonza	Cat#LT07-221
CyQUANT Cell Proliferation Assay	Invitrogen	Cat#C7026
jetPRIME transfection	Polyplus	Cat#101000027
Deposited data		
Bulk RNAses NPCs dataset	This paper	https://www.ncbi.nlm.nih.gov/geo/query/acc.cgi?acc=GSE292178; GEO: GSE292178
Bulk RNAseq organoids dataset	This paper	https://www.ncbi.nlm.nih.gov/bioproject/?term=PRJNA1248577SRA; BioProject ID: PRJNA1248577
Codes	This paper	https://github.com/tpentim/Leigh_Sildenafil_Organoids
snRNAseq organoids dataset	This paper	https://www.ncbi.nlm.nih.gov/geo/query/acc.cgi?acc=GSE293573; GEO: GSE293573

(*Continued on next page*)

Continued

REAGENT or RESOURCE	SOURCE	IDENTIFIER
Proteomics NPCs dataset	This paper	https://www.ebi.ac.uk/pride/archive/projects/PXD059519; ProteomeXchange: PXD059519
Metabolomics NPCs dataset	This paper	https://massive.ucsd.edu/ProteoSAFe/dataset.jsp?task=ee42368caf914a948db5983afe2460e4; MassIVE: MSV000097182
Experimental models: Cell lines		
Human iPSCs: HMGUi001-A	Helmholtz Zentrum München (HMGU)	PMID: 29396371
Human iPSCs: HHUUKDi009-A	Heinrich-Heine-Universität Düsseldorf (HHUUKD)	PMID: 28132834
Human iPSCs: CRMi003-A	RUCDR Infinite Biologics	PMID: 36459969
Human iPSCs: BIHi269-B	Berlin Institute of Health (BIH)	PMID: 36669241
Human iPSCs: HVRDi004-B	Synthego	PMID: 19911041
Human iPSCs: IUFi004-A	Cell Applications	PMID: 38217996
Human iPSCs: BIHi266-A	Berlin Institute of Health (BIH)	PMID: 36669241
Human iPSCs: WISCi004-B	WiCell	PMID: 18029452
Human iPSCs: UMGi014-C	University Medical Center Goettingen (UMG)	PMID: 33905594
Human iPSCs: HHUi001-A	Universitätsklinikum Düsseldorf (HHU)	PMID: 28132834
Human iPSCs: HHUi002-A	Universitätsklinikum Düsseldorf (HHU)	PMID: 28132834
Human iPSCs: HHUi003-C	Universitätsklinikum Düsseldorf (HHU)	PMID: 36137325
Human iPSCs: MDCi008-A	Max Delbrück Center Berlin Buch (MDC)	PMID: 35279592
Human iPSCs: MDCi009-A	Max Delbrück Center Berlin Buch (MDC)	PMID: 35279592
Human iPSCs: MDCi010-A	Max Delbrück Center Berlin Buch (MDC)	PMID: 35279592
Human iPSCs: BIHi267-B	Berlin Institute of Health (BIH)	PMID: 36669241
Human iPSCs: HMGUi001-A-64	Max Delbrück Center Berlin Buch (MDC)	PMID: 33771987
Human iPSCs: HVRDi004-B-6	Max Delbrück Center Berlin Buch (MDC)	PMID: 36741056
Human iPSCs: HVRDi004-B-7	Max Delbrück Center Berlin Buch (MDC)	PMID: 36741056
Experimental models: Organisms/strains		
Germline *Ndufs4* KO, C57/BL6/J background	University of Washington	PMID: 20534480
SURF1 KO pig, Large White background	Avantea	PMID: 29601977
Oligonucleotides		
See Table S5 for oligonucleotides	N/A	N/A
Software and algorithms		
CellProfiler	https://cellprofiler.org/	v.4.2.5.; RRID: SCR_007358
GraphPad Prism	GraphPad Software	v.5.01; RRID: SCR_007358
Adobe Illustrator	Adobe	v.29.6; RRID: SCR_010279
Cell Ranger	10x Genomics	v.7.10; RRID: SCR_017344
Ultivo triple-quadrupole mass spectrometer	Agilent Technologies; https://www.agilent.com/en/product/liquid-chromatography-mass-spectrometry-lc-ms/lc-ms-instruments/ultivo-lcms	N/A
MassHunter Software	Agilent Technologies	N/A; RRID: SCR_015040
MToolBox	https://github.com/mitoNGS/MToolBox[126]	v.1; RRID: SCR_012112
ImageJ	Fiji[127]; http://imagej.org	v1.53q and v1.54g; RRID: SCR_003070
IGV viewer	IGV; https://igv.org	v2.163; RRID: SCR_011793
CELLCYTE Studio	Cytena	N/A; RRID: SCR_021911
ZEN Microscopy Software	Zeiss	v.3.2RRID: SCR_013672
ND-1000 software	Thermo Fisher Scientific	v3.8.1; RRID: SCR_016517

(*Continued on next page*)

Continued

REAGENT or RESOURCE	SOURCE	IDENTIFIER
CFX96 software	Bio-Rad	N/A; RRID: SCR_018064
Image Lab software	Bio-Rad	v.6.1; RRID: SCR_014210
GeneMapper ID	Applied Biosystems	v.3.2.1; RRID: SCR_021103
Xcalibur software	Thermo Fischer Scientific	N/A; RRID: SCR_014593
TraceFinder 5.1 software	Thermo Fischer Scientific	N/A; RRID: SCR_023045
Columbus software	Revvity	v.2.9.0
FlowJo software	FlowJo	v.7.6; RRID: SCR_008520
OriginPro Software	OriginLab Corporation	N/A; RRID: SCR_014212
nfcore/rnaseq	https://zenodo.org/records/7998767	v.3.12.0
Trim Galore!	Babraham Bioinformatics; https://zenodo.org/records/7598955	v.0.6.10; RRID: SCR_011847
STAR aligner	https://github.com/alexdobin/star/releases	v. 2.7.10a; RRID: SCR_004463
Salmon	https://github.com/COMBINE-lab/salmon/releases	v.1.10.1; RRID: SCR_017036
DESeq2 package	https://github.com/thelovelab/DESeq2	v. 1.40.2 and v.7.5.1; RRID: SCR_015687
ClusterProfiler	DOI: 10.18129/B9.bioc.clusterProfiler	v4.8.3 and v4.10.0; RRID: SCR_016884
org.Hs.eg.db	DOI: 10.18129/B9.bioc.org.Hs.eg.db	v.3.18.0; RRID: SCR_024739
ggplot2	https://github.com/tidyverse/ggplot2/releases/tag/v3.5.1	v.3.5.1; RRID: SCR_014601
R	The R Project for Statistical Computing	v. 4.4.1; RRID: SCR_001905
Seurat	https://satijalab.org/seurat/ version: https://github.com/satijalab/seurat/releases	v. 5.1.0; RRID: SCR_016341
AUCell package	DOI: 10.18129/B9.bioc.AUCell	v. 1.26.0; RRID: SCR_021327
MsigDB package	https://data.broadinstitute.org/gsea-msigdb/msigdb/release/7.5.1/	v 7.5.1; RRID: SCR_022870
dplyr	https://cran.r-project.org/web/packages/dplyr/index.html	v. 1.1.4; RRID: SCR_016708
Dia-NN	https://github.com/vdemichev/DiaNN/releases/tag/1.8.1	v1.8.1; RRID: SCR_022865
OmicsNet platform	https://www.omicsnet.ca/	v.2.0
CytoNCA plugin	Cytoscape	v.3.10.2
KEGG database	GenomeNet	Release 112.0; RRID: SCR_001120
Vevo 2700 analysis software	FUJIFILM VisualSonics	v.1.5; RRID: SCR_015816
NIS-Elements Advanced Research	Nikon	v.3.2; RRID: SCR_027181
EZ-C1 Silver	Nikon	v.3.91
MATLAB 2023b	MathWorks; https://de.mathworks.com/products/new_products/release2023b.html	RRID:SCR_001622
IncuCyte Live-Cell Analysis System	Sartorius	RRID: SCR_023147
Other		
CytoSmart Cell Counter	Greiner Bio-One	Cat#6749
Orbital Shaker Heidolph Unimax 1010	Heidolph	Cat#543-12310-00
Operetta CLS	Revvity	Cat#HH16000020; RRID: SCR_018810
96-well Cell Culture Microplate, PS, F-Bottom, black TC, µCLEAR, 96-well black, clear bottom	Greiner Bio-One	Cat#655090
96-well Cell Culture Microplate, SCREENSTAR	Greiner Bio-One	Cat#655866
µ-Plate 96 Well Square	Ibidi	Cat#89626
DMS1000 microscope	Leica Microsystems	DMS1000
Eclipse Ts2	Nikon	Inverted Microscope; RRID: SCR_025716

(*Continued on next page*)

Continued

REAGENT or RESOURCE	SOURCE	IDENTIFIER
ZEISS Axio Observer Apotome 3	Zeiss	ZEISS Apotome 3: Optical sectioning in widefield fluorescence microscopy
ZEISS Axio Observer 7 inverted microscope	Zeiss	Inverted Microscope; RRID:SCR_023694
Magnification changer	Zeiss	Tuelens Optovar
Wavelength switcher	Sutter Instruments	Sutter Lambda DG5
Vibratome Microm HM 650 V	Thermo Fisher Scientific	Cat#920120
Multimode plate reader	Revvity	EnSight
CELLCYTE X	Cytena	CELLCYTE X™ - Live Cell Imager And Analyzer | CYTENA; RRID: SCR_021911
INFINITY platform	Abberior Instruments	INFINITY - @abberior.rocks
Promethion	Sable Systems International	Promethion Core Metabolic and Behavioral Phenotyping Systems
Infinite M1000 Pro	TECAN	Tecan | Thermo Fisher Scientific - DE; RRID: SCR_024561
Confocal laser scanning microscope C1	Nikon Mikroskope Solutions	Nikon's Digital Eclipse C1 Microscope System Delivers High Resolution Confocal Images at Sensible Price | News | Nikon Instruments Inc.
Mastercycler X50s	Eppendorf	6311000010; RRID: SCR_027059
CFX96Real-Time System qPCR machine	Bio-Rad	CFX96 Touch Real-Time PCR Detection System | Bio-Rad; RRID: SCR_018064
ChemiDoc MP Imaging system	Bio-Rad	ChemiDoc MP Imaging System | Bio-Rad; RRID: SCR_019037
Low-attachment U-bottom 96-well plates	Corning	Cat#3474
AggreWell	STEMCELL Technologies	Cat#34815
NovaSeq 6000 system	Illumina	NovaSeq 6000 System | Powerful sequencing with scalable throughput; RRID: SCR_016387
Dionex Ultimate 3000	Thermo Fisher Scientific	UltiMate 3000 HPLC and UHPLC Systems; RRID: SCR_019840
timsTOF SCP mass spectrometer	Bruker Daltonics	timsTOF SCP | Bruker; RRID: SCR_026542
SeQuant ZIC-pHILIC	Merck	Cat#1.50462
LSR-Fortessa X-20	Becton, Dickinson	LSRFortessa™ X-20 | Benchtop Flow Cytometer
384-well black-wall, clear-bottom plates	Revvity	Cat#6007460
Multidrop liquid dispenser	Thermo Fisher Scientific	https://www.thermofisher.com/de/de/home/life-science/lab-equipment/microplate-instruments/multidrop-dispensers.html
Rotating incubator	Thermo Electron	Cytomat
Echo 550	Beckman Coulter (Labcyte)	RRID: SCR_027476
Janus MDT	Revvity	Cat#YJLM001
Victor Multiple Plate Reader Spectrophotometer	Revvity	Cat#HH35000500
Millicell-CM inserts	Merck (MilliporeSigma in the USA)	https://www.sigmaaldrich.com
Eclipse FN-1	Nikon	ECLIPSE FN1 | Upright Microscopes | Microscope Products | Nikon Instruments Inc.
Eclipse 90i Upright Microscope	Nikon	RRID: SCR_020335
FLASH 4.0 LT camera	Hamamatsu Photonics	RRID: SCR_021971
NanoDrop 2000 Spectrophotometer	Thermo Fisher Scientific	RRID: SCR_018042
Nanodrop 1000 Spectrophotometer	peQlab	RRID: SCR_016517
Aurora Ultimate column	IonOpticks,	N/A
H-ESI source probe	Thermo Fisher Scientific	N/A

(*Continued on next page*)

Continued

REAGENT or RESOURCE	SOURCE	IDENTIFIER
In-house standard library	Merck	MSMLS-1EA library
1290 Infinity II HPLC	Agilent Technologies	https://www.agilent.com/en/product/liquid-chromatography/hplc-systems/gpc-sec-solutions/1290-infinity-ii-gpc-sec-system; RRID: SCR_019375
HPLC column	Agilent Technologies	Poroshell 120 EC-C18 column
3,500 Series Genetic Analyzer	Applied Biosystems	RRID: SCR_021901
Seahorse XFe24 Analyzer	Agilent Technologies	RRID: SCR_019539
IncuCyte	Sartorius	RRID: SCR_023147
Thermal camera	Dongguan Xintai Instrument Co., Ltd,	Cat#HT-18
Chemiluminescent Western Blot imager	Azure byosystem	Aerogene 300Q; RRID: SCR_026671

EXPERIMENTAL MODEL AND STUDY PARTICIPANT DETAILS

Induced pluripotent stem cells (iPSCs)

MT-ATP6 mutant iPSC lines were previously derived from three patients with m.9185T>C variant (ATP61_1: HHUi001-A; ATP6_2: HHUi002-A; ATP6_3: HHUi003-C), one patient with m.8993T>C variant (ATP6_4: MDCi008-A), two patients with m.8993T>G variant (ATP6_5: MDCi009-A; ATP6_6: MDCi010-A), and one patient with m.9176T>G variant (ATP6_7: BIHi267-B) (Figure S10H).[27,33–35] Genotyping of the lines was carried out by Sanger sequencing (Figure S1A). *SURF1* mutant iPSC isogenic lines (SURF1_1: HMGUi001-A-64) and *NDUFS4* mutant iPSC isogenic lines (NDUFS4_1: HVRDi004-B-6; NDUFS4_2: HVRDi004-B-7) were previously derived (Figure S10H).[25,89] Among healthy control iPSCs (Figure S10H), CTRL_1, (HMGUi001-A), CTRL_2 (HHUUKDi009-A), CTRL_4 (BIHi269-B), CTRL_7 (BIHi266-A), and CTRL_9 (UMGi014-C) were previously described,[27,33,128,129] CTRL_3 (CRMi003-A)[126] was purchased from RUCDR Infinite Biologics, CTRL_5 (HVRDi004-B, PGP1)[127] was purchased from Synthego, CTRL_6 (IUFi004-A, iPS12)[130] was purchased from Cell Applications, and CTRL_8 (WISCi004-B)[131] was purchased from WiCell. We cultured all iPSC lines on Matrigel (Corning)-coated plates using StemMACS iPS-Brew XF medium, supplemented with MycoZap (Lonza). CTRL_8 and ATP6_2 iPSCs were cultured in mTeSR Plus Medium (STEMCELL Technologies) prior to BCEC differentiation. Information on sex and age of the individuals from which the iPSCs were derived is provided in Figure S10H. We cultivated all iPSCs in a humidified atmosphere of 5 % CO_2 at 37 °C and 5 % oxygen. iPSCs were split at 70-80 % confluence with 0.5 μM EDTA (Invitrogen) in 1 x PBA (Gibco). We added 10 μM ROCK inhibitor (Enzo Biochem Inc) after splitting to promote survival. Cultures were routinely monitored for mycoplasma contamination by PCR using nine primers to amplify the six most common mycoplasma strains (Table S5). The positive control and internal contro were kindly provided by Dr. Cord Uphoff (DZMS, Germany). We monitored the identity of iPSCs using STR analysis, which was performed by the Forensic Department of the University Hospital Düsseldorf (Dr. Petra Böhme); 21 microsatellite loci were amplified using PCR and tagged products were analyzed using GeneMapper ID v.3.2.1 (Applied Biosystems). The use of iPSCs in pseudoanonymized manner was approved by the local ethic committees of Charité-Universitätsmedizin Berlin (EA2/131/13 and EA2/107/14) and Heinrich Heine University Düsseldorf (Study number 2020-967_5).

Animals

Germline *Ndufs4* KO mice were obtained from the University of Washington.[132] All mice were on the C57/BL6/J background and were fed the regular diet from Harlan Teklad.[132] Sildenafil citrate treatment was initiated soon after weaning and genotyping, between day 25-30 of age. Treatment studies were carried out in 16 female mice and 14 male mice. Mouse experiments were approved by the Institutional Animal Care and Use Committee (IACUC) of Johns Hopkins University, USA (M023M236).

Domestic pigs of large white background were used to study *SURF1* KO. Male KO animals were compared to sex and age-matched WT animals. 7 *SURF1* KO male animals were treated with sildenafil citrate starting immediately after birth. On the first day after birth, pigs were fed reconstituted milk (NeoPig Rescue, Provimi, 10-12 ml every hour) via gastric tube. By the second day, WT piglets and almost all sildenafil-treated *SURF1* KO piglets began drinking milk independently from an automatic feeder connected to the incubator. At day 30 after birth, pigs were transferred to the breeding cages and gradually switched from reconstituted milk to pelleted feed. Experiments in pigs were carried out according to the ARRIVE guidelines and approved by the Local Ethics Committee of Avantea, in accordance with the Italian Law (D.Lgs 26/2014) and EU directive 2010/63/EU regulating animal experimentation and approved by relevant authorities (Ministry of Health project # 367/2022-PR).

Cell lines

Big-conductance calcium-activated potassium (BKCa) KO human U87 glioblastoma lines with stably deletion of the *KCNMA1* gene, encoding for BKCa,[80] were kindly provided by Prof. Adam Szewczyk (Nencki Institute, Warsaw). WT and BKCa KO glioblastoma (U-87 MG) cells were grown in DMEM medium (Thermo Fisher Scientific) with 10 % fetal bovine serum (FBS) (Gibco) 100 U/ml penicillin and 100 μg/ml streptomycin (Gibco) in a humidified atmosphere of 5 % CO_2 at 37 °C.[80]

Human participants

The off-label individual basis treatment with sildenafil citrate (Revatio®) in LS patients carrying *MT-ATP6* variants was registered on ClinicalTrials.gov (ID: NCT06967831). The treatment was performed as "individual basis treatment", also known as "named-patient basis (NPB) therapy", which refers to pre-authorization access to unauthorized medicines requested by doctors for specific patients with serious unmet needs. In this treatment, the physicians carry an individual responsibility and there is no requirement of formal approval by EMA or a local IRB. This process is governed by national legislation within each EU Member State, under Article 5(1) of Directive 2001/83/EC. Patients were of Caucasian ethnicity and included both male and female individuals (according to sex assigned at birth). Details of patient features and clinical outcomes are reported in Tables 1, S3, and S4. We obtained written informed consent to use patient material and health data from the patients and their guardians according to the Declaration of Helsinki.

METHOD DETAILS

Neural precursor cells (NPCs) and differentiated neurons

We obtained NPCs from iPSCs using our previously published protocol.[133] Briefly, we detached iPSCs from Matrigel-coated plates using Accutase (Sigma-Aldrich) and transferred the collected cells into low-attachment 6-well plates where they were kept for two days in: KnockOut-DMEM (Thermo Fisher Scientific), KnockOut-SR (Thermo Fisher Scientific), non-essential amino acids (NEAA) (Thermo Fisher Scientific), plus 1 mM pyruvate (Thermo Fisher Scientific) 2 mM L-glutamine (Thermo Fisher Scientific), 1 x MycoZap Plus-CL (Lonza) with the addition of 0.5 μM purmorphamine (PMA) (Merck Millipore), 3 μM CHIR 99021 (Cayman Chemical), 10 μM SB-431542 (Selleckchem), and 1 μM dorsomorphin (Sigma-Aldrich). From day 2 to day 4, the media was switched to: Neurobasal:DMEM/F12 (Thermo Fisher Scientific) [1:1], 0.5 x N2, 0.5 x B27 without vitamin A, 1 x MycoZap Plus-CL, with the addition of 0.5 μM purmorphamine (PMA) (Merck Millipore), 3 μM CHIR 99021 (Cayman Chemical), 10 μM SB-431542 (Selleckchem), and 1 μM dorsomorphin (Sigma-Aldrich). On day 6, we transferred the suspended cells onto Matrigel-coated well plates using: the same media without SB-431542 and dorsomorphin, but with the addition of 150 μM ascorbic acid (Sigma-Aldrich). We maintained NPCs on this media and used them for experiments between passage 7 and passage 30.

Differentiation into neuronal cultures containing dopaminergic neurons was performed as previously described.[25] Briefly, starting from NPCs at low confluence (10-30 %), we switched to media containing Neurobasal:DMEM/F12 (1:1), 0.5 x N2, 0.5 x B27 with vitamin A, 1 x MycoZap Plus-CL, with the addition of 200 mM vitamin C, 100 ng/ml FGF8 (R&D Systems) and 1 mM PMA. After 8 days, we used the media Neurobasal:DMEM/F12 (1:1), 0.5 x N2, 0.5 x B27 with vitamin A, 1 x MycoZap Plus-CL, supplemented with 200 mM vitamin C, 0.5 mM PMA, 500 mM cAMP (STEMCELL Technologies), 10 ng/mL BDNF (MACS Miltenyi), 10 ng/ml GDNF (MACS Miltenyi) and 1ng/mL TGF-beta 3 (MACS Miltenyi). After ten days, the medium was changed to Neurobasal:DMEM/F12 (1:1), 0.5 x N2, 0.5 x B27 with vitamin A, 1 x MycoZap Plus-CL, supplemented with 200 mM vitamin C, 500 mM cAMP, 10 ng/ml BDNF, 10 ng/ml GDNF, and 1 ng/ml TGF-beta 3.

Cortical brain organoids

Cortical brain organoids were generated following two protocols (Figure S7A). The first protocol was based on our modifications[62] of a previous publication.[134] Briefly, on day 0, iPSCs at 80 % confluence were seeded into low-attachment U-bottom 96-well plates (Corning) to induce neurosphere formation. iPSCs were washed with DPBS (Gibco) and detached with Accutase (Gibco) for 5 min at 37 °C. Cell pellets were resuspended in cortical differentiation medium I (CDMI) consisting of Glasgow-MEM, 20 % Knockout Serum Replacement, MEM-NEAA, sodium pyruvate, 2-mercaptoethanol and penicillin-streptomycin (all from Gibco). After cell counting, the suspension was diluted with CDMI to a final cell concentration of 90,000 cells per ml and supplemented with 20 μM ROCK inhibitor (Enzo), 5 μM TGF-β inhibitor SB431542 (Cayman Chemical Company) and 3 μM WNT antagonist IWR1 (EMD Millipore Corp). The supplemented seeding suspension was distributed to low attachment U-bottom 96-well plates by adding 100 μl per well and incubated at 37 °C and 5 % CO_2. On day 3, the sides of the 96-well plates were carefully tapped to detach dead cells, and then 100 μl of CDMI supplemented with 20 μM ROCK inhibitor, 3 μM IWR1 and 5 μM SB431542. On days 6, 9, 12 and 15, 80 μl of the supernatant medium were removed from each well and replaced with 100 μl of CDMI supplemented with 3 μM IWR1 and 5 μM SB431542 per well. On day 18, the developing organoids were transferred to 100 mm petri dishes filled with cortical differentiation medium II (CDMII) consisting of DMEM/ F12, 1 % GlutaMAX, 1 % N2 supplement, 1 % chemically defined lipid concentrate and penicillin-streptomycin (Gibco). The petri dishes were placed on an orbital shaker at 70 rpm at 37 °C and 5 % CO_2. CDMII was changed every second day. On day 35, CDMII was replaced with cortical differentiation medium III (CDMIII) that in addition contains 10 % FBS (Gibco) and heparin (Merck). CDMIII was changed every two to four days, depending on the colour of the medium. From day 70 on, organoids were kept in cortical differentiation medium IV (CDMIV) that additionally was supplemented with 1 % B27 with vitamin A.

The second protocol was based on a different publication.[63] For this, AggreWell plates (STEMCELL Technologies) were prepared by incubation with Anti-Adherence Rinsing Solution (STEMCELL Technologies) for 15 min. iPSCs were detached from the 6-well plates using Accutase as described above. The cell suspension was pelleted at 200 x g for 4 min and resuspended in iPS Brew (Miltenyi Biotec) with 10 μM ROCK inhibitor. Cells were counted with CytoSmart Cell Counter (Greiner Bio-One) and 2.75 million cells were seeded in 1.5 ml per AggreWell. AggreWell plates were centrifuged at 100 x g for 3 min and left at 37 °C and 5 % CO_2 for 24 h. On day 1, spheroids were transferred to a petri dish using a cut P1000 tip and placed on a shaker. Medium was changed to embryonic stem (ES) medium composed of KO-DMEM, 20% Knockout Serum Replacement, MEM-NEAA, sodium pyruvate, GlutaMAX, penicillin-streptomycin (all from Gibco), and MycoZAP Plus-CL (Lonza), and supplemented with 10 μM SB431542 and 2.5 μM dorsomorphin (Sigma). Until day 6, ES medium was changed daily. Neurospheres were fed with Neural Differentiation Medium (NDM) consisting of Neurobasal A medium (Gibco), GlutaMAX, penicillin-streptomycin, MycoZAP and 2 % B27 without vitamin A (Gibco). From day 6-15, medium was changed daily and supplemented with 20 ng/ml EGF (R&D Systems) and 20 ng/ml FGF2 (R&D Systems). From day 16-21, medium was changed every second day, and from day 22-45, NDM medium was supplemented with 20 ng/ml BDNF (MACS Miltenyi), 20 ng/ml NT-3 (Peprotech), 200 μM (+)-sodium L-ascorbate (Sigma-Aldrich), 50 μM dibutyryl cAMP (STEMCELL Technologies), and 10 μM DHA (Sigma Aldrich), and changed every other day. For long-term maturation after day 46, NDM medium was prepared with 2 % B27 with vitamin A, and organoids were fed according to their needs. Images of brain organoids were acquired using the Eclipse Ts2 light microscope (Nikon), and at later growth stages, when the organoids were larger, using a DMS1000 microscope (Leica). The size of the organoids was determined by area calculation using ImageJ.

Assessment of mitochondrial membrane potential (MMP)

For MMP quantification, we applied a high-content analysis (HCA)-based live-cell detection assay that we previously established.[31] Briefly, we seeded NPCs onto black-wall, clear-bottom 96-well plates (SCREENSTAR, Greiner) pre-coated with Geltrex (Thermo Fisher Scientific) at a density of 1.5×10^5 cells/cm^2, and incubated them in NPC medium overnight at 37 °C, 5 % CO_2. The next day, NPCs were treated with either dimethylsulfoxide (DMSO) or sildenafil dilution series in 100 μl and incubated for 16 h at 37°C, 5% CO_2. On the day of the assay, we live-stained NPCs with 10 nM tetramethylrhodamine methyl ester (TMRM) (Invitrogen) and 1 μg/μl Hoechst 33342 (Thermo Fisher Scientific) in NPC medium for 30 min at 37 °C and 5 % CO_2. After 30 min incubation, cells were washed with 100 μl NPC medium without phenol red. NPCs were kept in 100 μl medium (w/o phenol red) for the duration of the assay. For confirming MMP depolarizing effect, we used the mitochondrial uncoupler carbonyl cyanide-p-trifluoromethoxyphenylhydrazone (FCCP) in combination with the mitochondrial complex III inhibitor antimycin A (AA).[31] Imaging was performed with an Operetta CLS high content imaging system (Revvity) with 20 x water objective in confocal mode. Imaging time did not exceed 30 min. TMRM and Hoechst 33342 intensity within the cells was calculated using Columbus software (Revvity, version 2.9.0). To assess the effect of KT5823 on MMP in presence and absence of sildenafil, NPCs were seeded, incubated as described above, and pre-treated for 1 h with either DMSO alone or 1 μM KT5823 dissolved in DMSO. After the incubation time, 10 μM sildenafil dissolved in DMSO was added on top and incubated for 16 h at 37°C, 5% CO_2. The final DMSO concentration was adjusted to 0.3 % for each condition. On the day of the assay, NPCs were live-stained and imaged. TMRM and Hoechst 33342 intensity within the cells was analyzed with CellProfiler (version 4.2.5). MMP values are presented as the TMRM intensity in a mutant or treated sample over the TMRM intensity in the control sample (%).

For MMP assessment using cytofluorimetry, we used LSR-Fortessa X-20 (Becton Dickinson) to monitor the fluorescence of TMRM (Invitrogen) following treatment with either 10 μM sildenafil, 10 μM 8-Br-cGMP (Sigma-Aldrich), or DMSO. Cells were harvested and resuspended in culture medium at approximately 1×10^6 cells/ml. The uncoupling agent carbonyl cyanide 3- chlorophenylhydrazone (CCCP, 50 μM final concentration) was added to the sample and incubated for 5 min at 37°C, 5% CO_2 to depolarize mitochondria. TMRM probe (20 nM final concentration) was added and incubated for 30 min at 37 °C and 5 % CO_2. After incubation, cells were washed once in 1 ml of culture medium, then resuspended in 300 μl of DPBS and analyzed on the flow cytometer. The TMRM-emitted fluorescence was detected by emission filters appropriate for R- phycoerythrin "PE" (585 nm ± 42 nm). An appropriate gating strategy was applied to select only live and single cells. Data were analyzed with FlowJo software (version 7.6); the median fluorescence intensity (MFI) for each sample was calculated and normalized on the relative unstained sample. TMRM intensity was quantified in at least 20,000 cells per sample; at least three biological replicates were analyzed. Statistical analysis was performed by one-way Anova. $p<0.05$ was considered statistically significant. MMP values are presented as the TMRM intensity in a mutant or treated sample over the TMRM intensity in the control sample (%).

For evaluating the MMP impact due to modulating BKCa channel, on day one, WT cells and BKCa KO cells were plated at a concentration to reach a 60 % confluence on day three. On day two, the cells were treated with 10 μM sildenafil or DMSO for 16 h. On day three, the cells were stained for 30 min at 37 °C with a staining solution containing HBSS 1 x (Gibco), 7 nM TMRM, 2 μM cyclosporin H, and 1:2,500 Hoechst. During the acquisition of the TMRM signal using the Operetta HTS system (PerkinElmer), cells were kept at 37 °C with 5 % CO_2 inside Operetta with the imaging solution containing HBSS 1 x (Gibco), 5 nM TMRM and 2 μM cyclosporin H. Measurement was performed for 111 minutes. Basal respiration was assessed by obtaining the mean TMRM values of the first 3 measurements. Values were then expressed as percentage of basal respiration. After 25 min, we injected either DMSO or oligomycin (2 μM), and the signal was recorded for further 50 min (4 measuring time points). Finally, FCCP (1 μM) was added to dissipate the membrane potential. The signal remaining following FCCP addition (two measuring points) was subtracted from TMRM signals of the basal and oligomycin-treated cells.

Compound screening

LS NPCs (ATP6_2) were seeded at a density of 1.5 x 10^5 cells/cm^2 onto Geltrex-coated 384-well black-wall, clear-bottom plates (Revvity) in 30 µl NPC medium using a Multidrop liquid dispenser (Thermo Fisher Scientific), which was calibrated prior to each usage. Using the MMP effect of FCCP in combination AA,[31] we established the Z' factor[38] of our assay to be about 0.68 - 0.85 across all screening plates. Assay plates with cells were placed into a rotating incubator (Thermo Electron, Cytomat) at 37 °C and 5 % CO_2 for 24 h. Cells were treated with 5 µM (0.05 % DMSO) of 5,632 different compounds from a drug repurposing library.[37] Compounds were transferred to 384-well assay plates using an Echo 550 (Beckman Coulter (Labcyte). Columns 23 and 24 contained controls on each plate. In row 23, a combination of 5 µM FCCP (Biozol) and antimycin A (Sigma Aldrich/Merck) was used as positive control to achieve complete mitochondrial depolarization. Row 24 contained 0.05 % DMSO as negative control. After incubation of 16 h, cells were live-stained for 30 min at 37 °C and 5 % CO_2 with a final concentration of 10 nM TMRM and 1 µg/µl Hoechst in 30 µl/well. Cells were then automated washed twice with 30 µl NPC medium (w/o phenol red) using the Janus MDT (Revvity). Images were directly acquired using an Operetta CLS high content imaging system with 20 x objective in confocal mode. Imaging time did not exceed 30 min. TMRM intensity within the cells and nuclei count was calculated using a customized Columbus software script and downstream data processing was performed with Activity Base (IDBS). 3 x DMSO standard deviation (SD) was set as the threshold for MMP depolarization to calculate and compare hit rates using different compound concentrations. To quantify the effects of compounds on depolarizing the hyperpolarized MMP of LS NPCs (ATP6_2), we normalized the percentage of MMP depolarization (TMRM signal) and the percentage of cell count (Hoechst signal) after treatment for 16 h with 5 µM of each compound in LS NPCs with respect to LS NPCs treated for 16 h with either 5 µM FCCP+AA or DMSO only. To achieve this normalization, we used the formula $z = (y - \min(x)) / (\max(x) - \min(x)) * 100$, where z is the final normalized value, y is the value of interest in the dataset, min(x) is the mean value of DMSO-treated LS NPCs, and max(x) is the mean value of FCCP+AA-treated LS NPCs. We next scored the normalized values (z) based on their ability to depolarize the MMP (inhibition) and classified the compounds in mild, intermediate, and strong uncouplers.

Bioenergetic assessment

For biochemical activity of complex V, approximately 1 x 10^7 NPCs were suspended in 0.5 ml of 10 mM ice-cold hypotonic Tris buffer (pH 7.6) and homogenized with glass/glass Dounce homogenizer with a tight pestle by 10 strokes. 200 µl of 1.5 M sucrose was added and then samples were centrifuged at 600 g for 10 min at 4 °C. Supernatants were collected and centrifuge at 14,000 g for 10 min at 4 °C. Mitochondrial pellets were suspended in 0.2 ml of 10 mM ice-cold hypotonic Tris buffer (pH 7.6) and subjected to three freeze-thaw cycles. Protein concentration was quantified with the Bicinchoninic Acid (BCA) protein assay Kit (Thermo Fisher Scientific). Complex V activity (ATP hydrolysis) was measured at 340 nm cleared from oligomycin-insensitive ATPase activities as described[43] and normalized to citrate synthase activity.[135]

For ATP content analysis, NPCs were grown in NPC medium and then switched to DMEM glucose-free (Gibco) and Neurobasal A-Medium glucose-free (Gibco) 1:1 medium supplemented with 1 mM sodium pyruvate, 1 % B27, 0.5 % N2, 1 % Pen/Strep, 1 % L-glutamine and 0.01 % MycoZap Plus-CL with 5 mM galactose as a carbon source to measure OXPHOS-derived ATP content, and then treated with DMSO or 10 µM sildenafil for 16 h. Luminescence-based ATP levels were detected in cellular suspension (5 x 10^3 cells) with ViaLight™ Plus Kit (Lonza). ATP levels were determined by luminometry using Victor Multiple Plate Reader Spectrophotometer (Revvity). For normalization purposes, we employed the DNA quantification with CyQUANT Cell Proliferation Assay (Invitrogen). Results were then expressed as luminescence A.U. relative to control lines cultured in galactose.

For live-cell assessment of cellular bioenergetics, we employed Seahorse XF96 and XFe24 extracellular flux analyzer, as previously described.[25] Briefly, the day before the assay, 100,000 cells (for XF96) or 120,000 (for XFe24) were plated into each Matrigel-coated well of the XF96 well plates and incubated overnight at 37 °C with 5 % CO_2. On the day of the assay, the growth medium was removed and replaced with glucose-based unbuffered media. The cells were incubated at 37 °C for 60 min to allow media temperature and pH to reach equilibrium before starting the measurement of mitochondrial respiration (oxygen consumption rate, OCR). After baseline records, we subsequently injected oligomycin (1 µM), FCCP (1 µM), and rotenone/antimycin A (1 µM each). Normalization to DNA content in each well of the plate was performed using the CyQUANT Cell Proliferation Assay kit.

Quantification of NAD metabolites

Quantitative analyses of NAD^+, NADH, $NADP^+$, and NADPH were carried out as a service in NADMED laboratory (Helsinki, Finland) from same homogenates submitted for metabolomics analysis. We used four LS NPC lines (ATP6_2, ATP6_4, ATP6_5 and ATP6_7.) and four healthy control NPC lines (CTRL_1, CTRL_2, CTRL_3 and CTRL_4) either treated for 16 h with either 0.1 % of DMSO or with 10 µM sildenafil resuspended in 0.1 % DMSO. NPCs were washed on the plate with DPBS buffer to remove protein of the culture media followed by the addition of cold extraction solvent acetonitrile:methanol:MilliQ; 40:40:20 to quench cellular metabolism. Obtained sample homogenates were shipped on dry ice to the measurement facility. Before analysis the homogenates were equilibrated to room temperature and centrifuged at 20,000 x g for 10 min at 4 °C to remove proteins. Next, NAD^+, NADH, $NADP^+$, and NADPH were measured individually from every cell extract using modified cyclic enzymatic reactions with colorimetric detection. For normalization of the results, protein content was measured using the pellets obtained after centrifugation of the homogenate.

Quantification of mtDNA copy number

NPCs were switched to DMEM glucose-free (Gibco) and Neurobasal A-Medium glucose-free (Gibco) 1:1 medium supplemented with 1 mM sodium pyruvate, 1 % B27, 0.5 % N2, 1 % Pen/Strep, 1 % L-glutamine and 0.01 % MycoZap Plus-CL with low glucose (4.6 mM), and then treated with DMSO or 1 μM sildenafil for 16 h. Cells were grown to confluency in a 6-well plate format. Medium was aspirated and cells were washed twice with DPBS. Quickly, cells were scraped in 1 ml DPBS. Cell suspension was collected into a 1.5 ml tube and centrifuged at 8,000 x g for 5 min at 4 °C. Supernatant was aspirated. Cell pellets were frozen in liquid nitrogen and stored at -80 °C. gDNA was isolated using the NucleoSpin Tissue Kit (Macherery-Nagel). DNA concentration was measured with the NanoDrop 2000 and diluted to 50 ng/μl. qPCR was performed using the Power SYBR Green PCR Master Mix (Applied Biosystems) for the genes *MT-ND1* and *NDUVF1* in technical triplicates, including no-template control. Ct values were corrected based on the primer efficiency.[136] The mtDNA/gDNA ratio was calculated with the corrected CT values using the formula: (*MT-ND1*/*NDUFV1*) * 2.

Analysis of mitochondrial nanostructure

To examine the impact of sildenafil on the mitochondrial nanostructure, we immunolabeled LS NPCs (ATP6_2) and control NPCs (CTRL_1) treated with 1 μM sildenafil for 24 h for MIC60, a core protein of the mitochondrial contact site and cristae organizing system (MICOS). For immunolabelling of MIC60, cells were fixed with prewarmed (37 °C) 4 % formaldehyde in DPBS (137 mM NaCl, 2.68 mM KCl and 10 mM Na2HPO4, pH 7.4) for 5 min at RT. Fixed cells were extracted with 0.5 % (v/v) Triton X-100 in DPBS, blocked with 5 % (w/v) BSA in DPBS. Afterwards, cells were incubated with diluted primary antibodies against MIC60 (Abcam) in 5 % (w/v) BSA in DPBS for 1 h at RT. After washing with DPBS, the primary antibodies were detected with secondary goat anti-rabbit antibodies labelled with Abberior STAR RED (Abberior). After washing with DPBS, the cells were mounted in Mowiol with 0.1 % 1,4-Diazabicyclo[2.2.2]octan (DABCO). Confocal and stimulated emission depletion (STED) microscopy were performed using an INFINITY platform (Abberior Instruments). The objective was an UPLXAPO60xO, NA: 1.42, oil objective (Olympus). For STED super-resolution microscopy, Abberior STAR RED was excited at 640 nm and depleted with 775 nm. The fluorescence was collected between 650 nm and 720 nm. Images were recorded with a pixel size of 20 nm and a dwell time of 30 μs per pixel.

To detect structural differences between LS NPCs and control NPCs, we captured approximately 4,000 STED images and trained a neural network classifier on multiple biological replicates to distinguish control NPCs (P[healthy]-score = 1) from LS NPCs (P[healthy]-score = 0). A deep residual neuronal network (ResNet34) was trained with STED data of DMSO-treated LS NPCs (ATP6_2) and control NPCs (CTRL_1) in a supervised setting to distinguish between both conditions. For the training, STED images were percentile normalized and divided into 512 x 512 pixel-sized regions (patches). Every patch was assigned to the class ''healthy'' when it originated from control NPCs and to the class ''ill'' when it originated from LS NPCs. Using a mean intensity threshold, patches without a sufficient fluorescence signal were allocated to a third class (''low information''). The final training dataset consisted of equal numbers of patches from three different biological replicates and included in total 75,000 patches of the ''healthy, ''ill'' and ''low information'' classes in a 0.4:0.4:0.2 ratio. The performance throughout the trainings process was monitored with a validation set of 11,000 patches. For every patch, the model predicts logits values corresponding to the three classes, that are then transformed with softmax function to receive a per class probability. The per-class accuracy computed from a confusion matrix was used as mean validation metric after each epoch and as an indicator for the best checkpoint. The final evaluation of the neuronal network after the training was carried out with a test set of 140,000 patches with a 0.4:0.4:0.2 ratio. The trained model was used to assign a P[healthy] score from zero to one to single STED images. For each STED image with a size of 2,048 x 2,048 pixels, 49 partially overlapping patches of 512 x 512 pixels were extracted and evaluated with the model. Patches with insufficient fluorescence signal were assigned to the ''low information'' class and excluded from the evaluation. For the remaining patches a P[healthy]-score was predicted. The P[healthy]-score of the single patches were averaged to assign a P(healthy)-scores to each STED image of 2,048 x 2,048 pixels. STED images which had a proportion of ''low information'' patches above 90 % were excluded. After training, the classifier could reliably differentiate the two conditions on images that were not used for the training, indicating alterations of the MIC60 fluorescence signal in LS NPCs. To gain further insights, we reviewed a subset of images individually. Confocal microscopy revealed a tubular mitochondrial network in both NPC cultures, with no evident phenotypic alterations in LS NPCs. STED imaging showed a largely uniform distribution of MIC60 clusters along mitochondrial tubules in control NPCs, whereas in LS NPCs, MIC60 appeared to accumulate at the sides of mitochondrial tubules. To investigate this phenotype, we manually analyzed the MIC60 pattern across the mitochondrial tubules in approximately 300 images. A semi-automated MATLAB-based analysis was employed to assess the MIC60 distribution in LS NPCs (ATP6_2) and control NPCs (CTRL_1). After blinding, individual elongated mitochondria were manually analyzed. The mitochondrial centerline was determined by marking discrete points along the mid-axis, which were then fitted to a Bézier curve to approximate the mitochondrial central axis. The fluorescence intensity profile across the mitochondrial transverse axis was measured every 10 nm at a length of 600 nm with its center at the Bézier curve. The profiles were averaged for all selected isolated mitochondrial fragments in a single STED image. A homogeneous MIC60 distribution results in a fluorescence intensity profile with a broad plateau at the central maximum along the transversal mitochondrial axis. MIC60 accumulation at the outer edge of the mitochondria creates a central intensity dip. LS NPCs revealed a clear dip in the distribution of fluorescence intensity. The altered distribution of MIC60 was expressed as a center-to-maximum fluorescence intensity ratio across the transversal mitochondrial axis.

Bulk RNA sequencing

For bulk transcriptomics of NPCs, we used four *MT-ATP6* mutant NPC lines (ATP6_2, ATP6_4, ATP6_5 and ATP6_7.) and four healthy control NPC lines (CTRL_1, CTRL_2, CTRL_3 and CTRL_4) either treated for 16 h with 0.1 % of DMSO alone or with 10 μM sildenafil resuspended in 0.1 % DMSO. We used n=3 biological replicates per condition. Total RNA was isolated from pelleted NPCs using the NucleoSpin RNA Plus kit (Macherey Nagel) and eluted in 30 μl RNase-free H_2O. RNA concentration was measured with NanoDrop 2000. For quality check, 300 ng RNA was run on a 2 % TBE gel.

For time-course bulk transcriptomics of NPCs grown in low glucose media, LS NPCs (ATP6_2, ATP6_4, and ATP6_7.) were switched to DMEM glucose-free (Gibco) and Neurobasal A-Medium glucose-free (Gibco) 1:1 medium supplemented with 1 mM sodium pyruvate, 1 % B27, 0.5 % N2, 1 % Pen/Strep, 1 % L-glutamine and 0.01 % MycoZap Plus-CL with low glucose (4.6 mM), and then treated for 6 or 24 h with 0.1 % DMSO alone, 1 μM sildenafil resuspended in 0.1 % DMSO, or 10 μM sildenafil resuspended in 0.1 % DMSO. We used n=3 biological replicates per condition. Total RNA was isolated from pelleted NPCs using the NucleoSpin RNA Plus kit (Macherey Nagel) and eluted in 30 μl RNase-free H_2O. RNA concentration was measured with NanoDrop 2000. For quality check, 300 ng RNA was run on a 2 %TBE gel. Differential expression analysis between the two timepoints was performed using DESeq2 (Wald test, Benjamini-Hochberg p-value adjustment). The values depicted in the boxplots (expression, y axis) in Figures S6E and S6F are variance-stabilized counts obtained with DESeq2's vst(), which normalized for sequencing depth and applies a transformation that is approximately log2 for large counts but reduces variance for low counts.

For bulk transcriptomics of brain organoids, total RNA was isolated from day 70 cortical brain organoids generated using the first protocol.[62,134] We used five pelleted organoids per sample with n=3 biological replicates per condition, grown under normal conditions (CTRL_1, CTRL_2, ATP6_4 and ATP6_7), or treated with 10 μM sildenafil for 24 h (ATP6_4 and ATP6_7). Total RNA was isolated using the RNeasy Mini Kit by Qiagen. RNA concentration as well as purity was measured at the Nanodrop Spectrophotometer ND1000 (peQlab) using ND-1000 software (V3.8.1). Total RNA was mixed with 1 μg of a DNA oligonucleotide pool comprising 50-nt long oligonucleotide mix covering the reverse complement of the entire length of each rRNA (28S rRNA, 18S rRNA, 16S rRNA, 5.8S rRNA, 5S rRNA, 12S rRNA), incubated with 1U of RNase H (Hybridase Thermostable RNase H, Epicentre), purified using RNA Cleanup XP beads (Agencourt), DNase treated using TURBO DNase rigorous treatment protocol (Thermo Fisher Scientific) and purified again with RNA Cleanup XP beads. rRNA-depleted RNA samples were further fragmented and processed into strand-specific cDNA libraries using TruSeq Stranded Total LT Sample Prep Kit (Illumina) and sequenced using the NovaSeq 6000 system with stranded technology, generating paired-end reads of 150 bp. Raw RNA sequencing data were processed to generate FASTQ files using Illumina bcl2fastq. Briefly, base calling was performed using Real-Time Analysis (RTA) software, and adapter sequences were trimmed. The resulting BCL files were converted to FASTQ format, followed by quality control assessment using FastQC before downstream analysis. The preprocessing of the FASTQ raw sequencing files was performed with nfcore/rnaseq (version 3.12.0) pipeline. Briefly, reads were trimmed with Trim Galore! (version 0.6.10) and mapped to the human genome (GRCh38 assembly) using STAR (version 2.7.10a) aligner.

For both NPCs and brain organoids samples, we performed different comparisons: i) LS with DMSO vs. controls with DMSO (disease signature), ii) LS + sildenafil vs. LS + DMSO (sildenafil signature), iii) controls + sildenafil vs. controls + DMSO (negative control test). Transcript counts were determined using Salmon (version 1.10.1). DESeq2 (version 1.40.2)[137] was used to identify differentially expressed genes in the NPC samples or in brain organoid samples (Table S1) (Benjamini-Hochberg-adjusted p-value 0.05). Gene Ontology (GO) enrichment analysis was performed to identify biological processes (BP) and cellular components (CC) using the enrichGO function within ClusterProfiler (4.8.3), using the annotations of org.Hs.eg.db (version 3.18.0). Visualizations were generated with ggplot2 (version 3.5.1).

Single-nucleus RNA sequencing

For single-nucleus RNA sequencing (snRNAseq), we used day 72 brain organoids generated with the second protocol[138] from control iPSCs (CTRL1) and LS iPSCs (ATP6_7). Brain organoids were treated with either DMSO or 10 μM sildenafil resuspended in DMSO for 45 days from day 27 to day 72. We used 15 pelleted organoids per sample (n=8 samples) with n=2 biological replicates per condition (n=120 cortical brain organoids in total). snRNA-seq was performed using the 10X Genomics Chromium system, following the manufacturer's protocol. Nuclei were isolated using mechanical dissociation with gradient centrifugation and stained with DAPI to assess nuclear integrity. Barcoding and cDNA amplification were carried out using the Chromium Single Cell 3' (vNext) Reagent Kit. Libraries were prepared and sequenced on the Illumina NovaSeq 6000, generating paired-end reads of 100 bp. Data processing, including demultiplexing, alignment to the reference genome (GRCh38-2020-A), and gene quantification, was performed using Cell Ranger (v7.2.0) from 10x Genomics with default parameters. To generate digital gene expression (DGE) matrices for each sample. DGEs were further processed in R (v. 4.4.1) using Seurat (v. 5.1.0).[139] Filtered DGEs were imported using the function "Read10x" and only genes detected in at least 5 cells were kept for downstream analyses. Similarly, cells with less than 200 genes and 3,000 unique transcripts or more than 0.5 % mitochondrial transcripts were discarded. After merging all samples in a single Seurat object, we performed gene expression normalization and scaling for each sample independently using SCTransform.[140] We performed unbiased clustering and dimensionality reduction using the first 20 principal components on all samples together. Clusters were manually annotated in 7 cell types analyzing their marker genes (Table S1). To identify differential genes induced by *MT-ATP6* variants and sildenafil treatment in a robust and reproducible way, we performed a pseudo-bulk analysis using the DESeq2 package[140] (v. 7.5.1), as described previously.[141] Pseudo-bulk analysis was used to determine differentially expressed genes within the individual populations (Table S1). For each population, we generated a pseudo-bulk expression profile for each organoid by summing the expression of 250 randomly selected cells. We filtered genes with less than 50 counts in at least 2 samples, normalized expression values by library size, estimated negative binomial dispersions. We performed different comparisons: i) LS + DMSO vs. controls + DMSO (disease signature), ii) LS + sildenafil vs. LS + DMSO (sildenafil signature), iii) controls + sildenafil vs. controls + DMSO (negative control test). For all comparisons, we identified differentially expressed genes and adjusted p value was calculated using Bonferroni correction for multiple testing correction. To estimate glycolytic pathway activity in single cells, we leveraged the AUCell package (v. 1.26.0)[142] and the 'Glycolysis' gene set in the 'Hallmark' database accessed from the MsigDB package (v 7.5.1).[143] Plots were generated with ggplot2 (v. 3.5.1) and piping using dplyr (v. 1.1.4) and visualized with uniform manifold approximation and projection (UMAP).

Proteomics analysis

We carried out proteomics using mass spectrometry (MS) for four *MT-ATP6* mutant NPC lines (ATP6_2, ATP6_4, ATP6_5, and ATP6_7) and four healthy control NPC lines (CTRL_1, CTRL_2, CTRL_3, and CTRL_4) with n=3 biological replicates per condition that were treated with either DMSO or 10 μM sildenafil in DMSO for 16 h. Cells were washed three times with ice-cold DPBS, detached using a cell scraper, transferred to pre-chilled 1.5 ml tubes and centrifuged at 1,000-3,000 rpm for 10 min at 4 °C. Subsequently, the supernatant was removed, and intact cells were snap-frozen. Cells were lysed under denaturing conditions in 300 μl of a buffer containing 3 M guanidinium chloride (GdmCl), 10 mM Tris(2-carboxyethyl)phosphine (TCEP), 40 mM chloroacetamide, and 100 mM Tris-HCl pH 8.5. Lysates were denatured at 95 °C for 10 min shaking at 1,000 rpm in a thermal shaker and sonicated in a water bath for 10 min. The protein concentration of each sample was measured with a BCA protein assay kit (23252, Thermo Fisher Scientific). 500 ng protein was used per sample and diluted with a dilution buffer containing 10 % acetonitrile and 25 mM Tris-HCl, pH 8.0, to reach a 1 M GdmCl concentration. Then, proteins were digested with LysC (Roche; enzyme to protein ratio 1:50, MS-grade) shaking at 800 rpm at 37 °C for 3.5 hours. The digestion mixture was diluted again with the same dilution buffer to reach 0.5 M GdmCl, followed by tryptic digestion (Roche, enzyme to protein ratio 1:50, MS-grade) and incubation at 37 °C overnight in a thermal shaker at 800 rpm. Peptides were acidified with formic acid to a final concentration of 2 %. LC-MS/MS was performed by nanoflow reversed-phase liquid chromatography (Dionex Ultimate 3000, Thermo Fisher Scientific) coupled online to a timsTOF SCP mass spectrometer (Bruker Daltonics) using the data-independent acquisition (DIA) method with parallel accumulation serial fragmentation (PASEF). Briefly, LC separation was performed using the Aurora Ultimate column (25 cm x 75 μm ID, C18, 1.7 μm beads, IonOpticks, Victoria, Australia). 150 ng of each desalted digest was applied to the column and peptides were eluted using a gradient of 3.8 to 38 % solvent B in solvent A over 60 min (total run time) at a flow rate of 400 nl per minute. Solvent A was 0.1 % formic acid and solvent B was 79.9 % acetonitrile, 20 % H_2O, and 0.1% formic acid. The "match between run" feature was used and the mass search range was set to m/z 400 to 1,000. MS data were processed with Dia-NN (v1.8.1) and searched against an in silico predicted human spectral library (Table S1).

Targeted metabolomics profiling

We carried out metabolomics using MS of four *MT-ATP6* mutant NPC lines (ATP6_2, ATP6_4, ATP6_5 and ATP6_7) and four healthy control N PC lines (CTRL_1, CTRL_2, CTRL_3 and CTRL_4) using n=4 replicates per condition that were treated with either 0.1 % DMSO or 10 μM sildenafil in 0.1 % DMSO for 16 h. NPCs were washed 1 x with DPBS, detached in 600 μl ice-cold extraction buffer (methanol, acetonitrile and Milli-Q water at a ratio of 40:40:20) using a cell scraper, transferred into an ice-cold 1.5 ml tube, and stored at -80 °C until use. Metabolites were extracted from cells with 500 μl of cold extraction solvent (Acetonitrile:Methanol:MilliQ; 40:40:20, Thermo Fischer Scientific). Subsequently, samples were processed with three cycles of sonication (60 s) and vortexing (120 s) followed by centrifugation at 14,000 rpm at 4 °C for 5 min. Next, the samples were centrifuged, the supernatants transferred to evaporation tube and evaporated to dry under nitrogen stream. Samples were reconstituted in 40 μl extraction buffer (Acetonitrile:Methanol:MilliQ; 40:40:20) and transferred to LC-MS vials. 2 μl of the samples were analyzed with Thermo Vanquish UHPLC coupled with Q-Exactive Orbitrap mass spectrometer equipped with a heated electrospray ionization (H-ESI) source probe (Thermo Fischer Scientific). A SeQuant ZIC-pHILIC (2.1 × 100 mm, 5 μm particle) column (Merck) was used for chromatographic separation. The gradient elution was carried out with a flow rate of 0.1 ml/min and mobile phase gradient with 20 mM ammonium hydrogen carbonate, adjusted to pH 9.4 with ammonium solution (25 %) as mobile phase A and acetonitrile as mobile phase B, 0-2 min 80 % B, 2-17 min 80-20 % B, 17-24 min 80 % B. The column oven and auto-sampler temperatures were set to 40 ± 3 °C and 5 ± 3 °C, respectively. Following setting were used for MS: full scan range: 55-825 m/z, polarity switching; resolution of 35,000, the spray voltages: 4250 V for positive and 3250 V for negative mode; the sheath gas: 25 arbitrary units (AU); the auxiliary gas: 15 AU; sweep gas flow 0; capillary temperature: 275 °C; S-lens RF level: 50.0. Instrument control was operated with the Xcalibur software (Thermo Fischer Scientific). The metabolite annotation and integration were done with the TraceFinder 5.1 software (Thermo Fischer Scientific) using confirmed retention times by in-house standard library (MSMLS-1EA, Merck) and their m/z. The data quality was monitored throughout the run using pooled QC sample prepared by pooling 5 μL from each suspended sample and interspersed throughout the run every 10 samples. The data was quality controlled for peak quality (poor chromatography), prefiltered with 20 % RSD cutoff of the pooled QC and noise. We identified metabolites that were differentially present within samples (Table S1).

Multi-omics integration

We performed multi-omics integration as previously described.[55] Briefly, we integrated bulk transcriptomics, proteomics, and metabolomics datasets derived from LS NPCs and control NPCs (*disease signature*), as well as transcriptomics and metabolomics datasets from sildenafil-treated LS NPCs and untreated LS NPCs (*sildenafil signature*). For both cases, we used all significantly deregulated molecules (adjusted p-value ≤ 0.05) as input lists for the OmicsNet platform (v.2.0) and retrieved their interactions based on STRING (confidence score 0.7) and Recon3D databases. Molecular interactions were filtered with the Prize-Collecting Steiner Forest (PCSF) algorithm, retaining only the most informative nodes regarding network organization and functionality. The final network was analyzed for centrality measures using the CytoNCA plugin in Cytoscape (v.3.10.2) and enrichment analysis using the KEGG database (Release 112.0). For network visualization, we chose the Organic Layout from yFiles plugin in Cytoscape. To dissect the rescue mechanism of sildenafil, we searched for molecules with reversed expression in the disease signature and sildenafil signature datasets. Molecules were annotated in the REACTOME and GeneOntology databases for pathway and biological processes enrichment analyses, respectively, using the clusterProfiler package (v4.10.0).

To explore the regulatory effect of sildenafil in gene expression levels, we retrieved the drug's signatures from the L1000 FWD database. Genes that had a consistent pattern of re-regulation across all examined cell lines after sildenafil treatment were considered as literature-indicated drug targets. We evaluated these literature-indicated drug targets in our transcriptomics datasets by filtering those genes that had the same pattern of re-regulation in LS NPCs after sildenafil administration (LS + sildenafil vs. LS + DMSO). A final list of literature-indicated drug targets with a similar regulation pattern in treated LS NPCs was considered a cross-validated set of genes involved in the mechanism of action of sildenafil. To describe the mechanistic effect of sildenafil on *HOXA5*, we performed two parallel clustering analyses in LS + DMSO vs. controls + DMSO and in LS + sildenafil vs. LS + DMSO networks, respectively. Specifically, we implemented the GLay algorithm aiming to identify the densely connected clusters within each network. By isolating the clusters with *HOXA5* and comparing them using the Dynet plug-in in Cytoscape, we highlighted their common and/or condition-specific interactions. Each cluster's interactions were used as inputs for enrichment analysis of biological pathways and terms. Following this pipeline, we identified the modulated pathways of *HOXA5* due to sildenafil administration.

Calcium imaging in cortical brain organoid slices (cBOS)

cBOS were generated as previously described.[69,144] Briefly, 3 % low melting temperature agarose (Gibco) was diluted in Hank's Balanced Salt Solution (HBSS, Sigma-Aldrich), heated to 90 °C and slowly cooled down to 40 °C. Brain organoids were washed in HBSS, embedded in the agarose, and cooled on ice until the agarose was solid. For slicing, a Vibratome Microm HM 650 V (Thermo Fisher Scientific) was adjusted to the following settings: frequency of 60 Hz, amplitude of 1.0 mm, velocity of 33 mm/s, and slice thickness of 300 μm. The slices were directly transferred to a petri dish filled with HBSS, placed in a cell culture hood and washed four times. Finally, the slices were collected on Millicell-CM inserts (Millipore) and placed in a 6-well plate. 750 μl of cortical differentiation medium IV (CDMIV) were added in each well, so that the membrane was soaked but the top side of the slices was still exposed to air. cBOS were cultured at 36 °C and 5 % CO_2 for around 30-59 days before starting calcium imaging experiments.

For calcium imaging experiments,[69] membrane permeable Oregon Green 488 BAPTA-1 AM (OGB-1, Invitrogen) was first solved in 20 % pluronic and 80 % DMSO and diluted to 200 μM in HEPES-buffered saline, which was then injected into cBOS and incubated for 30 minutes. During the incubation and throughout the experiments, cBOS were perfused with artificial cerebrospinal fluid (ACSF), containing 138 mM NaCl, 2.5 mM KCl, 2 mM $CaCl_2$, 1 mM $MgCl_2$, 1.25 mM NaH_2PO_4, 18 $NaHCO_3$, and 10 glucose. The ACSF was bubbled with 95 % O_2 and 5 % CO_2, resulting in a pH of 7.4. OGB-1 was excited at 488 nm and signals were detected using the imaging software NIS-Elements and a variable scan digital imaging system (Nikon) attached to an upright microscope (Eclipse FN-1, Nikon). The microscope was equipped with a Fluor 40x/ 0.8 DIC M/N2 ∞ /0 WD 2.0 water immersion objective (Nikon) and an orca FLASH 4.0 LT camera (Hamamatsu Photonics). Images were routinely obtained at 1 Hz and emission was collected at >500 nm. Regions of interest (ROIs) representing cell somata were identified, and their signals were background-corrected. For calculating $\Delta F/F0$, the traces were normalized to their initial baseline (first 30 s of measurement). Additionally, the fluorescence signals were corrected for bleaching and analysed with OriginPro Software (OriginLab Corporation). To probe for the cellular response to acute metabolic stress, ACSF was switched to glucose-free ACSF containing 5 mM sodium azide (Honeywell) and 2 mM 2-Deoxy-D-glucose (Apollo Scientific) for 2 min. Then, it was switched back to ACSF for 20-30 min until cellular calcium levels recovered to their original baseline. For each calcium signal, the area under the curve (AUC) and the peak amplitudes $\Delta F/F0$ (in %) were analyzed.

Calcium imaging in NPCs

One day prior to imaging, LS NPCs (ATP6_2, ATP6_4, ATP6_5, ATP6_7) were seeded on FluoroDishes™ at a density of 1.5 million cells/dish and treated with either 10 μM sildenafil or DMSO for 16 h. On the day of recording, the cells were washed twice with Tyrode's solution (129 mM NaCl, 2 mM CaCl2, 1 mM MgCl2, 5 mM KCl, 30 mM D-glucose, 25 mM HEPES, pH 7.4) and incubated with 3 μM fura-2 acetoxymethyl ester (fura-2 AM) (Thermo Fischer Scientific) in Tyrode's solution with 0.01% (v/v) Pluronic F-127 (Sigma-Aldrich) for 20 min at RT in the dark. After washing with Tyrode's solution, the cells were incubated for 10 min at room temperature (RT) in Tyrode's solution to allow fura-2 de-esterification and equilibration. Next, the Tyrode's solution was replaced by a calcium-free Tyrode's solution (129 mM NaCl, 1 mM MgCl2, 5 mM KCl, 30 mM D-glucose, 25 mM HEPES, 0.5 mM EGTA, pH 7.4), and immediately placed in a temperature- and CO_2-controlled (37 °C, 5 % CO_2, and ~20 % O_2) sample holder attached to the stage of an Axio Observer 7 inverted microscope (Zeiss, Jena, Germany) equipped with a x 40 objective (F-Fluar M27; NA 1.3; oil immersion; Zeiss) and x 1 magnification changer (Tubelens Optovar; Zeiss). Fura-2 was alternatingly excited at 340 nm and 380 nm using a Sutter Lambda DG5 wavelength switcher (Sutter Instruments, Novato, CA, USA), FT 430 dichroic mirror, and BP525/50 emission filter. Fura-2 emission signals were captured in the dark using an Axiocam 702 camera (Zeiss), applying an exposure time of 20 ms and image acquisition interval of 1 s. Microscopy hardware was controlled by Zen Pro software (version 3.2; Zeiss). During time lapse recordings, 1 μM thapsigargin (TG) (Thermo Fisher Scientific) was added to the extracellular medium by gentle pipetting. To achieve instantaneous mixing and a final concentration of 1 μM, 500 μl TG (prepared at 2 μM in calcium-free Tyrode's solution) was added to the FluoroDish™ containing 500 μl calcium-free Tyrode's solution. Numerical fluorescence intensity data was extracted from the fura-2 images using FIJI software (version 1.53q; https://fiji.sc/). ROIs were manually defined for each time lapse recording in the cytosol of individual cells and extracellular background. Next, in each image fura-2 emission signals were quantified for multiple cells at both excitation wavelengths. All cytosolic ROIs were of identical size and remained inside the cytosol during the full duration of the recording. Cytosolic fura-2 signals were first individually background-corrected for each excitation wavelength, after which the ratio value (340/380 nm) was calculated.

Neurite outgrowth quantification

We quantified neuronal outgrowth capacity in neurons treated for 8 days with 10 μM sildenafil or DMSO using our HCA-based protocol.[81] Briefly, neurons were split with 500 μl of Accutase at 37 °C for 10-15 min and were centrifuged for 5 min at 120 x g. All pipetting steps to dissociate the cells were performed slowly and gently to minimize damage to the more sensitive neurons. 10 μM ROCK inhibitor was added to the final media after splitting to promote neuron survival. Experiments and quantification were performed as previously described.[81] Neurons generated for neurite outgrowth quantification were treated with 10 μM sildenafil in 0.1 % DMSO or 0.1 % DMSO alone following media changes on days 8, 10, and 12. On day 14, the neurons were split and seeded onto black-wall, flat-clear-bottom 96-well plates (Greiner) at a density of 5,000 cells/well, and treated once more with Sildenafil or DMSO. Neurons were then cultured until day 16, when they were fixed with PFA, blocked, and stained for TUJ1 and Hoechst. Neurite images were then acquired using the Operetta CLS high content imaging system (Revvity) the TUJ1 and Hoechst signals at 20 x. Following acquisition, the neurite images were analyzed using CellProfiler (version 4.2.5). Briefly, the Hoechst signal was used to identify the nucleus as a primary object and the TUJ1 signal was used to identify the neurites as secondary objects. The nuclear objects were then expanded to serve as a proxy for the cell body and subtracted from the TUJ1 signal to leaving only the individual neurites. The results were exported as CSV for data analysis. Mean neurite length was calculated as the mean over the median per experiment.

For *PRKG1* knock-down (KD) in dopaminergic-enriched neuronal cultures, we used small interfering RNA (siRNA) against *PRKG1* using jetPRIME transfection (Polyplus) following the manufacturer's instruction. On day 12, neurons were transfected with 10 nM of *PRKG1* siRNA (Ambion) or scrambled siRNA (Ambion) by adding the transfection mix directly to the well. On day 14, after re-seeding the neurons onto the 96-well plates, neurons were transfected again with 10 nM of *PRKG1* siRNA or scramble siRNA. On day 16, *PRKG1* knock-down efficiency was evaluated by qPCR and neurite length was quantified with our HCA protocol.[81]

Experiments with *Ndufs4* KO mice

Sildenafil citrate (Sigma-Aldrich) was dissolved in DMSO, then diluted with tap water to obtain the final concentration of 400 mg/l drinking water and given *ad libitum*. Untreated mice (10 females, 8 males) were compared to sildenafil-treated *Ndufs4* KO mice (6 females, 6 males). Electrocardiography (ECG) recordings were recorded from conscious mice, using the INDUS Rodent Surgical Monitoring system without anesthesia. Transthoracic echocardiograms to measure ventricular size, wall thickness, and ejection fraction were performed on mice using the Vevo 2,700 VisualSonics System. Intraperitoneal injection with 0.1 mg midazolam was applied for anxiolytic muscle relaxant effects, without any anesthetic agent that may cause cardiac suppression. Standard 2D, M-mode, Doppler, Tissue Doppler images were obtained using a 30-MHz linear array transducer, including the parasternal short and long axis. All image analysis was performed by Vevo 2,100 analysis software (v.1.5) after rapid image collection. The diastolic function was measured using tissue Doppler imaging of the mitral annulus (E') and conventional mitral inflow (E wave). Metabolic chamber by Promethion (Sable Systems International) was applied to characterize the metabolism of whole-animal energy expenditure.[145] The 16-cage metabolic chamber system directly measures various parameters over a 72-hour period, such as heat production, oxygen consumption (VO_2), CO_2 production, and XY activity movement. The respiratory exchange ratio (RER) is calculated as the ratio of carbon dioxide production (VCO_2) to oxygen consumption. This parameter is useful to estimate the metabolic status. The xy axis detection of animal motion measure activity during day-time and night-time. The formula applied was Heat = $(1.232{*}VCO_2)+(3.815{*}VO_2)$.

Experiments with *SURF1* KO pigs

For generation of *SURF1* KO pigs, we followed a protocol for somatic cell nuclear transfer (SCNT) based on our previous method[11] with minor modifications. Briefly, ovaries from pubertal gilts of domestic pig, large white background were collected at a local abattoir and transported to the lab at 31-33 °C. Follicles larger than 3 mm were aspirated, and cumulus-oocyte complexes (COCs) were selected and matured in vitro at 38.5 °C under 5 % CO_2 for 42 h. One day before SCNT, donor cells were induced into quiescence via serum starvation (0.5 % FCS). On the day of SCNT, cells were trypsinized, washed, and resuspended in SOF-Hepes medium. Matured oocytes (with extruded polar body) were selected and zona pellucida was removed using 0.5 % pronase in DPBS. All manipulations were performed in SOF-Hepes with 10 % FCS. Oocytes were enucleated after a 5-min treatment with cytochalasin B (7.5 μg/ml) and Hoechst 33342 (5 μg/ml). Enucleated cytoplasts were exposed to phytohemagglutinin and fused with donor cells via double DC-pulse (1.2 kV/cm), then returned to maturation medium. As nuclear donor, we used a cell clone obtained by homologous direct recombination (HDR)[11] that harbors a 106 bp deletion on the left homology arm of exon 3 as well as a puromycin-resistance cassette in both alleles of the *SURF1* gene. After ~48 h of maturation, embryos were activated with a second double DC-pulse and incubated for 2 h in maturation medium containing cytochalasin B (5 μg/ml) and cycloheximide (10 μg/ml). Embryos were cultured in modified mSOF medium with amino acids and 4 mg/ml BSA, using a modified Well-of-the-Well system. Sows were synchronized with 12 mg/day of altrenogest for 15 days. On day 13, they received 0.15 mg $PgF_2\alpha$, followed by 1000 IU hCG 96 h after the last altrenogest dose. On day 6 of SCNT embryo development (compacted morula to early blastocyst stage), embryos were surgically transferred via mid-ventral laparotomy, five days after standing estrus. Pregnancy was assessed via ultrasound on day 30 and confirmed on day 60 post-transfer. Farrowing was induced with $PgF_2\alpha$ on days 114-115 of gestation. All offspring were genotyped after birth. For body temperature detection we used a Thermal Imaging Camera (Dongguan Xintai Instrument Co., Ltd, China).

SURF1 KO male piglets were treated immediately after birth with sildenafil citrate (n=3 animals with 2.1 mg/kg/day, n=4 animals with 0.5 mg/kg/day). At birth, the animals were separated from the sow and transferred to an incubator kept at 35 °C. Sildenafil was always administered at the same time and dissolved in milk. The veterinarian ensured that the entire dose was consumed. For biochemical and immunoblot experiments, we isolated the basal ganglia of newborn male pigs: 3 *SURF1* KO, 3 *SURF1* KO treated with sildenafil (2.1 mg/kg/day), and 3 sex and age-matched WT. Spectrophotometric analyses of complex IV (CIV) and citrate synthase (CS) activities were carried out as previously described.[135] CIV activity was normalized to CS activity, an index of mitochondrial mass. For histological analysis, tissues were removed immediately after death, post-fixed in 4 % PFA at 4 °C for 48 h, cryoprotected in DPBS containing 30 % sucrose for 24 h at 4 °C, embedded in optimal cutting temperature (OCT) compound, and frozen on dry ice. Cryostat sections (10 μm thick) were then mounted on gelatin-coated glass slides. The sections were stained with hematoxylin and eosin (H&E). Images were acquired using a Nikon Eclipse E400 light microscope at 20 x or 40 x magnification.

Quantification of sildenafil concentration in patient plasma

The sildenafil plasma concentration was monitored in three treated LS patients. EDTA blood was drawn in the morning before the first dose (trough level) and one hour after oral sildenafil application (peak level). Depicted time points in Figure 6D were separated by more than 3 months for each patient. The quantification was performed by Liquid Chromatography-Tandem Mass Spectrometry (LC-MS/MS). The EDTA-blood sample was centrifuged at 3,000 x *g* for 10 min at 4 °C and the plasma was aliquoted and frozen at -80 °C until measurement. 100 μl sample was mixed with 400 μl of the internal standard d_3-sildenafil (10 nM in acetonitrile) (CDN Isotopes). Proteins were precipitated by vortexing for 1 min and subsequent storage for 60 min at -20 °C. Supernatants were obtained by centrifugation at 16,000 x *g* at 4 °C for 10 min and subjected to LC-MS/MS sildenafil quantification applying the multiple reaction monitoring (MRM) approach. Chromatographic separation was achieved on a 1290 Infinity II HPLC (Agilent Technologies) equipped with a Poroshell 120 EC-C18 column (3.0 x 150 mm, 2.7 μm; Agilent Technologies) guarded by a pre-column (3.0 x 5 mm, 2.7 μm) of identical material. Water (eluent A) and acetonitrile (eluent B), both acidified with 0.1 % formic acid, were pumped with 0.4 ml/min. Elution of sildenafil and its internal standard was achieved with a 10-min linear gradient from 5 % to 90 % eluent B. Total run-time was 17 min including re-equilibration of the LC system. MS/MS analyses were carried out using an Ultivo triple-quadrupole mass spectrometer (Agilent Technologies) operating in the positive electrospray ionization mode (ESI+). The following ion source parameters were set: sheath gas temperature, 400 °C; sheath gas flow, 12 l/min of nitrogen; nebulizer pressure, 20 psi; drying gas temperature, 100 °C; drying gas flow, 7 l/min of nitrogen; capillary voltage, 3.0 kV; nozzle voltage, 0 kV. The following mass transitions were recorded (fragmentor voltage [FV] and collision energies [CE] in parentheses): sildenafil: m/z 475.2 → 58.0 (FV: 220 V, CE: 68 eV, *quantifier*), m/z 475.2 → 100.0 (FV: 220 V, CE: 28 eV), m/z 475.2 → 283.1 (FV: 220 V, CE: 44 eV); d_3-sildenafil: m/z 478.2 → 60.9 (FV: 220 V, CE: 68 eV, *quantifier*), m/z 478.2 → 103.0 (FV: 220 V, CE: 28 eV), m/z 478.2 → 283.1 (FV: 220 V, CE: 44 eV). Peak areas were determined with MassHunter Software (Agilent Technologies) and sildenafil was directly quantified *via* its internal standard d_3-sildenafil that was concentrated to 8 nM in the samples.

Genotyping and heteroplasmy quantification

Heteroplasmy levels and mtDNA haplotypes in the whole exome sequencing (WES) datasets were determined using the software MToolBox v.1.[146,147] Results were visualized in the IGV viewer v2.16.[148] Heteroplasmy levels of the *MT-ATP6* mutations in fibroblasts, iPSCs, and NPCs were determined using polymerase chain reaction-restriction fragment length polymorphism (PCR-RFLP) analysis, as described before.[27] Genomic DNA was isolated using the Nucleo-Spin Tissue kit (Macherey-Nagel). We used restriction enzyme StuI (NEB, R0187, 10,000 units/ml) for the m.9185T>C mutation (wild-type: 24+90 pb, mutation: 114 pb), HpaII (NEB, R0171, 10,000 units/ml) for m.8993T>C and m.8993T>G (wild type: 25+155 bp; mutant: 180 bp), XbaI (NEB, R0145, 10,000 units/ml) for m.9176 T>G (wild type: 24+155 bp, mutant: 179 bp). The percentage of cleaved versus uncleaved fragments was determined by capillary electrophoresis and laser detection of the FAM-labelled RFLP-fragments using the 3,500 Series Genetic Analyzer (Applied Biosystems, RRID:SCR_021901) and normalized to a standard curve of known degrees of heteroplasmy.

Cranial magnetic resonance imaging (cMRI)

cMRI was performed for the six patients with LS carrying *MT-ATP6*. For Patient 1, imaging was carried out at 16.5 years of age and showed areas of increased T_2-signal intensity in the *Putamen* and *Nucleus caudatus* on both sides (Figure 6E) and at the perisylvian gray matter (Figure S12H). For patient 2, imaging was carried out at 2.2 years of age and showed lesional areas in the *Putamen* and *Nucleus caudatus* in both T_2-weighted images (Figure 6E) and Fluid Attenuated Inversion Recovery (FLAIR) images (Figure S12H). For patient 3, imaging was carried out at 5 years of age (Figure 6E) and at 14 years of age (Figure S12H). Areas with increased T_2-signal intensity at 5 years of age (Figure 6E) had spontaneously resolved at 14 years of age (Figure S12H). In patient 4, FLAIR imaging was performed at 35 years of age and areas of increased signal intensity at the *Nuclei caudati* on both sides (Figure 6E) and enlargement of the internal and external liquor spaces due to diffused brain atrophy (Figure S12H). For patient 5, imaging was performed at 4.5 months of age and showed T_2-weighted images delayed myelination, enlarged external cerebral spinal fluid spaces, and a general frontal brain atrophy (Figure 6E). The T_2-signal intensity in the brain stem of patient 5 affected the *Fasciculus longitudinalis* and the *Substantia nigra* (Figure S12H). For patient 6, imaging was performed at 7.5 years of age and showed areas of increased T_2-signal intensity in the *Putamen, Pallidum*, and *Nucleus caudatus* on both sides (Figure 6E) and in the cortical gray matter (Figure S12H).

Toxicity assays

CellTiter-Glo assay (Promega) was used to determine cell viability based on cellular ATP concentration. NPCs were isolated using Accutase and seeded onto Geltrex-coated 96-well plates at a density of 1.5 x 10^5 cells/cm^2 and incubated in NPC medium overnight at 37 °C and 5 % CO_2. The day after, NPCs were treated with DMSO, FCCP+AA or sildenafil dilution series in 100 µl and incubated for 16 h at 37 °C and 5 % CO_2. One column contained an untreated reference. 50 µl Cell Titer-Glo reagent solution was added to each well and placed on a plate shaker (1 min, 100 rpm) and incubated at ambient temperature for 10 min to ensure cell lysis. 100 µl of the solution was transferred onto a new white wall, white bottom 96-well plate, and luminescence was measured using an EnSight multimode plate reader (Revvity).

For proliferation, NPCs were seeded in a coated 96-well plate (30,000 cells/well) and incubated at 37 °C and 5 % CO_2. Medium glucose concentration was either 21 mM or 4.5 mM, or glucose was substituted with galactose. With the first medium change, the medium was supplemented with 1 µM sildenafil, 10 µM sildenafil or DMSO (vehicle), respectively, or left without treatment. For toxicity analysis, the medium was additionally supplemented with Incuyte dye red (Sartorius) to indicate dead cells. Supplemented medium was changed every other day. Over the course of the experiment, the well plates were placed in the Cellcyte X (Cytena) microscope with a 10 x objective. Four pictures of each well were taken every three hours. Pipeline setup and analysis were done with the software CELLCYTE Studio (Cytena). Channels were "enhanced contour" for confluency and "red channel" (600 ms, 9 dB) for toxicity. Autofocus was set to "Classifier-based". Pictures taken with the "enhanced contour" channel were analyzed with the software-specific protocol "Cell Confluence" with the following settings: 58 a.u. contrast sensitivity, 2 a.u. smoothing, 200 µm^2 filled hole size, 100 µm^2 min object size. Pictures taken with "red channel" were analyzed with the software-specific protocol "object count" with the following settings: 30 a.u. contrast sensitivity, 50 a.u. separation sensitivity, 0 µm^2 filled hole size, 10 µm^2 min object size. Analysis results were exported to Excel and further processed with R studio.

Immunostaining

We fixed NPCs and neurons grown on Matrigel-coated coverslips with 4 % PFA (Thermo Fisher Scientific) in DPBS for 20 min at RT and washed two times with DPBS. For permeabilization, we incubated the fixed cells with a blocking solution containing 10 % normal donkey serum (DNS) (Merck Millipore) and 1% Triton X-100 (Sigma-Aldrich) in DPBS with 0.05 % Tween 20 (Sigma-Aldrich) for 1 h at RT. We diluted primary antibodies in blocking solution and incubated them overnight at 4 °C on a shaker. Next, the primary antibody was removed, and the wells were rinsed three times with DPBS. Corresponding secondary antibodies (all Alexa Fluor, 1:2,000, Thermo Fisher Scientific) together with 1:2,500 Hoechst 33342 (Thermo Fisher Scientific) were diluted in blocking solution and added to the wells for 1 h at RT on a shaker. Finally, the staining solution was removed, and the wells were rinsed with DPBS three times following mounting of the coverslips on microscopic slides. We acquired the images of 2D cultures using the fluorescence microscope ZEISS Axio Observer Apotome 3 (Zeiss) in combination with the ZEN Microscopy Software (Zeiss) and further processed with ImageJ.

For staining cortical brain organoids, we used 4 % PFA (Thermo Fisher Scientific) in DPBS for 1 h at RT and sliced them using the Vibratome Microm HM 650 V (Thermo Fisher Scientific). The samples were placed in a 3 % LB agar (Sigma-Aldrich) solution in DPBS and put in a cool place until the agar was solidified. The agar shape was freed from its mould and attached on the carrier plate of the vibratome and placed in cold DPBS. The cutting procedure was performed at an amplitude of 1.0 mm, a frequency of 60 Hz and a velocity of 13 mm/s. The organoids were sliced with a thickness of 100 µm and gently transferred to SuperFrost Plus glass slides (VWR) for staining. Blocking was carried out for 1 h at RT with a blocking solution containing 1 x DPBS, 10 % donkey serum (Sigma-Aldrich), 0.1 % Tween-20 (Sigma-Aldrich), and 1 % Triton-X (Merck). Primary antibodies were dissolved in blocking solution and applied on the slides and incubated at 4 °C overnight. The next day, the slides were rinsed three times for 10 min in 1 x DPBS and then exposed to secondary antibodies in blocking solution at a dilution of 1:300 counterstained with 1:2,500 Hoechst 3342 (Invitrogen). The slides were incubated for 1 h at RT protected from light and subsequently rinsed three times for 10 min with 1 x DPBS. Finally, coverslips were mounted using Pro-Long Glass Antifade Mountant (Invitrogen) on microscopic slides. Images of brain organoids were acquired using the Eclipse 90i upright widefield microscope (Nikon Microscope solutions) equipped with the imaging software NIS-Elements Advanced Research 3.2 (Nikon). Large images (7 x 7 stitches) were taken with a dry 20 x objective (Plan Apo VC 20 x / 0.75 air DIC N2 ∞/0.17 WD 1.0, Nikon Microscope Solutions) and three different filter channels (DAPI, FITC, TRITC). Specific structures of interest within the slices were imaged with the Confocal laser scanning microscope C1 (Nikon Microscope Solutions) and a dry 20 x objective (Plan Apo VC 20 x / 0.75 air DIC N2 ∞/0.17 WD 1.0, Nikon Microscope Solutions). Images were taken using the imaging software EZ-C1 Silver Version 3.91 at z-stack settings (1.1 µm step size, 10-30 steps).

Primary antibodies used for NPCs and organoids include rabbit anti-PAX-6 (BioLegend, 1:200), mouse anti-ß-Tubullin III (TUJ1, Sigma-Aldrich, 1:2000), mouse anti-Nestin (Merck/Sigma-Aldrich, 1:200). Secondary antibodies used include donkey anti-rabbit 488 (Invitrogen, 1:300), donkey anti-rabbit 647 (Invitrogen, 1:1000) and donkey anti-mouse Cy3 (Sigma-Aldrich, 1:300).

Tight junction proteins within BCECs were detected and visualized via immunofluorescence staining. For each step, 50 µl solution/insert was used. BCECs were fixed using 4% formaldehyde in DPBS for 10 min. After washing three times with DPBS, fixated cells were incubated in permeabilization solution (0.1% Triton X-100 in DPBS) for 15 min, washed twice with DPBS for 5 min each and subsequently, unspecific binding sites were blocked by incubation for at least 30 min in blocking solution (3% BSA in DPBS, 0.1% Tween 20). Primary antibodies were diluted in blocking solution and were applied to the inserts and incubated overnight at 4°C. Unbound antibodies were removed by washing twice for 5 min with DPBS. Next, cells were incubated with secondary antibodies, diluted in blocking solution, for 1 h at room temperature in the dark. After two additional washing steps, nuclear counterstaining was performed with 1 µg/ml Hoechst 33258 in DPBS. Cells were again washed twice with DPBS. Afterwards, the insert membranes were carefully cut out of the holder with a scalpel and transferred to the centre of glass slides, with the cell side facing upwards. These were then covered with approximately 5 µl mounting medium and a cover glass, which was framed with transparent nail varnish after drying. Glass slides were imaged using the Operetta CLS High Content Imaging System. Primary antibodies used: Occludin (mouse, Invitrogen 1:200) and ZO-1 (TJP1, Proteintech rabbit 1:100). Corresponding secondary antibodies used: Donkey anti-rabbit Alexa Fluor 488 (1:500, Thermo Fisher Scientific) and Goat anti-mouse Alexa Fluor 633 (1:500, Thermo Fisher Scientific).

Immunoblot analysis

Pellets of NPCs (at least 1.5 x 10^6 NPCs) or brain pig tissue (globus pallidus in the basal ganglia) were homogenized in 10 volumes of ice-cold 1x RIPA buffer (150 mM NaCl, 5 mM EDTA pH 8, 50 mM Tris pH 8, 1 % NP-40, 0.5 % sodium deoxycholate, 0.1 % sodium dodecyl sulfate) supplemented with protease and phosphatase inhibitors. Samples were incubated on ice for 30 min, followed by centrifugation at 14,000 rpm for 30 min at 4 °C. After three freeze-thaw cycles, protein concentration in the supernatants was determined using the Bradford assay (Bio-Rad). For SDS-PAGE, 30 µg of total proteins per sample were loaded onto 4-12% gradient polyacrylamide gels. Proteins were transferred to nitrocellulose membranes, which were then blocked for 1 h at RT with 5 % non-fat dry milk (Bio-Rad) or 5 % BSA (Sigma-Aldrich) in TBST (TBS + 0.1% Tween-20). Membranes were incubated overnight at 4 °C with primary antibodies diluted in blocking buffer. The following day, HRP-conjugated secondary antibodies (Sigma- Aldrich) were applied for 1 h at RT. Protein bands were visualized using either Clarity Western ECL substrate or Clarity Max from Bio-Rad. Images were acquired with the Azure Biosystems Aerogene 300Q imaging system. Densitometric quantification was performed using ImageJ software. After background subtraction, band intensities were normalized to the corresponding loading control β-ACTIN. Primary antibodies used were against PRKG1 (1:1000, Cell Signaling), anti-β-ACTIN (1:1000, Abcam), p-mTOR-Ser2448 (1:1,000, Cell Signaling), p-AMPKa-2270 Thr174 (1:1,000, Cell Signaling), p-PGC1a-Ser571 (1:1,000, Biotechne), p-4EBP-1 (1:1,000, Cell Signaling), PGC1a (1:1,000, Novus Bio), AMPKa (1:1,000, Cell Signaling), 4EBP-12272 (1:1,000, Cell Signaling), mTOR (1:1,000, Cell Signaling), anti-GAPDH (1:1,000, Abcam).

For MT-ATP6 immunoblotting, pooled NPCs (at least 1.5 x 10^6 NPCs) were homogenized in RIPA buffer and sonicated in an ultrasonic bath (Branson 1800-E) for 1 min, incubated in ice for 30 min and then centrifuged at 10,000 x g for 15 min at 4 °C. Protein concentration was determined with the Bicinchoninic Acid (BCA) protein assay kit (Thermo Fisher Scientific). 30 µg of proteins were run through a 4 % separating / 10 % resolving polyacrylamide gel with stain-free technology (Bio-Rad laboratories), to allow detection and quantification. Proteins were then electroblotted onto a PVDF membrane. After 1 h of blocking with 3 % BSA in TBS-Tween at RT, the membranes were incubated with the primary antibodies overnight at 4 °C and subsequently probed with HRP-conjugated secondary antibodies for 2 h at RT. Chemiluminescence-based immunostaining (SuperSignal West Pico PLUS Chemiluminescent Substrate, Thermo Fisher Scientific) was performed. Images were acquired with the ChemiDoc MP Imaging system. Data analysis and quantification was performed using Image Lab software, 6.1 (Bio-Rad Laboratories). The following primary antibody was used ATP6 (rabbit, 1:500, Immunological Science), with the appropriate secondary antibodies: anti-rabbit, HRP Conjugate (1:5000, Promega)

Mitochondrial complex assembly

For preparation of mitochondrial-enriched fractions for Blue Native PAGE, approximately 2 x 10^7 cells were resuspended in 400 µl of ice-cold Medium A (0.32 M sucrose, 10 mM Tris-HCl pH 7.4, 1 mM EDTA), homogenized in a glass/glass dounce homogenizer with a tight pestle by 10 strokes and centrifuged at 800 x g for 5 min at 4 °C to remove cell debris. Supernatants were collected and centrifuged at 9,000 x g for 10 min at 4 °C to obtain the enriched mitochondrial fractions and resuspended in 50 µl of cold Medium A to quantify the protein yield by Bicinchoninic Acid (BCA) protein assay Kit (Thermo Fisher Scientific). Samples were centrifuged again, resuspended in 1.5 M aminocaproic acid, 50 mM Bis-Tris/HCl pH 7, to a final protein concentration of 5 µg/µl, and solubilized with 1.6 µg of n-Dodecyl β-D-maltoside (DDM) per µg of protein, incubated on ice for 10 min and centrifuged at 16,000 x g for 30 min at 4 °C. Supernatants were collected, supplemented with 5 µl of Sample Buffer (750 mM aminocaproic acid, 50 mM Bis-Tris/HCl pH 7, 0.5 mM EDTA, and 5 % Serva Blue G-250) and stored at -80 °C until use.

For Blue Native Gel Electrophoresis (1D-BNGE) and 2D SDS-PAGE, about 40 µg of solubilized mitochondria were separated by pre-cast NativePAGE 3-12 % BisTris gels (Invitrogen) and run in a Mini Gel Tank (Thermo Fisher Scientific) at 4 °C. The upper buffer chamber was filled with Dark Blue Cathode buffer (50 mM Tricine, 15 mM Bis-Tris pH 7, 0.02 % Serva Blue G-250), and the lower buffer chamber with Anode buffer (50 mM Bis-Tris pH 7). Samples were run at 100 V for 30 min, then at 200 V. Dark Blue Cathode buffer was replaced with Light Blue Cathode Buffer (50 mM Tricine, 15 mM Bis-Tris pH 7, 0.002 % Serva Blue G-250) at half run.

Samples were then electroblotted onto a PVDF membrane and blocked for 1 h (3 % BSA in TBS-Tween) at RT before proceeding with the immunodetection. In 1D-BNGE, the antibody against ATP5B was used to visualize complex V holoenzyme and intermediate subassemblies; complex III (detected with antibody against UQCRFS1) was shown as loading control. Denaturing 2D-BNGE was used to confirm the presence of different subassemblies of complex V. For complex V and complex III visualization, we used antibodies against ATP5B (1:1,000, Sigma-Aldrich) and UQCRSF1 (1:1,000, Abcam). For 2D-PAGE, the gel strips of the 1D-BNGE were excised and covered with a denaturing solution (1 % SDS, 1 % β- Mercaptoethanol) for 1 h at RT. Each gel strip was run through a 4 % stacking / 10 % resolving polyacrylamide gel electrophoresis (Bio-Rad), electroblotted onto a PVDF membrane, and blocked for 1 h at RT with 3 % BSA in TBS-Tween. The following antibodies were used: ATP5B (1:1,000, Sigma-Aldrich), NDUFA9 (1:1,000, Invitrogen), and SDH-B (1:800, Abcam).

Quantitative polymerase chain reaction (qPCR)

Isolated total RNA was transcribed into complementary DNA (cDNA). Into a nuclease-free microcentrifuge tube, 1 μl of oligo $d(T)_{18}$ primers (Thermo Fisher Scientific), 1 μl of 10 mM dNTP mix (Thermo Fisher Scientific) and the respective volume of RNA solution that contained 1 μg RNA were filled up to 12 μl with RNase-free, distilled water. In the Mastercycler X50s (Eppendorf), the mixture was heated to 65 °C for 5 min and then quickly chilled on ice. 4 μl of 5 x First-Strand Buffer, 2 μl of 0.1M DTT and 1 μl of RNaseOUT (Invitrogen) were added to the tube, gently mixed and incubated at 37 °C for 2 min. 1 μl (200 units) of Moloney Murine Leukemia Virus Reverse Transcriptase (M-MLV RT) was added to the reaction tube and mixed. The reaction mixture was incubated for 50 min at 37 °C, and inactivated by heating at 70 °C for 15 min. For the qPCR reaction, the synthesized cDNA was mixed with 10 μM primer mix (primers designed with Integrated DNA technologies, Table S5) and SYBR™ Green PCR Master Mix (Applied Biosystems) diluted in water in a 96-well plate. The plate was transferred to CFX96™ Real-Time System qPCR machine (Bio-Rad) and the following program was started using CFX96 software: 2 min at 50 °C, 10 min at 95 °C, 39 x (15 s at 95 °C, 30 s at 62 °C, 30 s at 72 °C), 15 min at 95 °C, 5 s at 62 °C, and 50 s at 95 °C. To check the quality of the qPCR products, melting curves were assessed first. The obtained CT values were analyzed using the $2^{-\Delta\Delta CT}$ method. For this, the CT values of the genes of interest were subtracted from the CT values of the housekeeping genes Glyceraldehyde-3-phosphate dehydrogenase (*GAPDH*) and/or ornithine decarboxylase antizyme 1 (*OAZ1*). To investigate the differentiation ratio of brain organoids, we used SOX2/CTIP2 ratio. For this, the qPCR method was applied to RNA samples from each five pooled day 70 cortical brain organoids (CTRL_1, CTRL_2, ATP6_4, ATP6_7) with or without 10 μM sildenafil treatment for 24 hours.

Human blood-brain barrier (BBB) model

Control iPSCs (CTRL_8) and LS iPSCs (ATP6_2) were differentiated into brain capillary endothelial cells (BCECs) following previously described protocols.[149,150] Single cells were isolated using Accutase (Thermo Fisher Scientific) and seeded onto Matrigel-coated 6-well plates (Nunc™, Thermo Fisher Scientific) in 2 ml/well mTeSR™ Plus supplemented with 10 μM Y-27632 (STEMCELL Technologies). The starting cell number was optimized for both cell lines respectively. After 3 days, medium was changed to 2 ml/well unconditioned medium (UM) when the optimal cell density of 2 - 4 x 10^5 cells/cm^2 was reached (referred to as day 0). UM was composed of 78.5 % DMEM/F12 (Thermo Fisher Scientific), 20 % KnockOut serum replacement (Thermo Fisher Scientific), 1% MEM NEAA (Thermo Fisher Scientific), 0.5 % L-glutamine (Capricorn), and 0.1 mM β-mercaptoethanol (Thermo Fisher Scientific). UM was changed daily for the following five days to initiate co-differentiation of BCECs and neuronal cells. On day 6, medium was changed to 4 ml/well endothelial cell (EC) medium, composed of Human Endothelial-SFM (Thermo Fisher Scientific) and 0.5 % B27 Supplement (Thermo Fisher Scientific), supplemented with 20 ng/ml hFGF and 10 μM retinoic acid (RA) for BCEC expansion. On day 8, BCECs were dissociated using Accutase for 30 min and seeded at a cell density of 1 x 10^6 cell/cm^2 onto collagen IV/ fibronectin-coated transwell membranes (0.4 μm pore size, 24-well format, Greiner) in EC medium supplemented with 20 ng/mL hFGF and 10 μM RA. BCECs were adapted to EC medium without hFGF and RA at day 9 for 24 h. We measured transendothelial electrical resistance (TEER) values using an electrode to evaluate the integrity of the in vitro BBB. Only BBBs with TEER values ≥ 1000 Ω*cm^2 at day 10 were included. To monitor monolayer integrity for both iPSC-derived BBB models, 10 μM sodium fluorescein (Sigma-Aldrich) was added to the apical compartment of two reference inserts for each BCEC differentiation. The intensity of the fluorescent tracer molecule was measured in pooled samples of both compartments respectively using a fluorescent plate reader (Infinite M1000 Pro, TECAN, excitation: 490 nm, emission: 525 nm). We applied 10 μM sildenafil, sildenafil citrate, or reference compounds in EC medium to the apical compartment of two inserts each and incubated the cells for 1 h at 37 °C, 5 % CO_2 on an orbital shaker (100 rpm). Diazepam and atenolol were used as internal controls given their known high and low BBB permeability, as previously demonstrated.[151,152] Media from both the apical (A) and basolateral (B) compartments were collected, pooled and stored at -80 °C until quantification. Peak areas were used to calculate the apparent permeability (*P*app) of each substance using equation:

$$Papp = \frac{\Delta Q}{\Delta t \times A\left(\frac{C_D + C_0}{2}\right) \times 10^6}$$

$$\Delta Q = Conc.\, receiver \Delta t$$

$$\Delta t \; = \; incubation \; time$$

$$A = filter \; surface \; area \left[\frac{cm^2}{well}\right]$$

$$C_D = Conc. \; donor \Delta t$$

$$C_0 = Conc. \; donor \; t_0$$

Quantification of sildenafil, diazepam and atenolol in apical and basolateral media samples was performed using LC-MS/MS. The settings were maintained except for minor adjustments. Chromatographic separation of atenolol ($t_R = 3.5$ min), sildenafil ($t_R = 4.3$ min) and diazepam ($t_R = 5.5$ min) was achieved with gradient elution within 10 min of total run-time. After positive electrospray ionization, the MS/MS detector recorded three mass transitions per drug compound (fragmentor voltage [FV] and collision energies [CE] in parentheses): Sildenafil: *m/z* 475.2 → 58.0 (FV: 220 V, CE: 68 eV, *quantifier*), *m/z* 475.2 → 100.0 (FV: 220 V, CE: 28 eV), *m/z* 475.2 → 283.1 (FV: 220 V, CE: 44 eV); Diazepam: *m/z* 285.1 → 154.1 (FV: 144 V, CE: 28 eV), *m/z* 285.1 → 193.1 (FV: 144 V, CE: 36 eV, *quantifier*), *m/z* 285.1 → 222.1 (FV: 144 V, CE: 28 eV) and Atenolol: *m/z* 267.2 → 56.0 (FV: 128 V, CE: 32 eV), *m/z* 267.2 → 74.1 (FV: 128 V, CE: 24 eV), *m/z* 267.2 → 144.9 (FV: 128 V, CE: 28 eV, *quantifier*). Peak areas were determined with MassHunter Quantitative Analysis software (version 10.1, Agilent Technologies) and the three drugs were quantified using matrix-matched external calibration in the concentration range of 0.001 to 10 μM.

iPSC-derived cardiomyocyte (iPSC-CMs)

iPSC-CMs lines were obtained through WNT signaling modulation followed by metabolic selection, as previously described.[153,154] The resulting iPSC-CMs were maintained under feeder-free, serum-free culture conditions until day 60 post-differentiation. Confirmation of iPSC-CM identity was performed by immunostaining against alpha-actinin (ACTN2) (Sigma-Aldrich) and mitochondria were visualized with MitoSpy (BioLegend).

To assess cell viability, 100,000 LS iPSC-CMs (ATP6_7) per well were seeded in 24-well plates. Following a seven-day period of recovery, sildenafil treatment (vehicle, 10 μM, 50 μM, 250 μM) was initiated and maintained for 24 h on alternate days by dilution in RPMI media. For imaging acquisition, the Calcein AM Viability Dye (Invitrogen) was dissolved in DMSO at 1 mg/ml, and applied at a final concentration of 1 μM in RPMI for 30 min at 37 °C. After incubation, cells were washed twice with 1 x DPBS. Propidium iodide (PI) (Invitrogen) was diluted in RPMI to 1.5 mM and administered at a final concentration of 500 nM. Imaging and analysis were performed using the Incucyte live-cell analysis system.

For Glycostress test, LS iPSC-CMs (ATP6_6 and ATP6_7) were seeded in 24-well Seahorse assay plates at a density of 100,000 cells/well ten days prior the experiment. A Glycostress test was used to evaluate glycolysis activity, following a previously established protocol.[155] One hour before assay initiation, the cell culture medium was replaced with glucose-free Agilent XF assay medium and iPSC-CMs were incubated for 20 min at 37 °C in the absence of CO_2. After three baseline acidification rate recordings, 10 mM of glucose was injected, followed by a sequential injection of 1 μM ATP synthase inhibitor oligomycin A, and 100 mM 2-deoxy-D-glucose. Measurements of extracellular acidification were obtained via a Seahorse XFe24 Analyzer. Total protein content served as normalization for oxygen consumption rate (OCR) in each well.

Computational modeling of calcium and bioenergetics

To determine the effect of impaired calcium signaling on mitochondrial function in LS, we applied a mathematical model that couples cytosolic calcium dynamics with mitochondrial function.[70] The cytosolic calcium equations were modified to incorporate calcium exchange between the cytoplasm and extracellular space through plasma membrane calcium ATPase (PMCA) and store-operated calcium channels (SOCC). In this model, both PMCA and sarcoplasmic/endoplasmic reticulum calcium ATPase (SERCA) fluxes depend on the ATP levels to capture the potential rise in cytosolic calcium due to reduced ATP levels in cells with *MT-ATP6* variants. Parameters used in the model are based on previous works[70,156–162] and listed in Table S2. We converted the calcium fluorescence traces from cBOS (Figure 4B) into corresponding cytosolic calcium concentration ($\left[Ca^{2+}\right]_c$) using the formula developed before.[163] That is,

$$\Delta\left[Ca^{2+}\right]_c = k_D\left(\frac{F_{max}}{F_0}\left(1 - \frac{1}{R_F}\right)\frac{\Delta F}{(\Delta F_{max} - \Delta F)\Delta F_{max}}\right). \qquad \text{(Equation 1)}$$

Where $\Delta\left[Ca^{2+}\right]_c = \left[Ca^{2+}\right]_c - \left[Ca^{2+}\right]_0$ is the change in $\left[Ca^{2+}\right]_c$, $\left[Ca^{2+}\right]_0 = 0.1$ μM is the baseline cytosolic Ca^{2+} concentration, $k_D = 0.2$ mM in the dissociation constant for OBG-1 (used to label cytoplasmic calcium in cBOS), and $R_F = \frac{F_{max}}{F_{min}}$. F_{max} and F_{min} are the maximum and minimum fluorescent values in a trace, respectively. The instantaneous change in fluorescence is $\Delta F = F - F_0$, where $F_0 = 0.01$ is the baseline fluorescence. Finally, $\Delta F_{max} = F_{max} - F_0$ with F_{max} as the maximum fluorescence in the trace. To match the smaller timestep used in simulating mitochondrial bioenergetics, the time trace was interpolated. The resulting $\left[Ca^{2+}\right]_c$ traces were used for fitting the model to the observations in cells from MT-ATP6 and MT-ATP6 + Sil experiments. Rate equations for

$\left[Ca^{2+}\right]_c$, fraction of inactivated inositol 1,4,5-trisphsphate (IP$_3$) receptors (R_i), mitochondrial Ca^{2+} ([Ca^{2+}]$_m$), NADH ([NADH]$_m$), ADP ([ADP]$_m$), MMP ([$\Delta\psi$]), and cytosolic ADP ([ADP]$_c$) were adopted from Wacquier et al.[70] and Csordás et al.[164] The equation for $\left[Ca^{2+}\right]_c$ was modified to incorporate the effect of PMCA and SOCC entry from the extracellular space. These equations were solved in MATLAB 2023b using ode15s method, and are given as:

$$\frac{d\left[Ca^{2+}\right]_c}{dt} = f_c(\alpha J_{IP3} - J_{SERCA} - J_{PMCA} + J_{SOCC} + J_{SERCA} - \delta J_{MCU} - \delta J_{NCX} - \delta J_X) \qquad \text{(Equation 2)}$$

$$\frac{dR_i}{dt} = k^+ \left[Ca^{2+}\right]_c^{n_i} \left(\frac{1 - R_i}{1 + \left(\frac{\left[Ca^{2+}\right]_c}{K_a} \right)^{n_a}} \right) - k^- R_i \qquad \text{(Equation 3)}$$

$$\frac{d\left[Ca^{2+}\right]_m}{dt} = f_m(J_{MCU} - J_{NCX} + J_X), \qquad \text{(Equation 4)}$$

$$\frac{d[NADH]_m}{dt} = J_{PDH} + J_{AGC} - J_o, \qquad \text{(Equation 5)}$$

$$\frac{d[ADP]_m}{dt} = J_{ANT} - J_{F1F0}, \qquad \text{(Equation 6)}$$

$$\frac{d[ADP]_c}{dt} = J_{HYD} - \delta J_{ANT}, \qquad \text{(Equation 7)}$$

$$\frac{d\Delta\psi}{dt} = \frac{1}{c_{mito}}(b_1 J_O - b_2 J_{F1F0} - J_{ANT} - J_{H,LEAK} - J_{NCX} - 2J_{MCU} - 2J_X - J_{AGC}). \qquad \text{(Equation 8)}$$

Where Ca^{2+} fluxes from the endoplasmic reticulum (ER) to the cytoplasm through IP$_3$ receptors (J_{IP3}), from the cytoplasm to the ER through SERCA (J_{SERCA}), from the cytoplasm to the extracellular space (ECS) through PMCA (J_{PMCA}), from the ECS to the cytoplasm through SOCC (J_{SOCC}), from the cytoplasm to mitochondria through mitochondrial calcium uniporter (MCU) (J_{MCU}), and from mitochondria to the cytoplasm through Na$^+$/Ca^{2+} exchangers (NCX) (J_{NCX}) are given as:

$$J_{IP3} = v_{IP3}(b_{IP3} + IR_a)\left(\left[Ca^{2+}\right]_{er} - \left[Ca^{2+}\right]_c\right), \qquad \text{(Equation 9)}$$

$$IR_a = (1 - R_i)\left(\frac{IP_3^2}{K_i^2 + IP_3^2}\right)\left(\frac{\left[Ca^{2+}\right]_c^{na}}{K_a^{na} + \left[Ca^{2+}\right]_c^{na}}\right). \qquad \text{(Equation 10)}$$

We modeled metabolic stress by a rise in IP$_3$ concentration through the phospholipase C (PLC) pathway due to the rise in glutamate during metabolic stress, which is formulated by equation (11). Metabolic stress also impairs the fluxes through PMCA and SERCA through a decrease in [ATP]$_c$, which is already incorporated in their respective equations. One can also model metabolic stress by decreasing the rate at which NADH is oxidized in the electron transport chain (ETC) (and/or decreasing the rate of glycolytic pathway and other complexes in ETC) by itself or in combination with a rise in IP$_3$ concentration. However, using this later approach does not change the conclusions from the model.

$$IP_3 = a_{01}\left(\frac{1}{e^{\frac{470-(t-t_{stim})}{10}}+1} + \frac{3.5}{e^{\frac{450-(t-300-t_{stim})}{40}}+1}\right)e^{\frac{-(t-t_{stim})}{100}}, \qquad \text{(Equation 11)}$$

$$\left[Ca^{2+}\right]_{er} = \frac{f_{ER}}{\propto}\left(C_{tot} - \frac{\left[Ca^{2+}\right]_c}{f_c} - \frac{\delta\left[Ca^{2+}\right]_m}{f_m}\right), \qquad \text{(Equation 12)}$$

$$J_{SERCA} = v_P \frac{\left[Ca^{2+}\right]_c^2}{K_P^2 + \left[Ca^{2+}\right]_c^2} \frac{[ATP]_c}{K_e + [ATP]_c}. \quad \text{(Equation 13)}$$

$$J_{PMCA} = v_{PMCA} \left(\frac{\left[Ca^{2+}\right]_c^2}{0.25 + \left[Ca^{2+}\right]_c^2} \right) \left(\frac{[ATP]_c}{300 + [ATP]_c} \right), \quad \text{(Equation 14)}$$

$$J_{SOCC} = v_{SOCC} \frac{K_{SOCC}^4}{K_{SOCC}^4 + \left[Ca^{2+}\right]_{ER}^4}, \quad \text{(Equation 15)}$$

$$J_{MCU} = v_{MCU} \frac{\frac{\left[Ca^{2+}\right]_c}{K_1} \left(1 + \frac{\left[Ca^{2+}\right]_c}{K_1} \right)^3}{\left(1 + \frac{\left[Ca^{2+}\right]_c}{K_1} \right)^4 + \frac{L}{\left(1 + \frac{\left[Ca^{2+}\right]_c}{K_2} \right)^{2.3}}} e^{p_1 \Delta\psi}, \quad \text{(Equation 16)}$$

$$J_{NCX} = v_{NCX} \left(\frac{\left[Ca^{2+}\right]_m}{\left[Ca^{2+}\right]_c} \right) e^{p_2 \Delta\psi} \quad \text{(Equation 17)}$$

The additional Ca^{2+} flux (J_x) was added to capture the many experimental results, and particularly the observations that mitochondrial Ca^{2+} does not drop to zero in MCU knocked-down cells.[70,164]

$$J_x = v_x \left(\left[Ca^{2+}\right]_c - \left[Ca^{2+}\right]_m \right) e^{p_3 \Delta\psi}. \quad \text{(Equation 18)}$$

The effects of pyruvate dehydrogenase (PDH)-catalyzed reaction, glycolytic pathway (v_{GLY}), and the TCA cycle (reduction of $[NAD^+]_m$ into NADH) is formulated as:

$$J_{PDH} = v_{GLY} \frac{1}{q_1 + \frac{[NADH]_m}{[NAD^+]_m}} \frac{\left[Ca^{2+}\right]_m}{q_2 + \left[Ca^{2+}\right]_m}, \quad \text{(Equation 19)}$$

The aspartate-glutamate carrier (AGC) is part of MAS NADH shuttle system defined as:

$$J_{AGC} = v_{AGC} \frac{\left[Ca^{2+}\right]_c}{K_{AGC} + \left[Ca^{2+}\right]_c} \frac{q_2}{q_2 + \left[Ca^{2+}\right]_m} e^{p_4 \Delta\psi}. \quad \text{(Equation 20)}$$

The rate at which NADH is oxidized in the ETC and the rate at which protons are extruded from the mitochondria are combined into one equation as:

$$J_O = v_O \frac{[NADH]_m}{q_3 + [NADH]_m} \left(1 + e^{\frac{\Delta\psi - q_4}{q_5}} \right)^{-1}. \quad \text{(Equation 21)}$$

The activity of adenine nucleotide translocator (ANT) in electrogenic exchange of ATP or ADP across the inner mitochondrial membrane is given by:

$$J_{ANT} = v_{ANT} \frac{1 - \left(\frac{\propto_c}{\propto_m} \right) \left(\frac{[ATP]_c}{[ADP]_c} \right) \left(\frac{[ADP]_m}{[ATP]_m} \right)}{\left(1 + \propto_c \frac{[ATP]_c}{[ADP]_m} e^{-0.5 \frac{F\Delta\psi}{RT}} \right) \left(1 + \frac{[ADP]_m}{\propto_m [ATP]_m} \right)} e^{-\frac{F\Delta\psi}{RT}}, \quad \text{(Equation 22)}$$

where $\propto_c$ and $\propto_m$ denote the fact that only a fraction of nucleotides has access to the transporter. The dependence of the membrane potential is due to the negatively charged ADP and ATP. The rate of ATP synthesis by F_1F_0 ATPase is modeled as:

$$J_{F1F0} = v_{F1F0}\left(\frac{q_6}{q_6+[ATP]_m}\right)\left(1+e^{\frac{q_7-\Delta\psi}{q_8}}\right)^{-1}. \quad \text{(Equation 23)}$$

J_{HYD} represents the rate of ATP consumption (ATP hydrolysis) in the cytosol. The first term encodes the link between Ca^{2+} activity and ATP consumption in the cytosol whereas the second term captures ATP-consuming processes in the cytosol.

$$J_{HYD} = \frac{J_{SERCA}}{2}+\frac{J_{PMCA}}{2}+v_{HYD}\frac{[ATP]_c}{K_h+[ATP]_c}. \quad \text{(Equation 24)}$$

The Ohmic mitochondrial proton leak is given as:

$$J_{H,LEAK} = q_9\Delta\psi+q_{10}. \quad \text{(Equation 25)}$$

Finally, the total NADH, ADP, and ATP in the mitochondria and cytosol are given by conservation equations. That is:

$$[NADH]_m + [NAD^+]_m = [NAD]_m^{TOT}, \quad \text{(Equation 26)}$$

$$[ADP]_m + [ATP]_m = [A]_m^{TOT}, \quad \text{(Equation 27)}$$

$$[ADP]_c + [ATP]_c = [A]_c^{TOT}. \quad \text{(Equation 28)}$$

For global sensitivity analysis, we computed the first-order and total-order Sobol′ sensitivity indices following previous estimators[165,166] using Sobol-sequence sampling[167] including: resting value, amplitude value under metabolic stress (peak value – resting value), and full duration at half maximum (FDHM) value (the duration for which a variable is above (peak value – resting value) / 2). We modulated the key 8 parameters related to cytosolic calcium and mitochondrial bioenergetics: maximum rate of F_1F_0 ATPase activity (v_{F1F0}), glycolysis (v_{GLY}), adenine nucleotide translocator (v_{ANT}), NADH production via aspartate-glutamate carrier (v_{AGC}), NADH oxidation in ETC (v_O), plasma membrane calcium ATPase (v_{PMCA}), sarcoplasmic/endoplasmic reticulum calcium ATPase (v_{SERCA}), and of IP_3 receptors (v_{IP3R}). The model outputs were not very sensitive to other parameters and are therefore not presented. These 8 parameters were varied to analyze their effect on the 6 core variables: $[Ca^{2+}]_c$ (cytosolic calcium), $[Ca^{2+}]_c$ (mitochondrial calcium), $[NADH]_m$ (mitochondrial NADH), MMP, $[ATP]_m$ (mitochondrial ATP), $[ATP]_c$ (cytosolic ATP). In total, we delivered 18 model outputs from 81,920 model runs. In the generated graphs for the global sensitivity analysis (Figure S9A), the bullet size represents the significance of the effect of a parameter on a given model output (larger bullet means changing the parameter affects the output more) and the thickness of the edge indicates the significance of the interaction between the two parameters on the model output (thicker edge means changing the two parameters simultaneously affect the output more).

QUANTIFICATION AND STATISTICAL ANALYSIS

We analyzed the data using GraphPad-Prism software and employed the R environment for statistical computing. For all datasets, we tested the normality of the distribution using GraphPad-Prism (D'Agostino-Pearson test for large sample sizes and Shapiro-Wilk test for sample sizes under 50). After having performed outlier test analyses, we assessed statistical significance using parametric tests for normally distributed data (Student's *t* test, ANOVA) and non-parametric tests when normal distribution could not be verified (Mann-Whitney U and Kruskal-Wallis test). When possible, data are presented as scatter plots with individual data points showing all individual measurements. Unless otherwise indicated, we expressed the data as mean and standard deviation (mean ± SD). Experiments were repeated in independent biological experiments. Information on statistical details and number of replicates can be found in the respective figure legends. Figures were prepared with Adobe Illustrator.

Supplemental figures

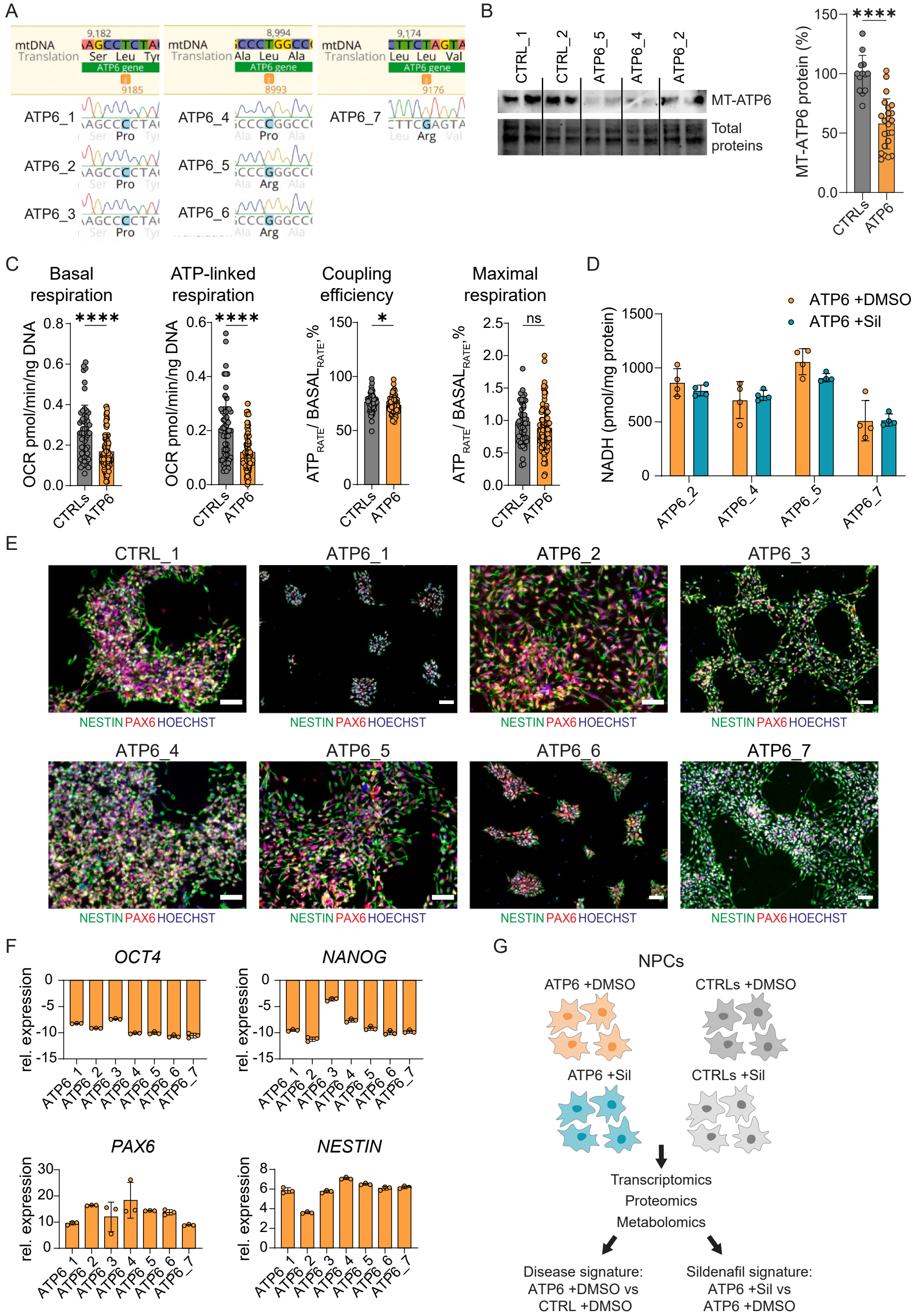

(legend on next page)

Figure S1. Generation of LS NPCs, related to Figures 1 and 2

(A) Genotyping of LS NPCs.

(B) Representative immunoblot and related quantification of MT-ATP6 protein expression in control NPCs and LS NPCs representing the four *MT-ATP6* variants (ATP6_2 for m.9176T>C, ATP6_4 for m.8993T>C, ATP6_5 for m.8993T>G, and ATP6_7 for m.9176T>G). $n = 3$ independent experiments. $^{****}p < 0.0001$; unpaired two-tailed *t* test.

(C) Seahorse-based bioenergetic profile of control NPCs (CTRL_1 and CTRL_2) and LS NPCs (ATP6_2, ATP6_4, ATP6_5, and ATP6_7). $n = 3$ independent experiments. Mean ± SD, $^{****}p < 0.0001$, $^{*}p < 0.05$; unpaired two-tailed *t* test.

(D) NADH quantification in LS NPCs treated with DMSO or 10 µM sildenafil for 16 h ($n = 3$ independent biological replicates per sample).

(E) Representative immunostaining of LS NPCs. Scale bar: 50 µm.

(F) qPCR analysis showing downregulation of iPSC markers *OCT4* and *NANOG*, and upregulation of NPC markers *NESTIN* and *PAX6* in LS NPCs compared with their respective LS iPSC lines. Mean $\log_2$ ratios (mean ± SD) in relation to control iPSCs (CTRL_1).

(G) Schematic of omics setup in control NPCs (CTRL_1, CTRL_2, CTRL_3, and CTRL_4) and LS NPCs (ATP6_2, ATP6_4, ATP6_5, and ATP6_7) to dissect the disease signature and sildenafil signature.

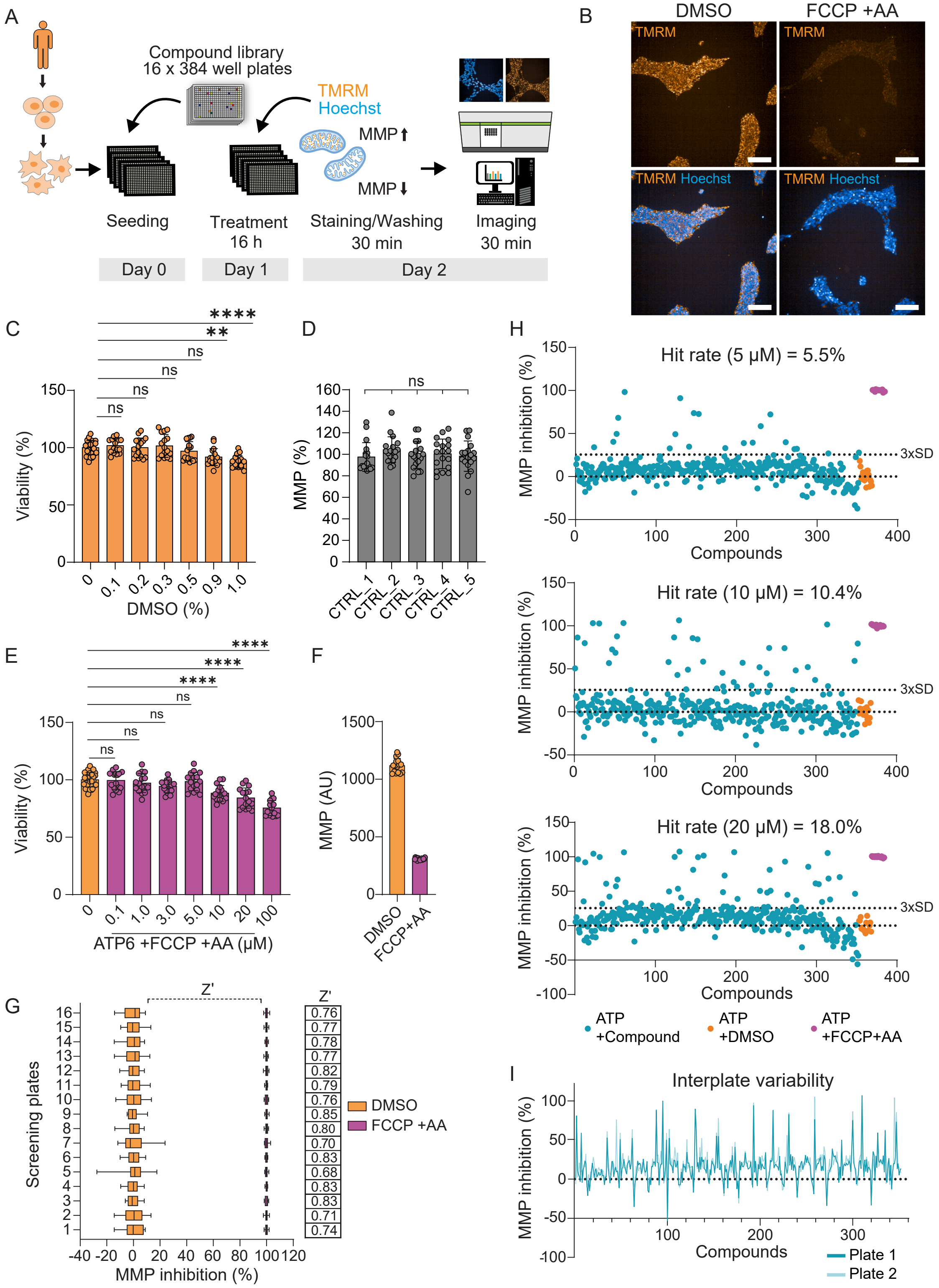

Figure S2. Compound screening in LS NPCs, related to Figure 1

(A) Compound screening workflow in LS NPCs.

(B) Representative images of LS NPCs (ATP6_2) treated with DMSO or 5 µM carbonyl cyanide-p-trifluoromethoxyphenylhydrazone (FCCP) and 5 µM antimycin A (AA) and live-cell stained with TMRM and Hoechst. Scale bar: 100 µm.

(legend continued on next page)

(C) Cell viability in LS NPCs (ATP6_2). Dots: mean value/well. **$p < 0.01$, ****$p < 0.0001$; ordinary one-way ANOVA with Dunnett's multiple comparisons.

(D) HCA MMP in control NPC lines. Dots: mean value/well, $n = 3$ independent experiments; ordinary one-way ANOVA with Dunnett's multiple comparisons.

(E) Cell viability in LS NPCs (ATP6_2) after 16 h treatment with increasing FCCP + AA concentrations, normalized to DMSO (0 value). Dots: mean value/well. ****$p < 0.0001$; ordinary one-way ANOVA with Dunnett's multiple comparisons.

(F) HCA MMP in LS NPCs (ATP6_2) treated for 16 h with either 0.05% DMSO or 5 μM FCCP + AA. Dots: mean value/well.

(G) HCA MMP in LS NPCs (ATP6_2) in independent screening plates showing stability of Z′ factor.

(H) Screening tests with 16 h treatment of 352 compounds in LS NPCs (ATP6_2). Blue dots: compounds in DMSO; orange dots: DMSO only; purple dots: 5 μM FCCP + AA as positive controls. Upper dotted line: 3 × SD.

(I) HCA MMP in LS NPCs (ATP6_2) with 352 compounds (10 μM after 16 h) in different screening plates.

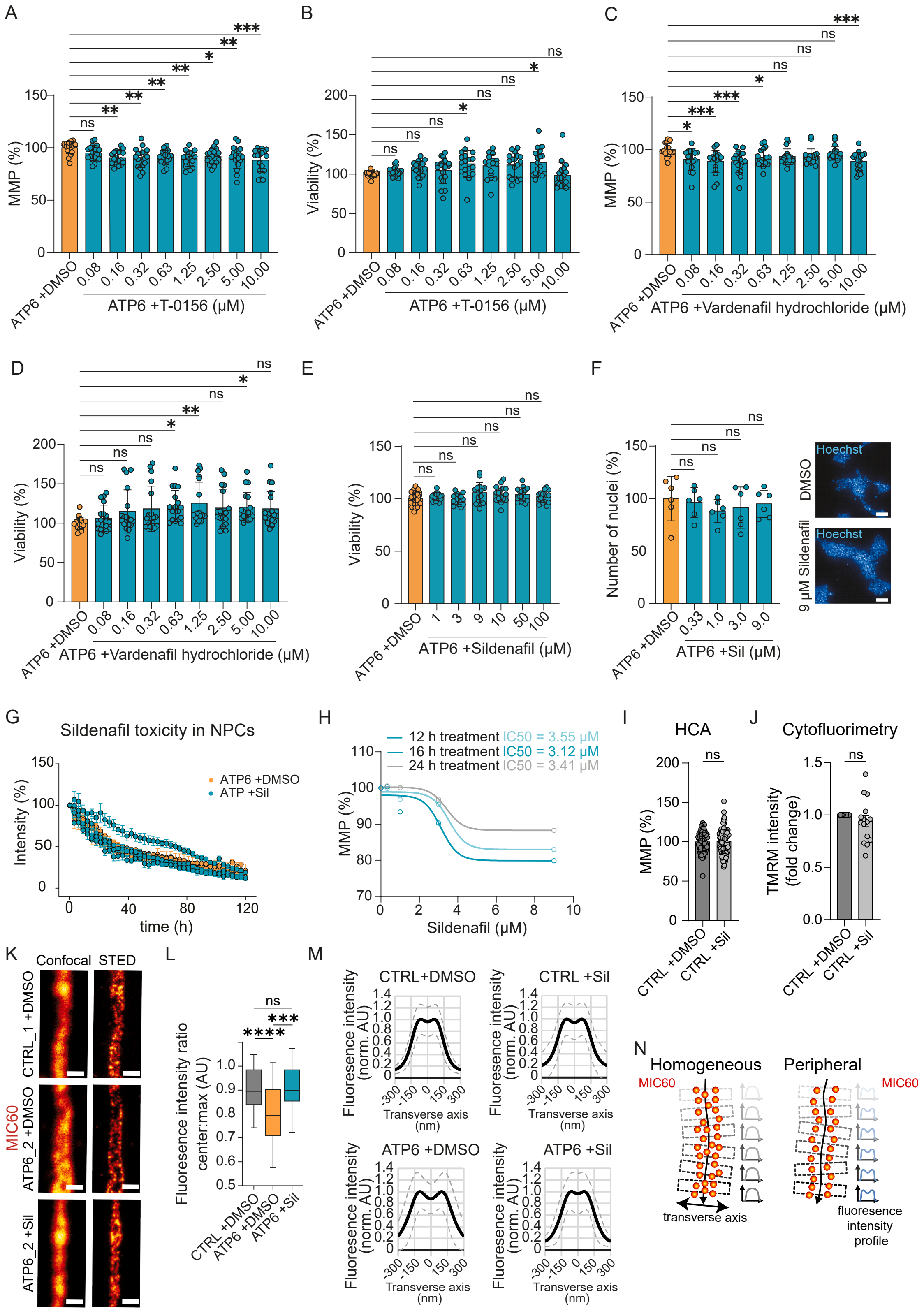

(legend on next page)

Figure S3. PDE5i compounds normalize MMP in LS NPCs, related to Figure 1

(A–D) HCA MMP and cell viability of LS NPCs (ATP6_2) treated with T-0156 or vardenafil hydrochloride compared with DMSO. Dots: mean value/well, $n = 3$ independent experiments. $^{*}p < 0.05$, $^{**}p < 0.01$, $^{***}p < 0.001$; ordinary one-way ANOVA with Dunnett's multiple comparisons.

(E) Cell viability of LS NPCs (ATP6_2) treated with sildenafil ($n = 16$ replicates) compared with DMSO ($n = 31$ replicates); ordinary one-way ANOVA with Dunnett's multiple comparisons.

(F) HCA Hoechst staining in LS NPCs (ATP6_2) treated with sildenafil. Dots: mean value/well; ordinary one-way ANOVA with Dunnett's multiple comparisons. Scale bar: 100 μm.

(G) Proliferation-based toxicity in LS NPCs (ATP6_2, ATP6_4, ATP6_5, and ATP6_7) treated with 0.1% DMSO (orange) or 10 μM sildenafil in 0.1% DMSO (cyan). Dots: individual signal for each line, $n = 3$ independent experiments.

(H) IC_{50} values in LS NPCs (ATP6_2) treated with sildenafil. Dots: mean value/well.

(I and J) HCA MMP and cytofluorimetry MMP in control NPCs (CTRL_1) treated with 10 μM sildenafil for 16 h.

(K) Representative images of MIC60 in control NPCs (CTRL_1) and LS NPCs (ATP6_2) treated with DMSO or 1 μM sildenafil for 24 h. Scale bar: 500 nm.

(L) MIC60 central fluorescence intensity over maximal intensity recorded with STED microscopy for the transversal profiles shown in (M). $^{***}p < 0.001$, $^{****}p < 0.0001$; ordinary one-way ANOVA with Dunnett's multiple comparisons.

(M) MIC60 average fluorescence intensity profiles (black lines) across the transverse axis of mitochondria recorded with STED microscopy in control NPCs (CTRL_1) and LS NPCs (ATP6_2) treated with DMSO or 1 μM sildenafil for 24 h. Dashed lines: SD.

(N) Distribution pattern of MIC60 in mitochondrial cristae in control NPCs and sildenafil-treated LS NPCs (homogeneous distribution) compared with DMSO-treated LS NPCs (peripheral distribution).

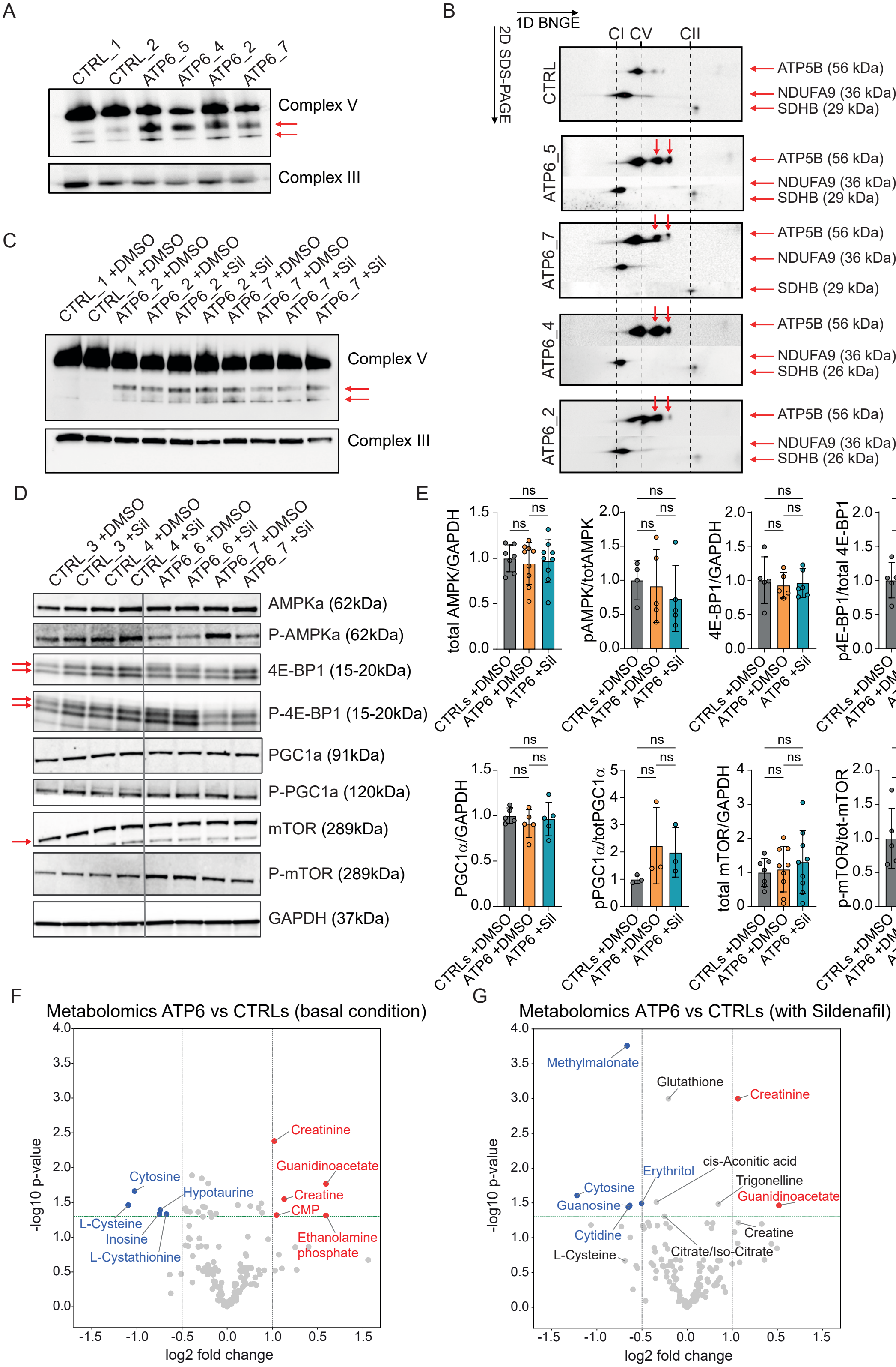

(legend on next page)

Figure S4. Effects of sildenafil on mitochondrial metabolism, related to Figures 1 and 2

(A) 1D-blue native gel electrophoresis (BNGE) images of n-dodecyl β-D-maltoside (DDM)-treated mitochondrial fraction of control NPCs and LS NPCs. ATP5B antibody: CV holoenzyme and intermediate subassemblies; UQCRFS1 antibody: complex III as loading control. *n* = at least 3 independent experiments.

(B) 2D-BNGE of samples in (A). Red arrows: subassembly forms. *n* = at least 3 independent experiments.

(C) 1D-BNGE images of DDM-treated mitochondrial fraction of control NPCs and LS NPCs treated with DMSO or 10 μM sildenafil for 16 h. ATP5B antibody: CV holoenzyme and intermediate subassemblies (red arrows).

(D) Representative immunoblot of control NPCs (CTRL_3 and CTRL_4) and LS NPCs (ATP6_6 and ATP6_7) treated with DMSO or 10 μM sildenafil for 16 h. UQCRFS1 antibody: complex III as loading control. *n* = at least 3 independent experiments.

(E) Quantification of immunoblot in (D), *n* = 3 independent experiments. Mean ± SD; one-way ANOVA with Tukey's multiple comparisons.

(F and G) Volcano plots of metabolomics depicting upregulated metabolites (red) and downregulated metabolites (blue) in LS NPCs (ATP6_2, ATP_4, ATP6_5, and ATP6_7), compared with control NPCs (CTRL_1, CTRL_2, CTRL_3, and CTRL_4), treated with DMSO or 10 μM sildenafil for 16 h.

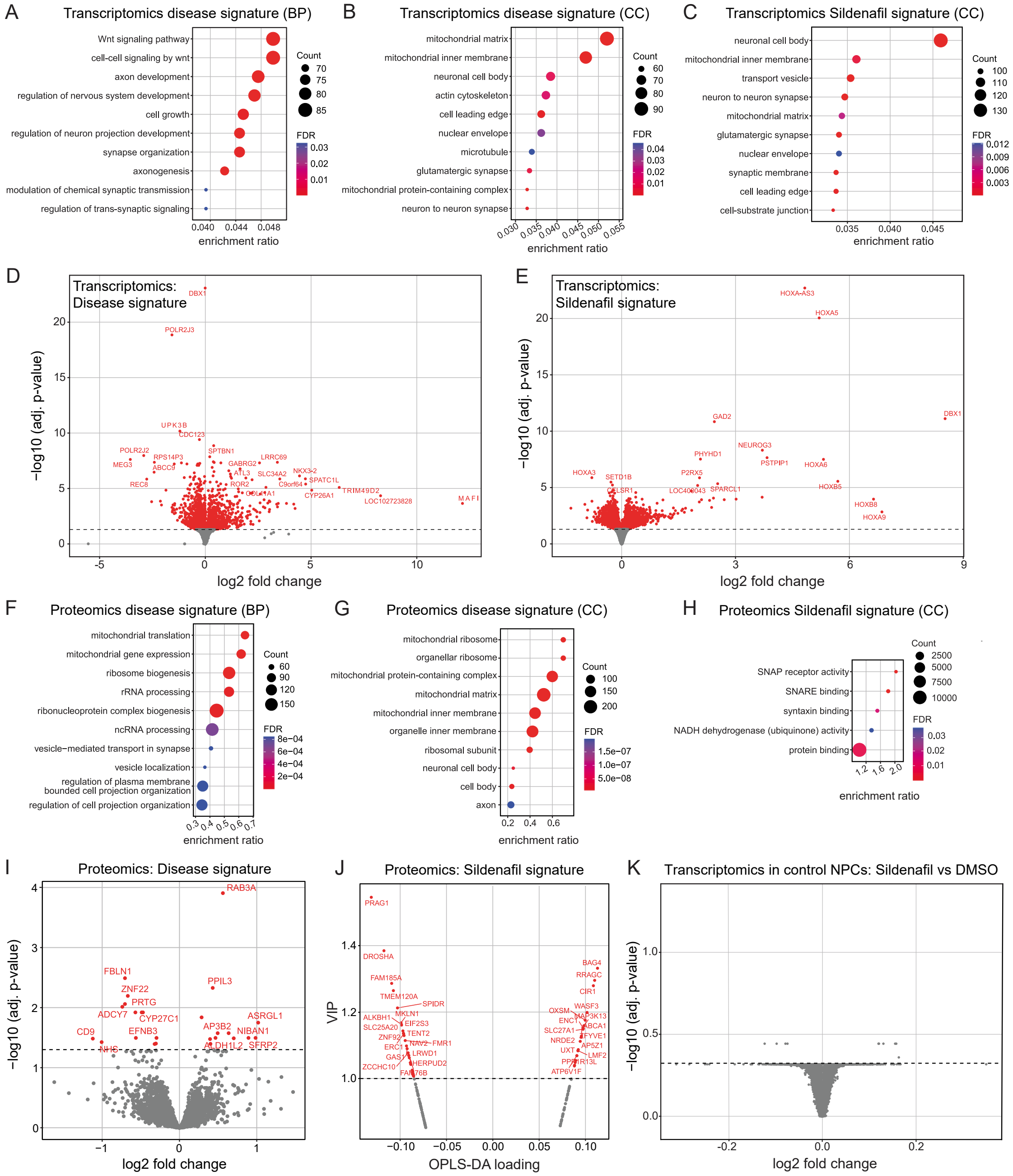

Figure S5. Disease signature and sildenafil signature revealed by multi-omics, related to Figure 2

(A and B) Top-ten Gene Ontology (GO) biological processes (BPs) and cellular components (CCs) in LS NPCs (ATP6_2, ATP_4, ATP6_5, and ATP6_7) compared with control NPCs (CTRL_1, CTRL_2, CTRL_3, and CTRL_4) based on transcriptomics.

(C) Top-ten GO CC in LS NPCs (ATP6_2, ATP_4, ATP6_5, and ATP6_7) treated with sildenafil for 16 h compared with DMSO based on transcriptomics.

(D and E) Differentially expressed genes (DEGs) (red dots) in LS NPCs (ATP6_2, ATP_4, ATP6_5, and ATP6_7) compared with control NPCs (CTRL_1, CTRL_2, CTRL_3, and CTRL_4) and in LS NPCs (ATP6_2, ATP_4, ATP6_5, and ATP6_7) treated with sildenafil compared with DMSO.

(F and G) Top-ten GO BP and GO CC in LS NPCs (ATP6_2, ATP_4, ATP6_5, and ATP6_7) compared with control NPCs (CTRL_1, CTRL_2, CTRL_3, and CTRL_4) based on proteomics.

(H) Top-ten enriched GO CC in LS NPCs (ATP6_2, ATP_4, ATP6_5, and ATP6_7) treated with sildenafil for 16 h compared with DMSO based on proteomics.

(I) Differentially expressed proteins (DEPs) (red dots) in LS NPCs (ATP6_2, ATP_4, ATP6_5, and ATP6_7) compared with control NPCs (CTRL_1, CTRL_2, CTRL_3, and CTRL_4).

(J) DEPs (red dots) in LS NPCs (ATP6_2, ATP_4, ATP6_5, and ATP6_7) treated with sildenafil compared with DMSO using the machine-learning classifier OPLS-DA.

(K) Bulk transcriptomics of control NPCs (CTRL_1, CTRL_2, CTRL_3, and CTRL_4) treated with sildenafil compared with DMSO.

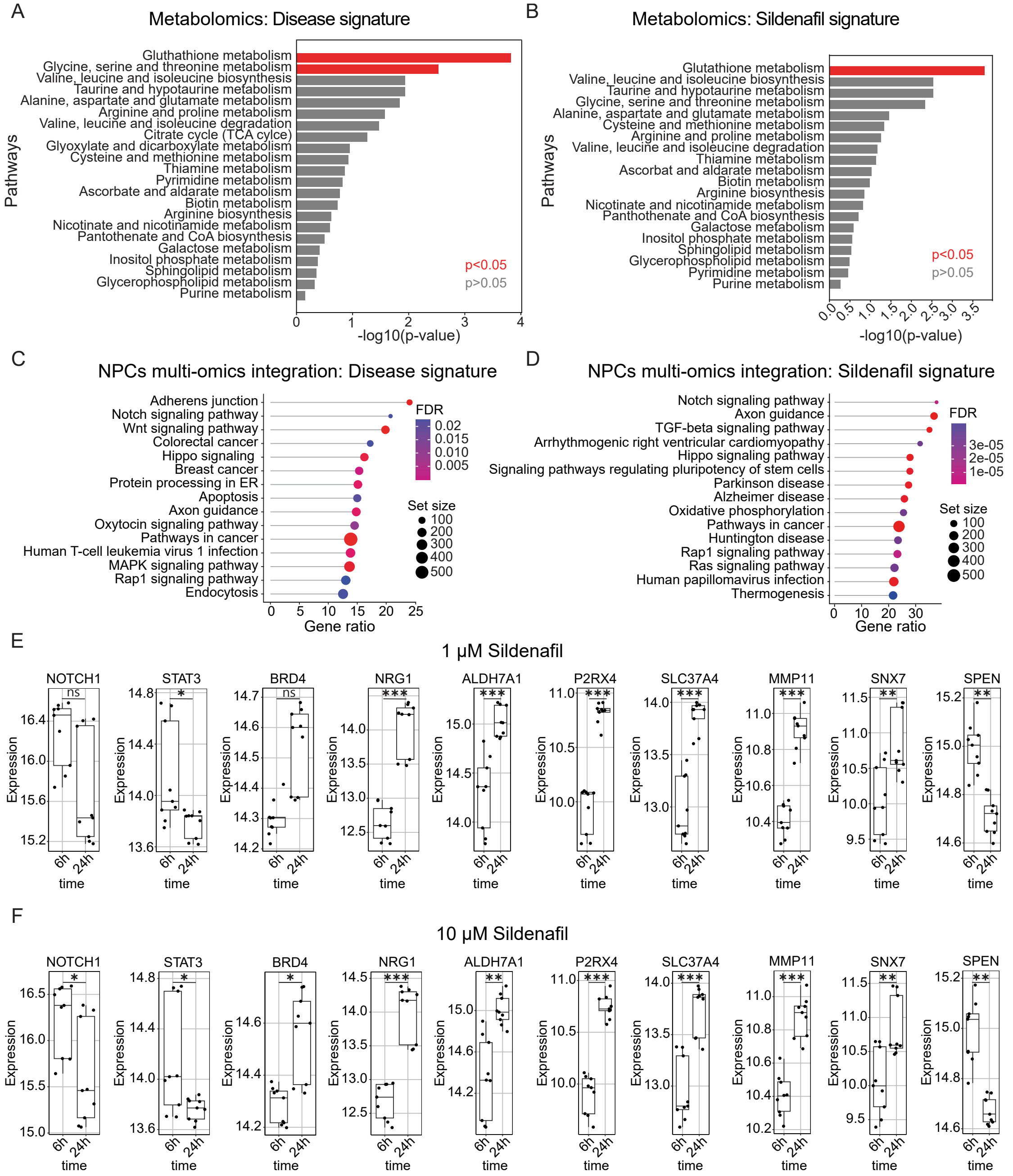

Figure S6. Metabolic signature of LS NPCs and multi-omics integration, related to Figure 2

(A and B) Altered metabolic pathways (red) and identified metabolic pathways (gray) in LS NPCs (ATP6_2, ATP_4, ATP6_5, and ATP6_7) compared with control NPCs (CTRL_1, CTRL_2, CTRL_3, and CTRL_4) (disease signature) and in LS NPCs treated with 10 μM sildenafil for 16 h compared with DMSO (sildenafil signature). One-way ANOVA with FDR adjustment for multiple comparisons ($p < 0.05$).

(C and D) Multi-omics integration: Kyoto Encyclopedia of Genes and Genomes (KEGG) pathways in LS NPCs compared with control NPCs (disease signature) or in LS NPCs treated with sildenafil compared with DMSO (sildenafil signature).

(E and F) Expression of putative sildenafil-responsive genes based on bulk transcriptomics of LS NPCs (ATP6_2, ATP6_4, ATP6_5, and ATP6_7) treated for 6 h or 24 h with 1 μM sildenafil (E) or with 10 μM sildenafil (F) compared with DMSO-treated LS NPCs. *y* axis: variance-stabilized counts obtained with DESeq2's vst() function; *p* values: computed with DESeq2 comparing expression levels at 24 h vs. 6 h, adjusted using Benjamini-Hochberg method.

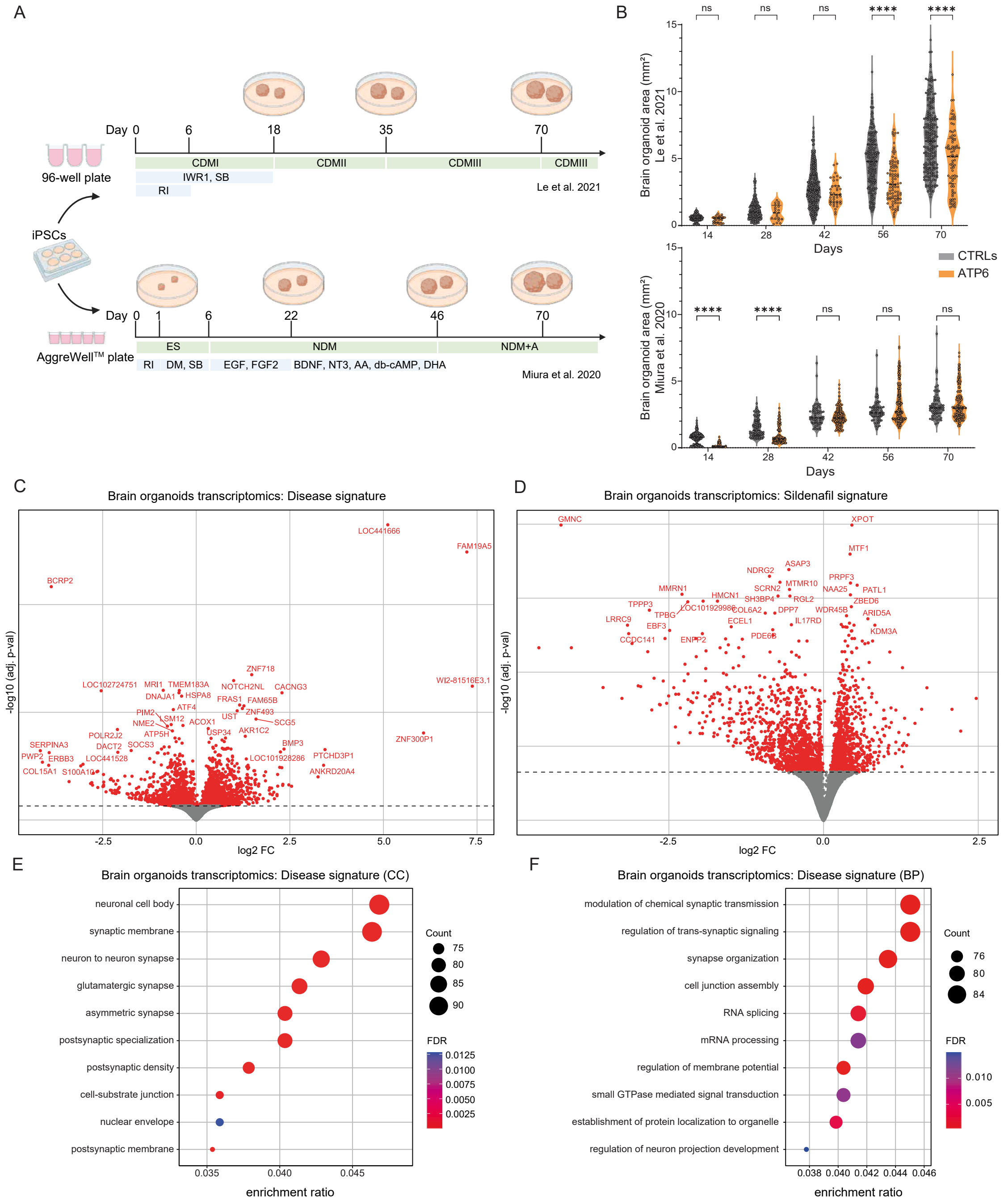

Figure S7. Brain organoid models of LS, related to Figure 3

(A) Schematic of the brain organoid protocols used: Le et al. with 96-well plates[62] or Miura et al. with AggreWells plates.[63]

(B) Size quantification of individual brain organoids grown following the two protocols until day 70. $****p < 0.0001$; two-tailed Mann-Whitney U test.

(C and D) DEG (red dots) in day 70 LS brain organoids (ATP6_2 and ATP6_7) compared with control brain organoids (CTRL_1 and CTRL_2) and in day 70 LS brain organoids (ATP6_2 and ATP6_7) treated with 10 μM sildenafil for 24 h compared with DMSO.

(E and F) Top-ten GO BP and GO CC in day 70 LS brain organoids (ATP6_2 and ATP6_7) compared with control brain organoids (CTRL_1 and CTRL_2) based on bulk transcriptomics.

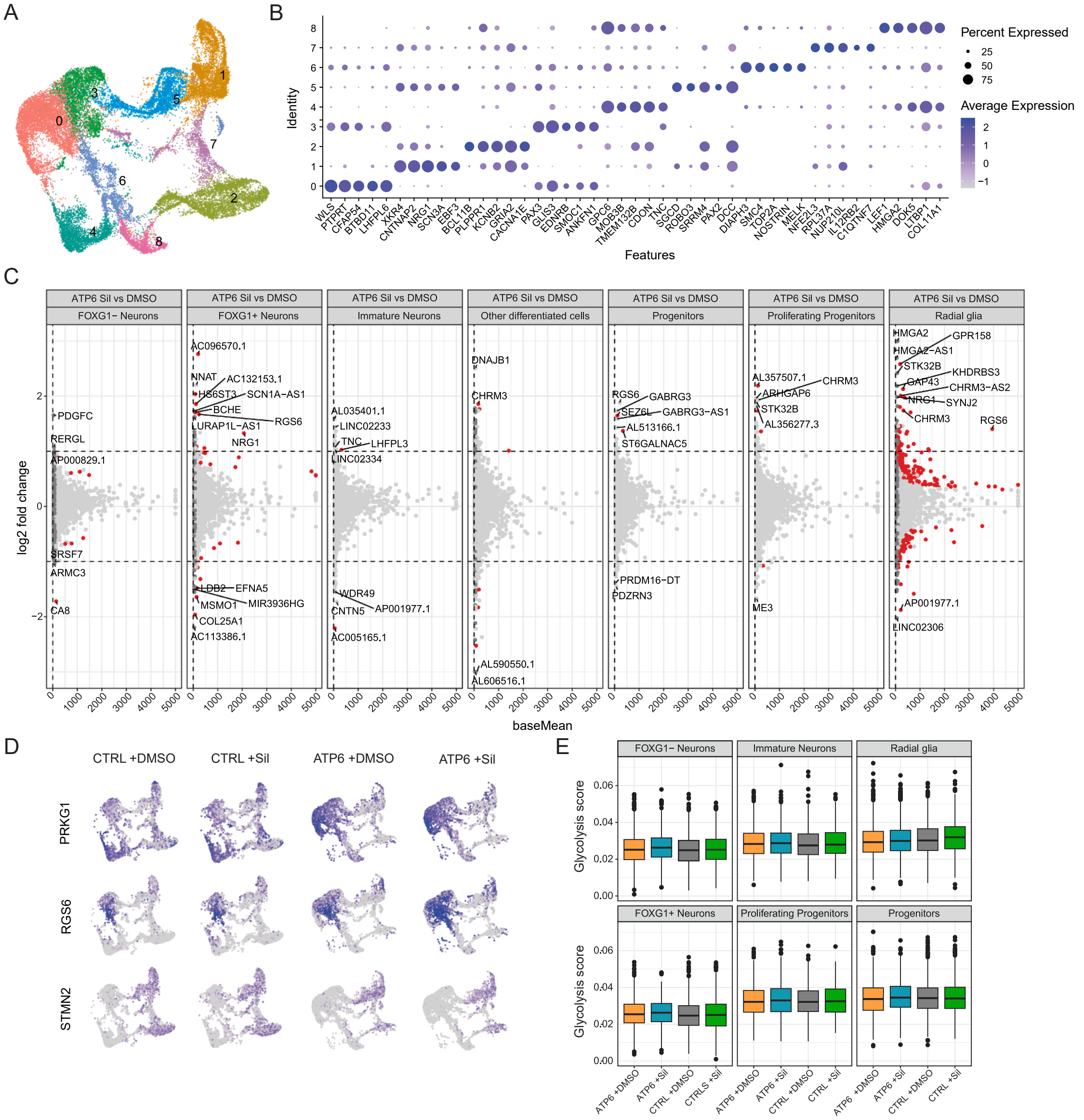

Figure S8. snRNA-seq of LS brain organoids, related to Figure 3

(A) Uniform manifold approximation and projection (UMAP) representation of 9 clusters in day 70 cortical brain organoids.

(B) Dot plot featuring five representative genes for each of the 9 clusters present in day 70 cortical brain organoids.

(C) DEG (red dots) in day 70 LS brain organoids (ATP6_7) treated with 10 μM sildenafil for 45 days compared with DMSO based on pseudo-bulk analysis of snRNA-seq.

(D) Expression distribution of *PRKG1*, *RGS6*, and *STMN2* in day 70 brain organoids from controls (CTRL_1) and LS (ATP6_7) treated with sildenafil or DMSO for 45 days.

(E) Molecular signatures database hallmark GLY score across the populations of day 70 brain organoids.

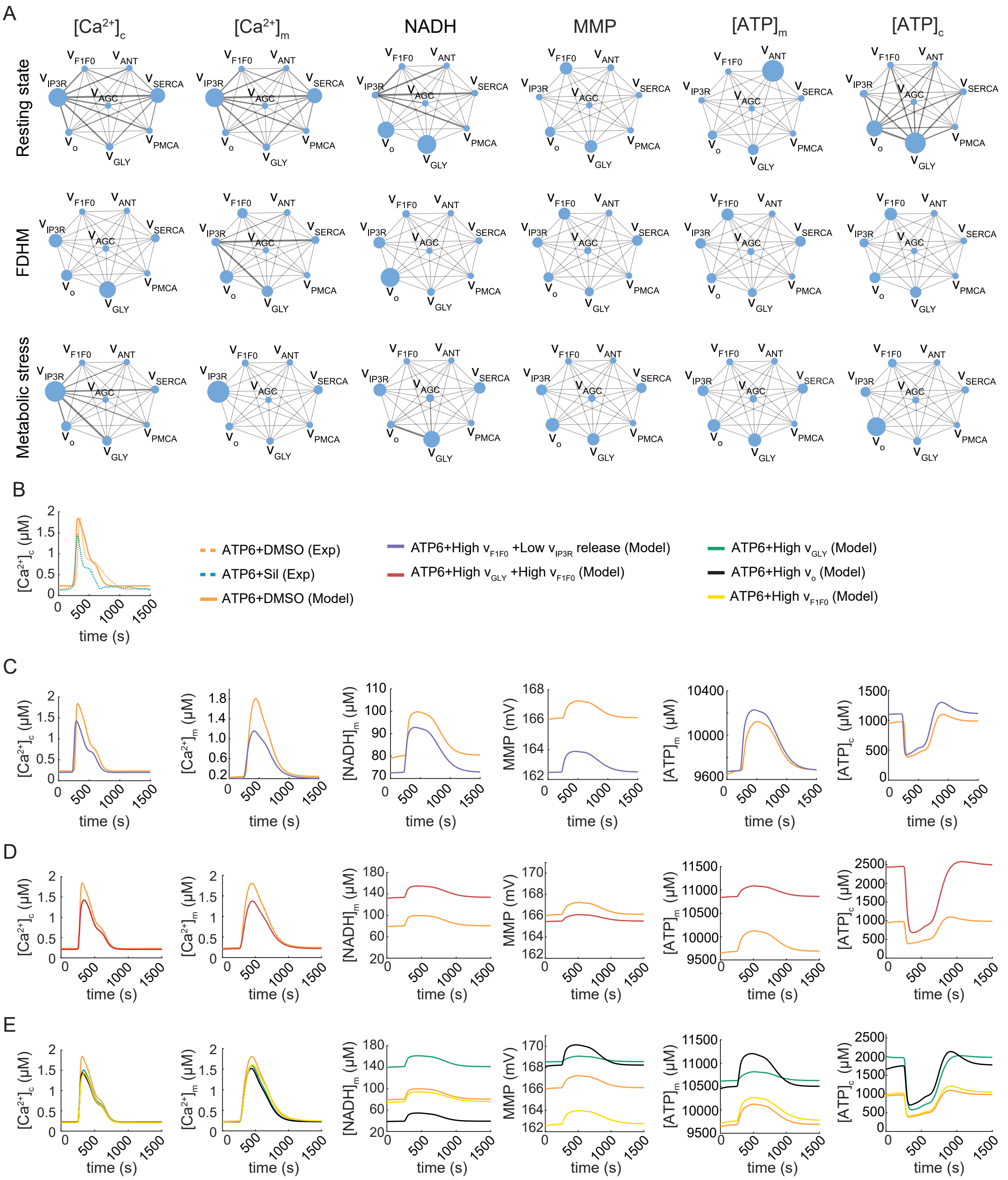

Figure S9. Computational model of calcium and bioenergetics, related to Figure 4

(A) Global sensitivity test for the mathematical model of calcium and bioenergetics. Values for resting state, full duration at half maximum (FDHM), and metabolic stress were computed for: [Ca^{2+}]$_c$ (cytosolic calcium), [Ca^{2+}]$_c$ (mitochondrial calcium), [NADH]$_m$ (mitochondrial NADH), MMP, [ATP]$_m$ (mitochondrial ATP), [ATP]$_c$ (cytosolic ATP) varying the key parameters: maximum rate of F$_1$F$_0$ ATPase activity (v_{F1F0}), GLY (v_{GLY}), ANT (v_{ANT}), NADH production via AGC (v_{AGC}), NADH oxidation in ETC (v_O), PMCA (v_{PMCA}), SERCA (v_{SERCA}), and of IP3Rs (v_{IP3R}). Bullet size: significance of the effect of a parameter; edge thickness: significance of the interaction between the two parameters.

(B) Comparison between experimental calcium traces obtained in LS cBOS and calcium traces computationally predicted by the mathematical model.

(C) Model prediction of the effects of *MT-ATP6* variants in basal conditions or in conditions with increased maximum rate of F1F0 (v_{F1F0}) together with decreased maximum rate of IP3R (v_{IP3R}).

(D) Model prediction of the effects of *MT-ATP6* variants in basal conditions or in conditions with increased maximum rate of GLY (v_{GLY}) together with increased maximum rate of F1F0 (v_{F1F0}).

(E) Model prediction of the effects of *MT-ATP6* variants in basal conditions or in conditions with increased maximum rate of either GLY (v_{GLY}), F1F0 (v_{F1F0}), or NADH oxidation in ETC (v_O).

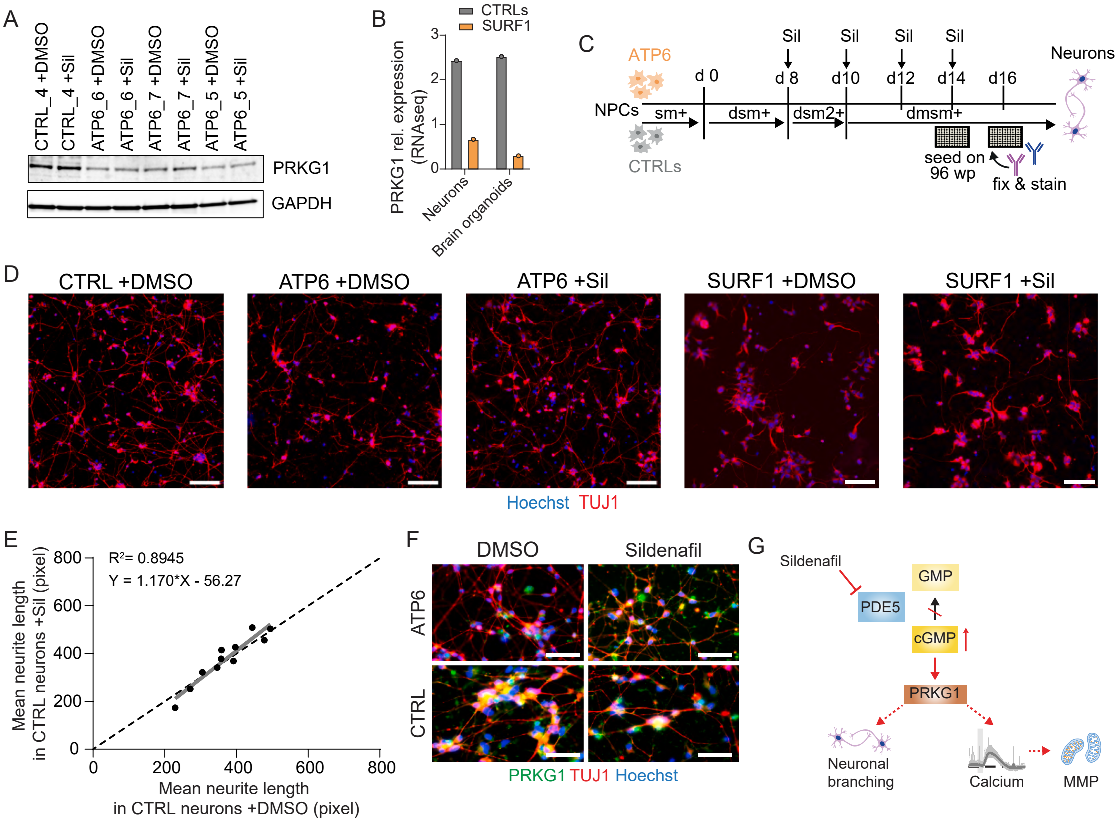

H

Name	hPSCreg name	Alternative name	Sex	Age (years)	Variant	Heteroplasmy (Fibs)	Heteroplasmy (iPSCs)	Heteroplasmy (NPCs)	Publication of iPSC line (PMID)
CTRLs									
CTRL_1	HMGUi001-A	XM001	f	47	-	-	-	-	29396371
CTRL_2	HHUUKDi009-A	TFBJ	m	0	-	-	-	-	28132834
CTRL_3	CRMi003-A	NCRM1	f	0	-	-	-	-	36459969
CTRL_4	BIHi269-B	-	f	42	m.9176T>G	55.0%	1.0%	1.6%	36669241
CTRL_5	HVRDi004-B	PGP1	m	55	-	-	-	-	36459969
CTRL_6	IUFi004-A	iPS12-10	f	30	-	-	-	-	38217996
CTRL_7	BIHi266-A	-	f	31	m.8993T>G	0.0%	0.0%	0.0%	36669241
CTRL_8	WISCi004-B	-	f	0	-	-	-	-	18029452
CTRL_9	UMGi014-C	-	m	-	-	-	-	-	33905594
ATP6									
ATP6_1	HHUi001-A	TDA2	f	47	m.9185T>C	99.0%	100.0%	100.0%	28132834
ATP6_2	HHUi002-A	TDA3	f	20	m.9185T>C	100.0%	100.0%	100.0%	28132834
ATP6_3	HHUi003-C	A4_W1	m	4	m.9185T>C	93.5%	100.0%	100.0%	36137325
ATP6_4	MDCi008-A	8993 B12	m	9	m.8993T>C	96.8%	98.2%	97.9%	35279592
ATP6_5	MDCi009-A	8993 C11	f	2	m.8993T>G	97.8%	97.4%	96.2%	35279592
ATP6_6	MDCi010-A	8993 D7	m	3	m.8993T>G	98.1%	98.1%	97.9%	35279592
ATP6_7	BIHi267-B	-	m	17	m.9176T>G	98.0%	98.0%	98.0%	36669241
SURF1					**Variant**				
SURF1_1	HMGUi001-A-64	C1_mut2	f	47	Isogenic mutation (c.769G>A)				33771987
CTRL_1	HMGUi001-A	C1	f	47	Isogenic control				33771987
NDUFS4									
NDUFS4_1	HVRDi004-B-6	E9	m	55	Isogenic mutant (c.316C>T)				36741056
NDUFS4_2	HVRDi004-B-7	F3	m	55	Isogenic mutant (c.20C>G)				36741056
CTRL_5	HVRDi004-B	PGP1	m	55	Isogenic control				36741056

Figure S10. Functional validations in human neuronal models of LS, related to Figure 4

(A) Representative immunoblot of PRKG1 (78 kDa) and GAPDH (37 kDa) in control NPCs and LS NPCs treated with 10 μM sildenafil or DMSO for 16 h (quantification in Figure 4L).

(B) *PRKG1* gene expression in *SURF1* mutant neurons and brain organoids (SURF1_1) compared with isogenic controls (CTRL_1) based on published bulk RNA-seq.[25]

(C) Schematic of the differentiation into dopaminergic-enriched neuronal cultures.

(legend continued on next page)

(D) Representative images of neurons from controls (CTRL_1), *MT-ATP6* mutants (ATP6_7), and *SURF1* mutants treated with 10 μM sildenafil or DMSO for 8 days. Scale bar: 100 μm.

(E) Linear regression of the mean neurite length (mean over median) in control neurons (CTRL_1, *n* = 4; CTRL_2, *n* = 3; CTRL_3, *n* = 1; CTRL_5, *n* = 3) treated with sildenafil for 8 days over control neurons exposed to only DMSO (gray line). Dots: individual values per experiment. Black dotted line: hypothetical linear regression with no effect (y = x).

(F) Representative immunostaining for PRKG1 and TUJ1 in control neurons (CTRL_2) and LS neurons (ATP6_4) treated for 8 days with sildenafil or DMSO. Scale bar: 50 μm.

(G) Mode of action of sildenafil. Red arrows: known actions of sildenafil. Dashed arrows: suggested actions of sildenafil in LS neural cells.

(H) Details of the human iPSC lines used in this study. For lines carrying *MT-ATP6* variants, we quantified the heteroplasmy in the parental fibroblasts (Fibs) and in the respective iPSCs and NPCs.

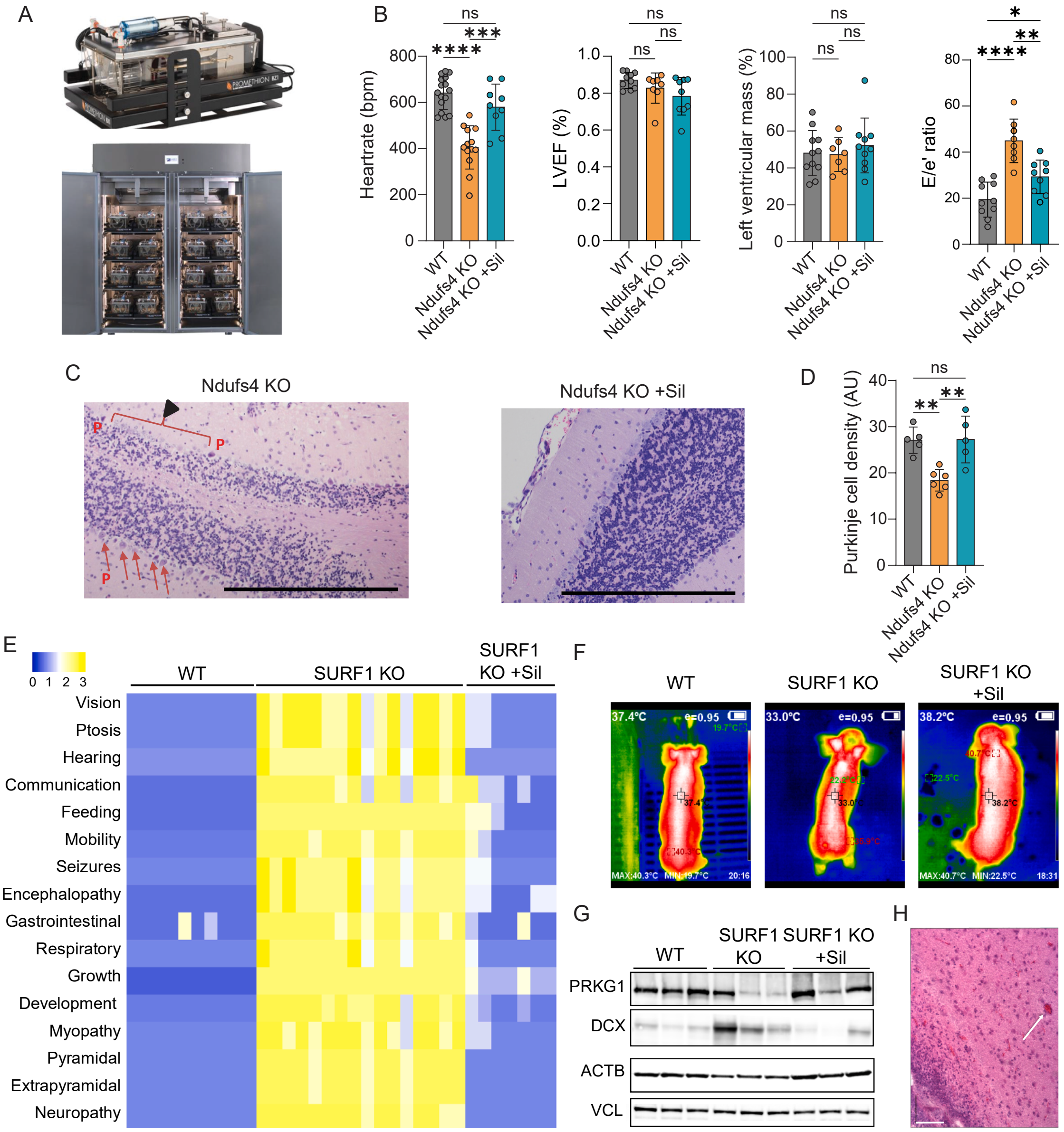

Figure S11. Sildenafil effects in LS animal models, related to Figure 5

(A) Metabolic chamber to assess metabolic fitness in *Ndufs4* KO mice.

(B) Cardiac effects of sildenafil in 42- to 45-day-old *Ndufs4* KO mice ($n = 8–10$): heart rate (bpm) and diastolic dysfunction measured by tissue Doppler imaging, left ventricular mass (%), left ventricular ejection fraction (LVEF, %), and ratio of the peak early mitral inflow velocity over the early diastolic mitral annular velocity (e′) measured by echocardiography. *$p < 0.05$, **$p < 0.01$, ***$p < 0.001$, ****$p < 0.001$; two-tailed Mann-Whitney U test.

(C and D) Representative immunohistochemistry and related quantification of Purkinje cells (P) density in 42- to 45-day-old *Ndufs4* KO mice ($n = 5–6$). Arrows: loss of Purkinje cells. **$p < 0.01$; ANOVA post hoc analysis. Scale bar: 500 μm.

(E) Clinical features of WT pigs ($n = 10$), untreated *SURF1* KO pigs ($n = 16$), and *SURF1* KO pigs treated with sildenafil ($n = 7$) based on the adaptation of the NPMDS scale.

(F) Representative thermal images of WT and *SURF1* KO pigs (quantification in Figure 5G).

(G) Representative immunoblot of PRKG1 and DCX in WT pigs (n=3), untreated *SURF1* KO pigs ($n = 3$), and *SURF1* KO pigs treated with sildenafil ($n = 3$). Vinculin (VCL) and actin beta (ACTB): loading controls (quantification in Figure 5J).

(H) Representative hematoxylin and eosin (H&E) staining of the brain of a *SURF1* KO pig receiving sildenafil 2.1 mg/kg/day who died after 4 days. White arrow: cerebral microhemorrhage. Scale bar: 100 μm.

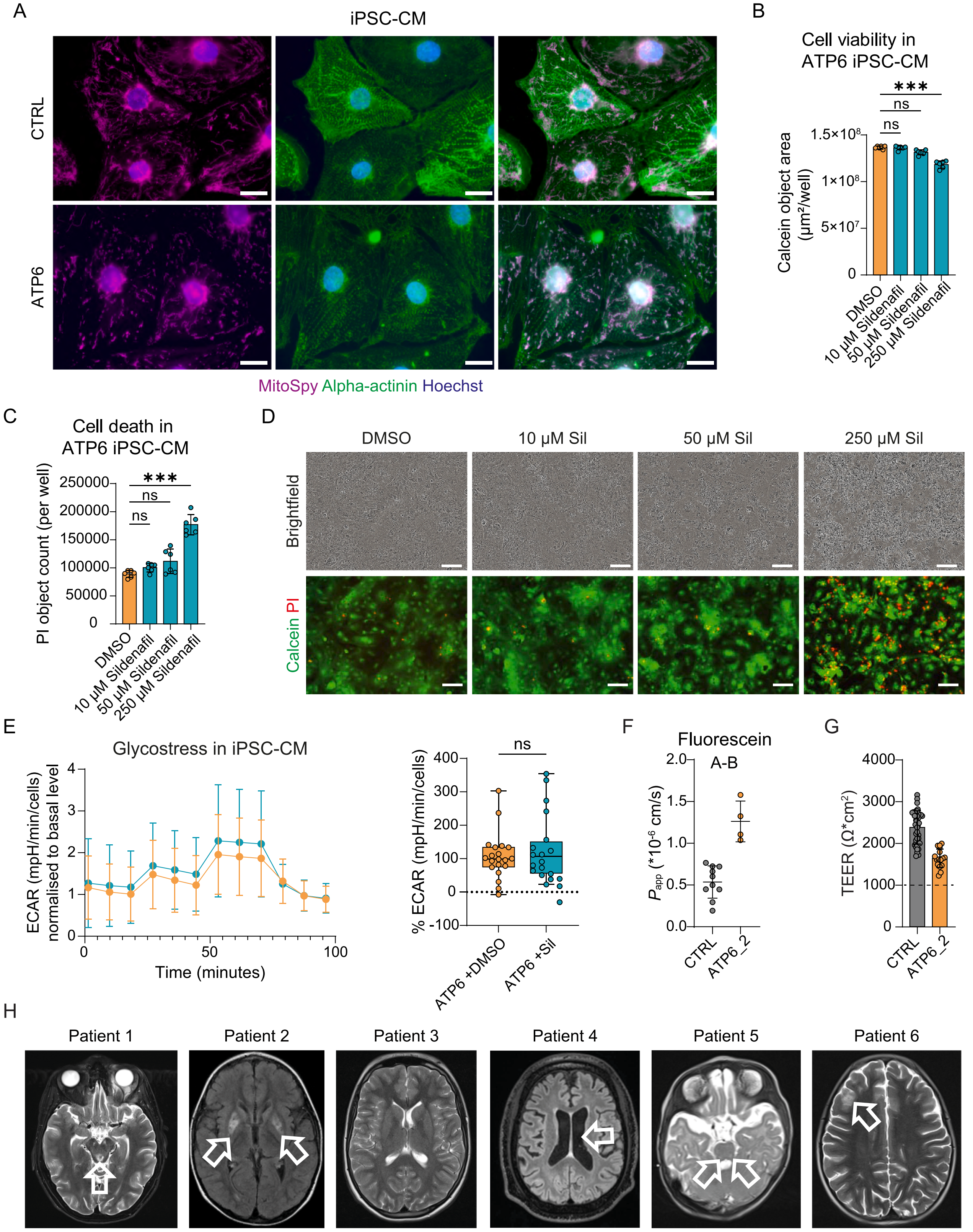

(legend on next page)

Figure S12. Sildenafil impact on iPSC-CMs, BBB, and LS patients, related to Figure 6

(A) Representative immunostaining of iPSC-derived cardiomyocytes (iPSC-CMs) from LS (ATP6_7) and control (CTRL_9). Scale bar: 100 μm.

(B and C) Quantification and representative images for live-cell count via calcein and cell death count via propidium iodide (PI) in iPSC-CM from LS (ATP6_7) treated with sildenafil for 24 h. $n = 6$ from two independent experiments, $^{***}p < 0.005$; unpaired two-tailed *t* test. Scale bar: 100 μm.

(D and E) Representative images and related quantification of seahorse-based GLY stress test in iPSC-CM from LS (ATP6_6 and ATP6_7) treated with 10 μM sildenafil for 24 h. $n = 20$ from two independent experiments; unpaired two-tailed *t* test.

(F) Apparent permeability coefficient (*p*app, 10^{-6} * cm/s) from the apical to basolateral (A-B) compartment of fluorescein in control BCECs (CTRL_8) and LS BCECs (ATP6_2), $n = 3$–5 independent experiments.

(G) Transendothelial electrical resistance (TEER) measurement in BCECs from control (CTRL_8) and LS (ATP6_2), $n = 3$–5 independent experiments.

(H) Representative cMRI taken during the diagnosis of the six LS patients who were subsequently treated with sildenafil. Arrows indicate: T_2-signal increase in the perisylvian gray matter of the brain stem in Patient 1, FLAIR signal increase in the basal ganglia in Patient 2, spontaneous resolution of T_2-signal intensities at the age of 14 years in Patient 3 (see Figure 6E for comparison), FLAIR image with generalized brain atrophy and enlargement of the intracerebral fluid spaces in Patient 4, T_2-signal increase in the *Substantia nigra* and the *Fasciculus longitudinalis* of the brain stem in Patient 5, and T_2-signal increase in the cortical gray matter in Patient 6.